ELUCIDATING THE MORPHOLOGICAL AND SYNAPTIC ORGANIZATION OF MAMMALIAN TOUCH CIRCUITS

by
Emily Kuehn

A dissertation submitted to Johns Hopkins University in conformity with the requirements for the degree of Doctor of Philosophy

Baltimore, Maryland
October, 2016

ABSTRACT

The somatosensory system is tasked with translating and processing a myriad of complex stimuli from the periphery to the central nervous system to generate our tactile experience of the world. This process begins in the periphery, where low-threshold mechanoreceptors (LTMRs), neurons that are exquisitely tuned and organized for conveying innocuous touch information, are stimulated. LTMRs subsequently project to the deep dorsal horn, a poorly characterized spinal cord region implicated in processing LTMR information. We observed a previously unappreciated organization of LTMR peripheral projections to the skin, in which the majority of LTMR peripheral projections of a single subtype are largely non-overlapping in their innervation of hair follicles. We further noted differences in these overlap patterns as a function of body region or hair follicle type. This organization is subsequently maintained and translated in LTMR central projections, with central organization influenced by the body region and orientation of their peripheral receptive fields and notable differences in organization across different LTMR subtypes. Further, we report an array of mouse genetic tools for defining neuronal components and functions of the dorsal horn LTMR-recipient zone (LTMR-RZ), a role for LTMR-RZ processing in tactile perception, and the basic logic of LTMR-RZ organization. Within the LTMR-RZ, we found an unexpectedly high degree of neuronal diversity – seven excitatory and four inhibitory subtypes of interneurons exhibiting unique morphological, physiological, and synaptic properties. Remarkably, LTMRs form synapses on between 4 and 11 LTMR-RZ interneuron subtypes while, conversely, each LTMR-RZ interneuron subtype samples inputs from at least one to three LTMR classes, as well as spinal cord interneurons and corticospinal neurons. Thus, the discrete organization of LTMR peripheral and central projections likely underlies the somatotopic nature of innocuous touch. Further, the LTMR-RZ is a sensory processing region endowed with a neuronal complexity that rivals the retina and functions to pattern the activity of ascending touch pathways that underlie tactile perception.

Thesis Advisor and Reader #1	David Ginty, Ph.D.
Committee Chair and Reader #2	Shanthini Sockanathan, Ph.D.
Committee Member	Lisa Goodrich, Ph.D.
Committee Member	Corey Harwell, Ph.D.
Committee Member	Qiufu Ma, Ph.D.

ACKNOWLEDGEMENTS

The work presented in this document was only possible with the collaboration, guidance and support from many others. Listed here are those who were directly involved in my research and time as a graduate student, although many others before inspired, educated, and empowered me to reach this achievement. To them, and those listed here, thank you.

My advisor, Dr. David Ginty, provided endless guidance, instruction, and support during my tenure as a graduate student in his lab. Moving with him and our fellow lab members to a new city and university introduced a unique set of challenges, but working with David alone made the move worth it. He brings energy, excitement, and kindness to every scientific discussion, motivating and inspiring those around him. I hope in my future professional roles I can harness the same remarkable talent.

Numerous collaborators and colleagues contributed to the research presented here. Dr. Victoria Abraira in particular served as part-mentor, mostly friend and ally in my time as a graduate student. She taught me to be passionate and rigorous in my scientific research, as well as to be bold, both in work and in life. Additional collaborators include Dr. David Hughes, who provided guidance and expertise in synapses of the spinal cord; Dr. Cherry Ho, who laid the groundwork for my analysis of LTMR peripheral organization, and a host of current and former Ginty lab members: Anda Chirila, Mark Springel, Lauren Orefice, Alexis Tolliver, Amanda Zimmerman, Justin Zhou, Chengzhuo Gao, Michael Rutlin, Connie Tsan, Karleena Bashista, and Jessica Hoynoski. Drs. Carmen Birchmeier, Susan Dymecki, Guoping Feng, Doug Forrest, Jun Chul Kim, Jeremy Nathans, and

Hongkui Zeng generously providing mouse lines used in this study. Within the HMS community, I would also like to thank Raffaele Potami (HMS Research Computing group), Adam Granger, and Mahmoud El-Rifai (HMS Neurobiology Imaging facility) for assistance in MATLAB coding as well as array tomography processing and analysis. Many thanks to my thesis committee members, Drs. Shan Sockanathan, Lisa Goodrich, Corey Harwell, Qiufu Ma, and the late Steve Hsaio, as well to Victoria Abraira, Lauren Orefice, and Jessica Barowski for feedback on this manuscript. Finally, I am grateful for the privilege to have worked with many talented undergraduate students, in particular, Katherine West and Haley Dolan, allowing me to develop as a mentor while also gaining their contributions to my own research.

In addition to research contributions, many personal thanks are owed to scientists, friends, and family alike. First, to my tireless husband, Michael Chodos, who would move to another planet with me if I asked him to (it's true - it was in our wedding vows!). Words cannot express the appreciation and love I feel for him every day. To my parents, who taught me to be patient, kind, curious, and driven, and are always excited to hear about my research and provide unconditional love and support. To my in-laws and newly extended family, thank you for embracing 'science girl' as one of your own. Katie and Krissy, my friends and former roommates, are always a source of support and encouragement and taught me to be scientifically curious, open, and generous. Jessie, lab manager and close friend, is always willing to lend an ear and continues to teach me how to be courteous and efficient in the workplace. Lauren, baymate and friend, reminds me each day how exciting it is to be a scientist and from her I have learned to appreciate the smallest of scientific victories. Amanda, with whom I had the honor of teaching a

Neuroscience tutorial for a full year, taught me to think on my feet as we together navigated the challenges of teaching. Friendships forged before leaving Hopkins still remain strong and I’m grateful to all of my friends from Baltimore who didn’t let the distance hinder our friendships. Thank you especially to Tym and Ellen for the engagements, weddings, half marathons, and endless love. Beyond the bench, Paige, Andee, Chad, and Nicole have kept me sane through Boston winters and grad school blues. Thank you, all of you, for being a part of this journey.

TABLE OF CONTENTS

LIST OF TABLES

LIST OF FIGURES

CHAPTER 1. INTRODUCTION

The world around us is rich with tactile information, and our perception of it requires an ability to detect and distinguish a variety of mechanical stimuli. As humans, we rely heavily on our sense of touch for a variety of essential tasks and behaviors, including feeding, object recognition, avoiding physical harm, mating behaviors, and child rearing. Tactile discrimination, object recognition, and sensory-motor feedback are essential for interacting with our environment, and our somatosensory system endows us with this ability. Touch encompasses a variety of modalities, including pressure, vibration, stretch, temperature, and pain. How are tactile stimuli acting upon the skin represented and processed in the CNS to yield an experience of the physical world?

1.1. The somatosensory system is a highly organized sensory system

The anatomical substrate of innocuous touch perception is rooted in the intricate innervation patterns of physiologically distinct and morphologically specialized sensory neurons termed low-threshold mechanoreceptors (LTMRs). The perception of innocuous touch begins with the activation of these LTMRs by mechanical stimuli such as vibration, skin stretch, indentation, or movement of hair follicles (Lumpkin et al., 2010). The unique morphological and anatomical arrangement of LTMR subtype endings in the skin, our largest sensory organ, underlies distinct LTMR subtype response properties and, ultimately, the perception of object size, shape, texture, vibration, rate and direction of stimulus movement, and compliance (Owens and Lumpkin, 2014; Tsunozaki et al., 2009; Zimmerman et al., 2014). In addition to these pragmatic discrimination abilities, LTMRs also confer complex social and emotional, or affective qualities of touch (Kumazawa and Perl, 1977; Olausson et al., 2002).

LTMRs are pseudo-unipolar somatosensory neurons, with cell bodies that reside in the dorsal root ganglia (DRG) and cranial sensory ganglia, with one axonal branch extending into the periphery and another branch that penetrates the spinal cord and, in some cases, the dorsal column nuclei of the brainstem. Cutaneous LTMR subtypes are classified as Aβ, Aδ, or C based on their cell body sizes, axon diameter, degree of myelination, and action potential conduction velocity (Table 1.1 and Horch et al., 1977). LTMRs are further distinguished by the cutaneous end organs with which they associate and their preferred stimuli, as well as by their rates of adaptation to constant indentation of the skin (Table 1.1 and Burgess et al., 1968). Our lab previously utilized genetic labeling of these LTMR subtypes to assess their patterns of axonal endings in mouse hairy skin and spinal cord (Bai et al., 2015; Li et al., 2011). From these studies and others, we now have a more thorough understanding of the unique innervation patterns of LTMR subtypes in hairy and glabrous skin (Li and Ginty, 2014; Luo et al., 2009; Wu et al., 2012).

Peripheral Organization

Mammalian skin can be broadly classified into two major categories: hairy and glabrous (non-hairy). Within hairy skin, hair follicles represent the major mechanosensory end organ, while glabrous skin contains four major end organs: Merkel's discs, Meissner corpuscles, Pacinian corpuscles, and Ruffini endings, with specific LTMR innervation patterns observed for each end organ (Table 1.1 and Johnson, 2001; Zimmerman et al., 2014). Studies of discriminative touch have largely focused on glabrous skin as the anatomical landmark for touch perception (Johnson et al., 1991, 2000), with hairy skin largely overlooked for its role in tactile processing. However, hairy skin plays a major role in affective touch detection, and a greater appreciation for its role in other types of tactile processing is beginning to develop (Lechner and Lewin, 2013; McGlone et al., 2014).

Most extensively studied in the rodent, murine hairy skin displays three hair follicle types: guard, awl/auchene, and zigzag, which are present at varying frequencies (1%, 23%, and 76% in trunk hairy skin, respectively) and are specifically innervated by unique combinations of LTMRs (Table 1.1 and Li et al., 2011). For example, guard hair follicles are associated with Aβ RA-LTMRs, Aβ SAI-LTMRs, and Aβ Field-LTMRs, which are differentially sensitive to hair deflection, skin indentation, and stroke, and exhibit different rates of adaptation (Abraira and Ginty, 2013; Bai et al., 2015; Burgess et al., 1968; Koltzenburg et al., 1997). Interestingly, awl/auchene and zigzag hair follicles, which account for ~99% of hair follicles of the body, are quadruply innervated by Aβ RA-LTMRs, Aβ Field-LTMRs, Aδ-LTMRs and C-LTMRs, and triply innervated by Aβ Field-LTMRs, Aδ-LTMRs and C-LTMRs, respectively (Bai et al., 2015; Li et al., 2011). In contrast to hairy skin, the light touch receptors of glabrous skin include Aβ RA1-LTMRs, Aβ RA2-LTMRs, Aβ SA1-LTMRs, and Aβ SA2-LTMRs (Johnson and Hsiao, 1992; Woo et al., 2015). Importantly, we now understand that, like glabrous skin, hairy skin can be considered a highly specialized sensory organ. Each of the three major hair follicle types of hairy skin are innervated by a unique combination of LTMRs, forming distinct mechanosensory end organs, which subsequently display reiterative patterns in the hairy skin (Li et al., 2011; Schlake and Thomas, 2007). These specific innervation patterns in the skin are the basis of the somatotopic nature of the sense of touch. The role of hairy skin in detecting and conveying tactile information is an emerging area of study where much of the underlying organization and neural substrates remain largely unknown. While it is now known what unique combinations of LTMR subtypes innervate each hair follicle type (Bai et al., 2015; Li et al., 2011), the broader organizational relationships of LTMRs in the periphery remains unexplored. In particular, what is the relationship of peripheral receptive fields for LTMRs of the same subtype and how do these relationships converge centrally? One might speculate that some LTMR subtype populations could be entirely non-overlapping, while others may require partial or complete overlap in their peripheral receptive fields for neural processes such as coincidence detection. Our goal to address these questions is timely, given the range of murine molecular genetic tools to target individual LTMR subtypes and emerging appreciation for the role hairy skin plays in tactile information processing.

Table 1.1. Comparison of low-threshold mechanoreceptor (LTMR) subtypes.[*]

LTMR subtype	Conduction velocity	Cell body size	Degree of myelination	Adaptation properties	Skin type	End organ/ ending type
C-LTMR	C (0.2-2m/s)	small	unmyelinated	intermediately adapting	Hairy	Awl/auchene & zigzag hairs Longitudinal lanceolate ending
Aδ-LTMR	Aδ (5-30m/s)	medium	lightly myelinated	intermediately adapting	Hairy	Awl/auchene & zigzag hairs Longitudinal lanceolate ending
Aβ RAI-LTMR	Aβ (26-91m/s)	large	heavily myelinated	rapidly adapting	Hairy	Guard & awl/auchene hairs Longitudinal lanceolate ending
					Glabrous	Meissner corpuscle
Aβ RAII-LTMR	Aβ (30-90m/s)	large	heavily myelinated	rapidly adapting	Glabrous	Pacinian corpuscle
Aβ SAI-LTMR	Aβ (16-96m/s)	large	heavily myelinated	slowly adapting	Hairy	Guard hairs Merkel cell (touch dome)
					Glabrous	Merkel cell
Aβ SAII-LTMR	Aβ (20-100m/s)	large	heavily myelinated	slowly adapting	Hairy	unclear
					Glabrous	Ruffini ending

[*] Adapted from Abraira and Ginty, 2013.

Central Organization and Circuitry

Within the spinal cord, LTMR central projections synapse upon second-order neurons in the dorsal horn, and in some cases, neurons in the dorsal column nuclei of the brainstem. Along the dorsal-ventral plane of the spinal cord, we refer to distinct cytoarchitectural laminae (Rexed, 1952); the laminae comprising the dorsal horn are, from most dorsal to ventral, lamina I through VI. Within this simple two-dimensional plane, previous work has shown that each LTMR class occupies distinct, although partially overlapping, laminae of the spinal cord dorsal horn (Li et al., 2011). The central endings of C, Aδ-, and Aβ-LTMRs terminate within lamina II_{iv}, laminae II_{iv}-III, and laminae II_{iv}-V, respectively (Bai et al., 2015; Li et al., 2011). Furthermore, LTMRs innervating the same small patch of hairy skin display central projections that form somatotopically-organized columns in the spinal cord dorsal horn, perpendicular to the dorsal edge of the spinal cord (Brown, 2012; Li et al., 2011). We hypothesize that these columns represent sites of integration for LTMR inputs, and thus a key locus for processing of somatosensory information in the spinal cord dorsal horn.

Unlike the skin, where tactile stimuli are presented, the spinal cord, where tactile processing begins, is not a two-dimensional structure. Therefore, the two-dimensional somatotopic organization of LTMR endings in the skin must be translated into the three-dimensional space of the spinal cord. At a basic level, somatotopy is maintained in the spinal cord along its rostrocaudal and mediolateral axes, with more caudal inputs integrated in the caudal spinal cord, and distal to proximal inputs integrated from medial to lateral regions of the dorsal horn (Brown, 2012). However, LTMR central projections exhibit different branching morphologies along the rostrocaudal axis (Abraira and Ginty, 2013). Aδ- and C-LTMR central projections travel one or two segments rostrally before arborizing within the spinal cord dorsal horn. Aβ-LTMR central projections bifurcate, sending branches in opposite directions for several segments along the rostrocaudal axis, sprouting collaterals along the way, with a subset of Aβ-LTMRs projecting to the dorsal column nuclei (DCN) in the brainstem (Bai et al., 2015; Niu et al., 2013). Further complicating this organizational issue of somatotopy in the spinal cord is the fact that Aβ-, Aδ- and C-LTMRs are present in the hairy skin at different proportions; those numbers do not allow for a simple one-to-one relationship between Aδ- and C-LTMR central projections and individual Aβ-LTMR collaterals, for example. The sense of touch is nearly useless without the ability to identify the area of the skin being stimulated. It is therefore essential that the central nervous system maintain this body map when processing and integrating tactile information.

Components of the circuitry in the dorsal horn involved with processing LTMR information include presynaptic sensory inputs, locally projecting interneurons, descending modulatory inputs, and long-range projection neurons. The majority of neurons in the dorsal horn are locally-projecting interneurons, defined as such because their axons and dendrites remain within the spinal cord (Chung et al., 1984). Populations of dorsal horn interneurons in the most superficial lamina (I and II) are important in the perception of pain, temperature, and itch, and are the most well-studied of dorsal horn interneurons (Todd, 2010). However, little is known about deep dorsal horn interneurons that integrate LTMR inputs and modulate projection neuron outputs conveying innocuous touch information to higher brain centers. There have been some attempts to distinguish spinal cord interneurons based on morphology, physiology, or expression patterns (Del

Barrio et al., 2013; Grudt and Perl, 2002; Yasaka et al., 2007), but most remain unclassified (Grudt and Perl, 2002; Maxwell et al., 2007). Considering that synaptic arrangements between LTMR subtypes and their postsynaptic targets are complex and may include synaptic contacts with axons of neighboring interneurons, elucidating which interneurons are post-synaptic targets of the various LTMR subtypes is essential for deciphering the circuitry underlying light touch. Preliminary evidence suggests that C- and Aδ-LTMRs provide inputs to a variety of specific interneuron cell types, including central and islet cells, radial and vertical cells (Grudt and Perl, 2002; Yasaka et al., 2007), and PKCγ^+ interneurons (Neumann et al., 2008). However, this is only a start into the identification of interneurons that lie post-synaptic to C- and Aδ-LTMRs; and even less is known about the candidate postsynaptic partners of Aβ-LTMRs.

Ensembles of LTMR activities emanating from the skin convey tactile information via LTMR central projections to the spinal cord and brainstem. Thus, the perception of diverse tactile stimuli requires robust and precise mechanical stimulus detection by LTMR peripheral endings in the skin and intricate processing capabilities of LTMR activity ensembles by interneurons and projection neurons in the CNS. Carefully dissecting LTMR anatomical organization as well as defining the cellular and synaptic substrates of touch information processing in the CNS will reveal how LTMR activity ensembles, internal state, and experience are integrated to generate percepts of the physical world.

1.2. An emerging view of touch information processing

The historical, canonical view of innocuous, discriminative touch information processing in the CNS has emphasized the "direct dorsal column pathway," in which Aβ-LTMR axonal branches project directly, via the dorsal column, to the brainstem dorsal column nuclei (DCN) where second order neurons project to the thalamus. Third order thalamic neurons convey touch information to the somatosensory cortex (Johnson and Hsiao, 1992; Mountcastle, 1957). In the classic "labeled line" model, LTMR subtype integration and processing begins in the somatosensory cortex, with the spinal cord, DCN and thalamus serving as relay stations. An alternate model posits an integrative somatosensory system in which touch information processing begins at the earliest stages of sensory neuron inputs to the CNS, as found in other sensory systems (Abraira and Ginty, 2013). In the visual system, for example, we now appreciate the retina as a key locus of visual information processing, with retinal ganglion cells conveying highly processed visual information from the retina to a large number of brain regions (Masland, 2001). Thus, in an analogous, emerging view of the somatosensory system, the spinal cord dorsal horn mirrors the retina by playing a key role in processing innocuous touch information delivered in the form of LMTR activity ensembles. In support of this idea, only a subset of LTMRs extend an axonal branch via the direct dorsal column pathway to the DCN while, in contrast, all LTMRs exhibit axonal branches that terminate in the dorsal horn, including regions devoid of projection neurons (Li et al., 2011). Moreover, these central LTMR terminations in the dorsal horn are organized in a highly somatotopic manner. Thus, "indirect", or post-synaptic ascending pathways, including postsynaptic dorsal column (PSDC) neurons, subsets of anterolateral tract neurons, and spinal-cervical tract neurons, are likely to convey perceptually relevant innocuous touch information from the spinal cord dorsal horn to the brain in a somatotopically organized manner. However, the neural substrates and mechanisms of LTMR ensemble integration and processing in the dorsal horn, and the functions of dorsal horn LTMR-recipient zone (LTMR-RZ) interneurons and post-synaptic ascending pathways in touch perception are poorly understood.

1.3. Defining the organizational logic of LTMRs, as well as cellular and synaptic components of the LTMR-RZ, provides fundamental insight about touch information processing

The present study considers both the complex anatomical organization of LTMRs in the periphery and spinal cord dorsal horn, as well as the cellular and synaptic organizational logic of the LTMR-RZ, with the goal of defining how these arrangements and components contribute to innocuous touch information processing and tactile perception. These issues were addressed using the mouse as a model system because of the rich array of robust murine genetic tools. Investigation of the relative overlap in peripheral receptive fields of five LTMR subtypes revealed that the majority of LTMR subtypes have largely non-overlapping peripheral receptive fields. A subset showed differences in these patterns of overlap based on the hair follicle type and/or body region being innervated. The development and use of an assay to label and visualize the axonal projections of LTMRs with adjacent or overlapping peripheral receptive fields allowed us to ascertain how somatotopic organization is maintained in the spinal cord. The organization of LTMR central projections in the spinal cord dorsal horn likely reflects the complex integration and transformation of information that must occur from their peripheral receptive fields. We observed that the organization of these central projections is influenced by the body region and orientation of their peripheral receptive fields, with notable differences in organization across different LTMR subtypes. Through an open-ended screen to identify genes that are uniquely expressed in select LTMR-RZ neuronal subtypes, and the exploitation of these genes for the generation of a large array of mouse molecular-genetic tools, we found within the LTMR-RZ seven excitatory and four inhibitory interneuron subtypes, each displaying a unique combination of morphological and physiological properties. Moreover, the generation of an excitatory synaptic atlas of the LTMR-RZ revealed that LTMR subtypes form synapses onto four to eleven LTMR-RZ interneuron subtypes and, conversely, each of the 11 LTMR-RZ interneuron subtypes receives convergent synaptic inputs from one to three LTMR subtypes, as well as other locally projecting LTMR-RZ interneurons and corticospinal projection neurons. We also found that LTMR-RZ interneurons play essential roles in texture discrimination and innocuous touch perception, and that they tune the responses of postsynaptic ascending projection pathway neurons that convey touch information from the spinal cord to the brain. From this we conclude that the mechanosensory dorsal horn is a complex and distinctly interconnected locus of LTMR and cortical input integration that orchestrates the activity of postsynaptic ascending pathways required for innocuous touch perception. The current study provides a general understanding of the anatomical basis of mechanosensory integration and processing of tactile information in the central nervous system.

CHAPTER 2. EXPERIMENTAL RESULTS

The Organizational Logic of LTMR Peripheral and Central Projections

2.1. The majority of LTMR subtypes have largely non-overlapping peripheral receptive fields

Within the periphery, LTMRs innervate cutaneous end organs in specific combinations (Table 1.1), yet little is known about how peripheral innervation patterns compare within and across populations. Understanding if LTMR peripheral terminals exhibit an overlapping or non-overlapping organization within subtype populations, for example, informs our understanding of how innocuous touch information is both detected and processed. To assess relative peripheral organization and relationships among single LTMR subtypes at the level of the population, we used a combination of LTMR-CreER mouse genetic tools (Table 2.1, Bai et al., 2015; Li et al., 2011; Luo et al., 2009; Rutlin et al., 2015) with Cre-recombinase- dependent fluorescent reporters (Table 2.2, Madisen et al., 2010). Using two reporters in the same animal (in combination with LTMR-CreER lines) permits labeling of one particular LTMR population in a stochastic fashion: some neurons are labeled with tdTomato, others with YFP, while some are labeled with both tdTomato and YFP. Treatment with optimal tamoxifen dosage achieves labeling of the majority of neurons of a particular LTMR subtype in three colors at the same relative ratios (33% red, 33% green, 33% yellow, Figure 2.1). Combining this labeling strategy with a whole-mount preparation of the skin allowed us to observe trends in LTMR innervation patterns in the periphery (Figure 2.2). In these samples, we quantified the number of neurons innervating individual hair follicles, revealing the relative amount of overlap among individual LTMRs of a single population in the periphery. From this analysis, we observed that the majority of LTMRs have largely non-overlapping peripheral receptive fields, with four of five LTMR subtypes (C-, Aδ-, Aβ SAI-, and Aβ Field-LTMRs) displaying single-neuron innervation for >70% of the hair follicles that they innervate (Figure 2.3). Interestingly, Aβ RA-LTMRs are the only subtype to display triple innervation, exhibiting the most peripheral overlap of all LTMR subtypes observed, with less than half of hair follicles showing single innervation.

Across the body, different regions are tasked with unique functions and therefore may need to engage different circuits within the nervous system. Among other properties, region-specific differences in the elasticity, barrier properties, and androgen receptor expression of the skin have been observed (Choudhry et al., 1992; Cua et al., 1990; Yosipovitch et al., 2000). Further, the three hair follicle types are present in mouse hairy skin at varying frequencies and are differentially sensitive to mechanical stimuli as a function of both anatomy and LTMR subtype-specific innervation. Thus, we speculated that different patterns of peripheral innervation by LTMR subtypes according to location or hair follicle might be expected. We assessed overlapping patterns of peripheral receptive fields according to body region (back, abdomen, and thigh hairy skin) and hair follicle type being innervated (guard hairs can be distinguished from zigzag and awl/auchene hairs by the presence of Troma1$^+$ staining to label Merkel cells). Of the five LTMR subtypes, only Aβ SAI-LTMRs show a difference in overlapping patterns according to body region, with a higher incidence of dual innervation in abdomen hairy skin (Figure 2.4). Aβ RA-LTMRs and Aβ Field-LTMRs are the only two LTMR populations in this study to innervate both guard hairs *and* awl/auchene and/or zigzag hairs, and for both of these populations, guard hairs are observed to receive a higher incidence of dual (or triple, in the case of Aβ RA-LTMRs) than other hair follicles (Figure 2.4). These observations indicate that different body regions or hair follicle types may require duplicate or even triplicate innervation from a single LTMR subtype in order to appropriately engage neural circuits and detect innocuous touch. These fundamental organizational principles of LTMRs observed in the periphery suggest that: (1) information conveyed by individual LTMR populations must largely converge in downstream circuits, as few LTMRs of the same subtype detect information from the same hair follicle(s), and (2) LTMR organization, and therefore integration or processing of tactile information, may differ according to body region and/or hair follicle types innervated. From these observations we next asked how the central projections of LTMRs maintain and organize the complex combination of tactile information detected in the periphery.

Table 2.1. Murine molecular genetic toolbox for targeting LTMR subtypes.

LTMR Subtype	Mouse Line	Reference	Tamoxifen treatment	Notes
C-LTMR	*TH*$^{2A\text{-}CreER}$	Abraira and Kuehn et al.	0.3-0.5mg at P21	
Aδ-LTMR	*TrkB*^{CreER}	Rutlin et al., 2015	2mg at P21	Labels TrkB$^+$ neurons innervating hairy skin, not glabrous skin (Meissner corpuscle).
			2mg at E12.5	Labels TrkB$^+$ neurons innervating both hairy and glabrous skin.
Aβ Field-LTMR	*TrkC*^{CreER}	Bai et al., 2015	2mg at E16.5 or P21	Label Aβ Field-LTMRs innervating both hairy and glabrous skin. Depending on age of tamoxifen treatment, Aβ SAI- or Aβ RA-LTMRs may also be labeled; distinguishable from Aβ Field-LTMR by morphology.
	Ptgfr^{CreER}	Unpublished	2mg at E16.5 or P21	
Aβ SAI-LTMR	*TrkC*^{CreER}	Bai et al., 2015	2-3mg at E12.5	Labels Aβ SAI-LTMRs innervating both hairy and glabrous skin.
Aβ RA-LTMR	*Ret*^{CreER}	Luo et al., 2009	2.5mg at E10.5-11.5	Labels Aβ RA-LTMRs innervating both hairy and glabrous skin.
	Split-Cre	Unpublished	N/A	Labels Aβ RA-LTMRs innervating hairy skin, not glabrous skin.

Table 2.2. Single- and dual-recombinase fluorescent reporter lines.

Mouse Line	Construct	Fluorescent Reporter	Reference	Notes
Ai3	Rosa26-CAG-lox-STOP-lox-YFP	Yellow Fluorescent Protein (YFP)	Madisen et al., 2010	
Ai9	Rosa26-CAG-lox-STOP-lox-tdTomato	tdTomato	Madisen et al., 2010	
Ai57	Rosa26-CAG-frt-STOP-frt-lox-STOP-lox-JAWS-GFP	Green Fluorescent Protein (GFP)	Madisen et al., 2015	
Ai65	Rosa26-CAG-frt-STOP-frt-lox-STOP-lox-tdTomato	tdTomato	Madisen et al., 2015	
Ai80	Rosa26-CAG-frt-STOP-frt-lox-STOP-lox-CatCh-eYFP	Enhanced Yellow Fluorescent Protein (eYFP)	Unpublished	low expression levels of CatCh-YFP

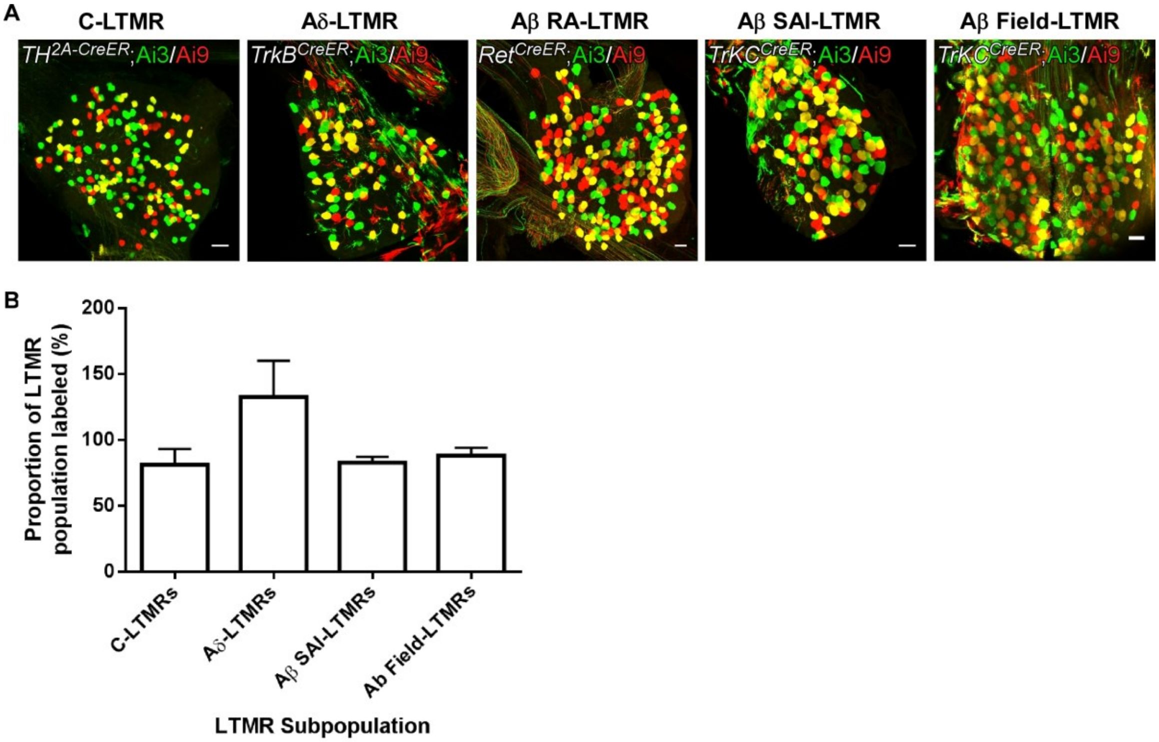

Figure 2.1. Labeling efficiency for assessing LTMR peripheral receptive field overlap.

(**A**) Representative images of whole mount immunostained DRGs labeling specific LTMR subpopulations showing approximately 33% red (Ai9), 33% green (Ai3), 33% yellow (Ai3 and Ai9) labeling. Tamoxifen treatments were as follows: C-LTMRs (0.07mg at P16 to $\mathit{TH}^{2A\text{-}CreER}$;Ai3/Ai9), Aδ-LTMRs (3mg at E12.5 to TrkB^{CreER};Ai3/Ai9), Aβ RA-LTMRs (2mg at E11.5-E12.5 to Ret^{CreER}Ai3/Ai9), Aβ SAI-LTMRs (2mg at E12.5 to TrkC^{CreER};Ai3/Ai9), and Aβ Field-LTMRs (2mg at E16.5). Scale bars = 50μm. (**B**) Quantification of efficiency of labeling for a subset of LTMR subpopulations. Labeling efficiency of C-LTMRs determined by co-immunostaining with anti-TH in the DRG: bar represents percentage of all TH$^+$ DRG neurons that are YFP$^+$ and/or tdTom$^+$. Labeling efficiency of Aδ-LTMRs determined by comparison to DRG neurons labeled by TrkB-Tau-eGFP: bar represents YFP$^+$ and/or tdTom$^+$ neurons per DRG relative to average number GFP$^+$ neurons in TrkB-Tau-eGFP (121.5 ± 8.4, n=4 animals). Labeling efficiency of Aβ SAI-LTMRs determined by co-immunostaining with anti-Troma1 in the skin: bar represents percentage of Troma1$^+$ touch domes with YFP$^+$ and/or tdTom$^+$ innervation. Labeling efficiency of Aβ Field-LTMRs determined by observing hair follicles with circumferential endings: bar represents percentage of total hair follicles (all types) with YFP$^+$ and/or tdTom$^+$ circumferential innervation. n = 3 animals for all.

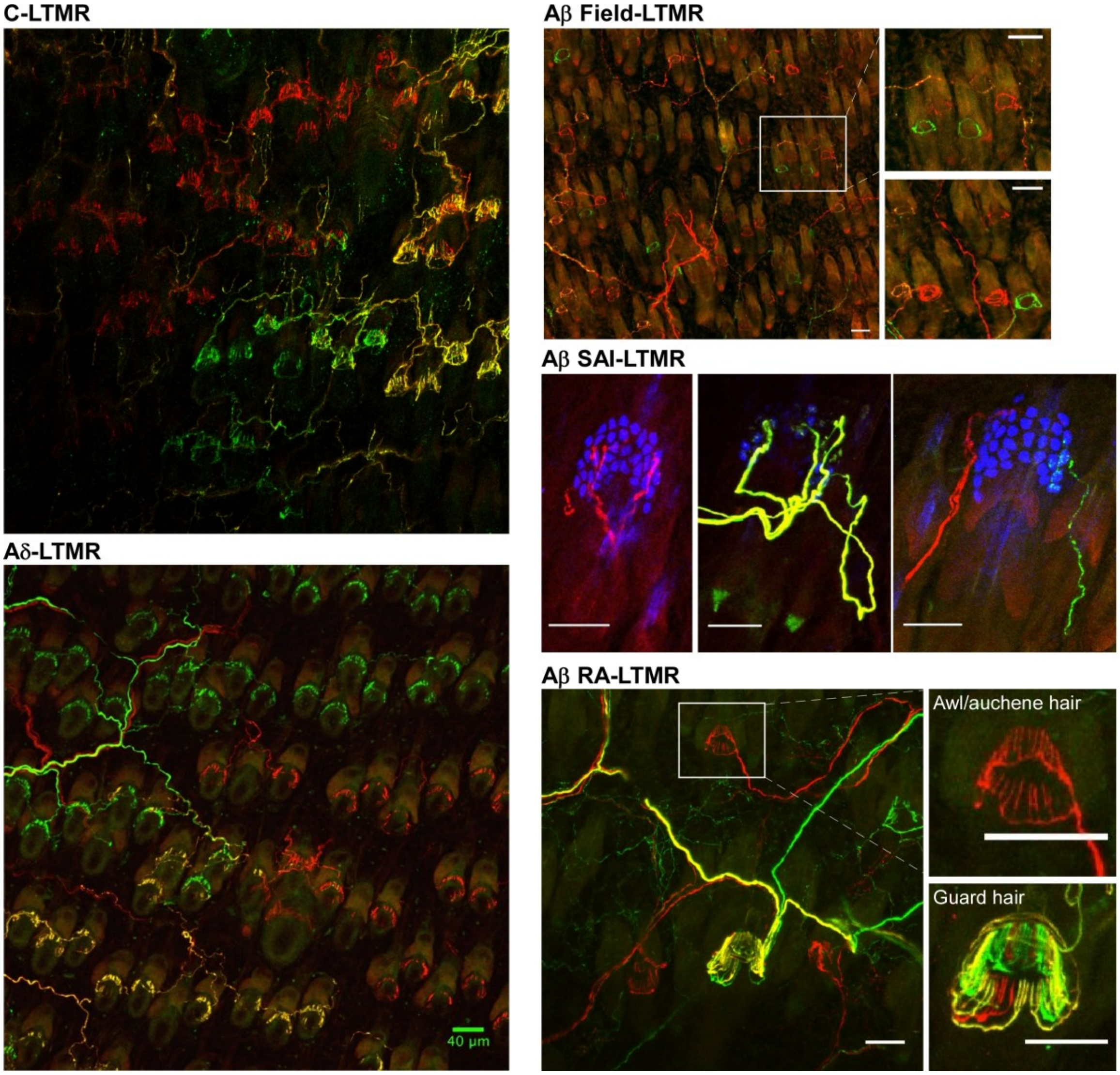

Figure 2.2. Visualizing LTMR peripheral receptive fields.
Representative images from hairy skin whole mount immunostaining (Ai3, green; Ai9, red; Troma1, blue). C-LTMRs (0.07mg at P16 to *TH*$^{2A\text{-}CreER}$;Ai3/Ai9), Aδ-LTMRs (3mg at E12.5 to *TrkB*^{CreER};Ai3/Ai9), Aβ RA-LTMRs (2mg at E11.5-E12.5 to *Ret*^{CreER}Ai3/Ai9), Aβ SAI-LTMRs (2mg at E12.5 to *TrkC*^{CreER};Ai3/Ai9), and Aβ Field-LTMRs (2mg at E16.5 to *TrkC*^{CreER};Ai3/Ai9). Scale bars = 50μm unless otherwise noted.

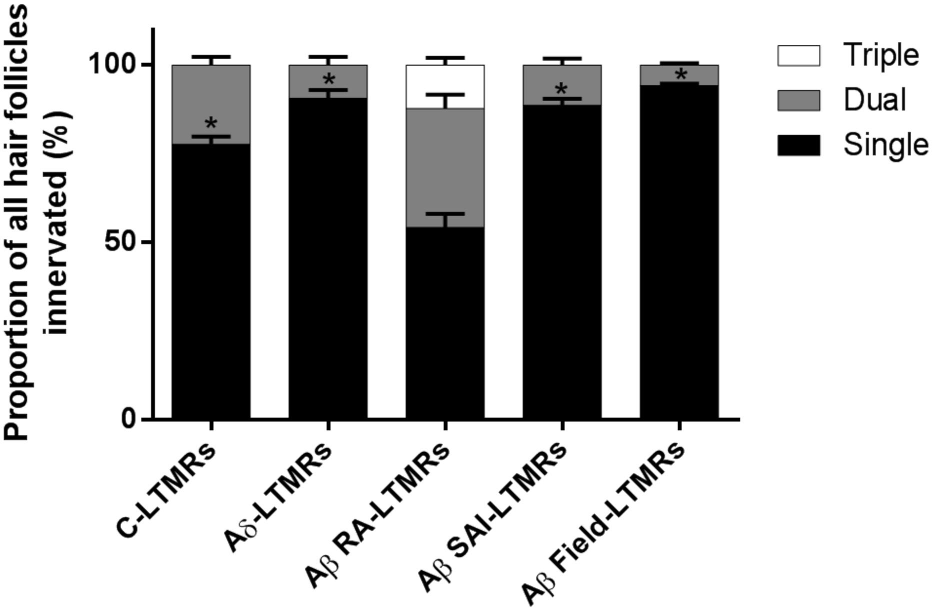

Figure 2.3. LTMR peripheral receptive fields are largely non-overlapping. Quantifications of relative peripheral overlap within LTMR subpopulations. Of total hair follicles innervated by each LTMR subtype, bars indicate the relative fraction that receive single (black), dual (grey), or triple (light grey) innervation from that subtype. C-LTMRs (0.07mg at P16 to *TH*$^{2A\text{-}CreER}$;Ai3/Ai9, n = 5 animals), Aδ-LTMRs (3mg at E12.5 to *TrkB*^{CreER};Ai3/Ai9, n = 4 animals), Aβ RA-LTMRs (2mg at E11.5-E12.5 to *Ret*^{CreER}Ai3/Ai9, n = 3 animals), Aβ SAI-LTMRs (2mg at E12.5 to *TrkC*^{CreER};Ai3/Ai9, n = 5 animals), and Aβ Field-LTMRs (2mg at E16.5 to *TrkC*^{CreER};Ai3/Ai9, n = 4 animals). To determine if LTMR populations are truly innervating the majority of hair follicles singly, a one-sample t-test was used. If proportion of innervation was above 70%, significance is indicated above the respective bar graph (*p < 0.05).

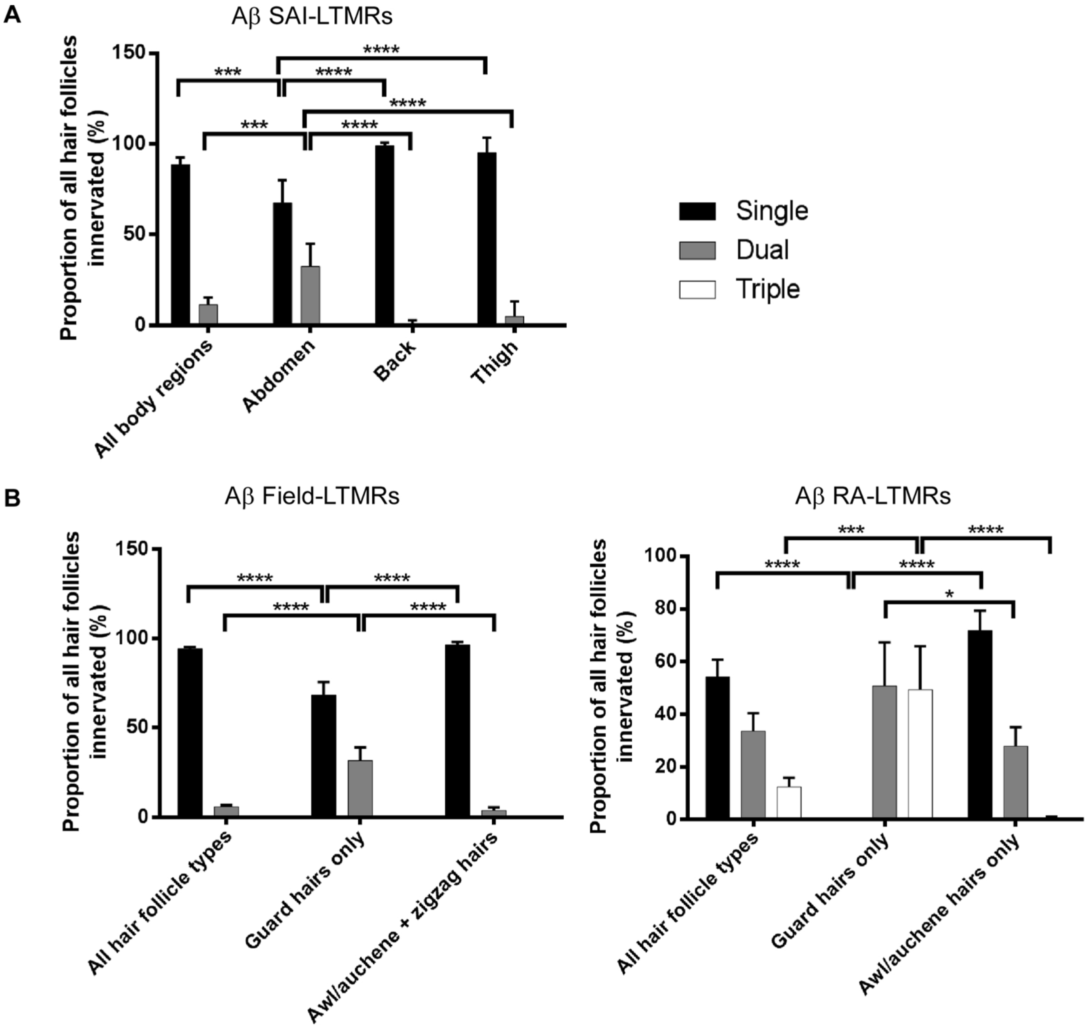

Figure 2.4. Differences in LTMR peripheral receptive field overlap according to body region or hair follicle type.

Quantifications of relative peripheral overlap within specific LTMR subpopulations according to (**A**) body region or (**B**) hair follicle type. Of total hair follicles innervated by each LTMR subtype, bars indicate the relative fraction that receive single (black), dual (grey), or triple (light grey) innervation from that subtype. Aβ SAI-LTMRs (2mg at E12.5 to $TrkC^{CreER}$;Ai3/Ai9, n = 3 animals), Aβ Field-LTMRs (2mg at E16.5 to $TrkC^{CreER}$;Ai3/Ai9, n = 3 animals), and Aβ RA-LTMRs (2mg at E11.5-E12.5 to Ret^{CreER}Ai3/Ai9, n = 3 animals). For comparisons between innervation patterns according to body region or hair follicle type, statistics are denoted above bars by brackets. For Aβ SAI-LTMRs: (Two-way ANOVA: P < 0.0001, F[6, 30] = 18.99). For Aβ Field-LTMRs: (Two-way ANOVA: P < 0.0001, F[4, 21] = 72.79). For Aβ RA-LTMRs: (Two-way ANOVA: P < 0.0001, F[4, 18] = 38.97). Post-hoc Tukey's test: *p<0.05, **p<0.01, ***p<0.0005, ****p<0.0001.

2.2. Assay development to label and visualize LTMRs in a somatotopic fashion

The organization of LTMR central projections in the spinal cord dorsal horn likely reflects the complex integration and transformation of information that must occur from their peripheral receptive fields. Previous work has demonstrated that LTMR central projections maintain somatotopic organization in the spinal cord (Brown, 2012), presumably to accurately reflect site-specific tactile stimuli in CNS processing. Somatotopy, however, is observed in both the mediolateral and rostrocaudal dimensions and LTMR central projections exhibit unique axonal morphologies (branching versus non-branching patterns, for example). Understanding the organization and relationships of LTMR central projections will inform our understanding of tactile processing and allow us to make models and predictions about this integration and circuitry. For these reasons, we sought to elucidate the organization of LTMR central projections in a somatotopically- relevant manner across multiple body regions. This goal required the development of an assay in which (1) LTMRs are sparsely and specifically labeled, (2) LTMR labeling can be targeted to a particular body region to label LTMRs with adjacent or overlapping receptive fields, and (3) both peripheral and central projections of LTMRs can be readily visualized in three-dimensions.

To define the morphological organization of individual LTMR subtype central projections and their relationship to their peripheral projections, we utilized a combination of mouse genetic tools, viral delivery of Flp recombinase to LTMR endings in the skin, and spinal cord whole-mount preparations for visualization of LTMR endings in the spinal cord dorsal horn. Our lab has developed extensive Cre and CreER tools for labeling each LTMR subtype population (Table 2.1) and for this assay, we combined these lines with dual-recombinase-dependent reporters (Table 2.2 and (Madisen et al., 2015)) and skin injections of AAV-FlpO to label specific subtypes of LTMRs innervating the same small region of hairy skin. Dual recombinase lines that were most useful to these experiments were those in which combined expression of Cre and Flp recombinases yield expression of a fluorescent marker. The use of multiple dual recombinase-dependent fluorescent reporter lines allows the opportunity to distinguish one labeled LTMR axonal projection from another, which is particularly important because of the close proximity of LTMR subtype endings, in both the skin and the spinal cord. As such, we tested three separate dual-recombinase lines from the Allen Institute: *Rosa26*$^{FSF\text{-}LSL\text{-}tdTomato}$ (Ai65), *Rosa26*$^{FSF\text{-}LSL\text{-}CatCh\text{-}eYFP}$ (Ai80), and *Rosa26*$^{FSF\text{-}LSL\text{-}JAWS\text{-}GFP}$ (Ai57) (Table 2.2, (Madisen et al., 2015), which express tdTomato, eYFP, or GFP, respectively, when both Cre and Flp recombination have occurred. We found the Ai80 line to display eYFP expression levels that were too low to be easily visualized by whole mount staining (data not shown), and thus proceeded to use the Ai65 and Ai57 dual recombinase lines for these experiments.

For targeting LTMRs that innervate the same small patch of hairy skin, we opted for Flp recombinase delivery via viral skin injections. Our lab previously demonstrated the utility of labeling a small patch of hairy skin via skin injections with CTB (Li et al., 2011); in the current study, we optimized this procedure for use with adeno-associated virus (AAV). AAV serotypes are noted to have variable tropism (Aschauer et al., 2013; Burger et al., 2004; Zincarelli et al., 2008), and while the efficiency of various AAV serotypes for gene delivery to DRG neurons had been previously reported (Mason et al., 2010; Vrontou et al., 2013), no assessment of labeling DRG neurons via non-invasive skin injections had yet been reported. Thus, we first tested a panel of AAV-Cre-GFP or AAV-GFP constructs (Table 2.3, University of Pennsylvania Vector Core, and Madisen et al., 2015) in *Rosa*$^{LSL\text{-}tdTomato}$ (Ai9), *Rosa*$^{LSL\text{-}Alkaline\ Phosphatase\ (AP)}$ (RiAP) or wildtype animals. Animals were injected at P21 with 2-6 different AAV serotypes (approximately 0.5-1µL per injection) and animals were euthanized after 3 to 6 weeks. We assessed labeling efficiency of both AAV serotype and post-injection incubation time (Figure 2.5). From this, we determined AAV1 to be the most efficient AAV serotype for labeling DRG cells via skin injection (Figure 2.5 and data not shown) and also noted that waiting five to six weeks after AAV-FlpO and tamoxifen treatment ensured robust labeling in both central and peripheral LTMR terminals (Figure 2.5). To limit expression of FlpO to neurons, and thus avoid contamination of labeling of keratinocytes and other skin cells that would prevent optimal observation of LTMR peripheral projections, we incorporated the Synapsin1 promoter into the final viral construct. The final viral construct for skin injections was AAV2/1-humanSynapsin1-FlpO (AAV1-Syn-FlpO, Table 2.3, Madisen et al., 2015). We subsequently tested and determined the optimal timing and volume of viral injections with this AAV construct for each LTMR subtype (Table 2.4). This enabled optimal labeling of specific LTMR subtypes in LTMRCreER;Ai65/Ai57 mice via AAV-Syn-FlpO injection to the skin.

The final component of assay development involved developing a method to visualize LTMR peripheral and central projections. Our lab previously developed methods for whole-mount fluorescent staining of the skin (Li et al., 2011), but had yet to attempt fluorescent whole mount staining and/or imaging of the spinal cord or brainstem. At the time of this project's conception, developing clearing techniques for large pieces of neural tissue was a major goal for the neuroscience field and there existed a variety of published clearing techniques (Zhu et al., 2013). We tested the published clearing methods known as Sca*l*e (Hama et al., 2011), ClearT and ClearT2 (Kuwajima et al., 2013), CLARITY (Chung and Deisseroth, 2013), and later, iDISCO (Renier et al., 2014), as well as modified versions of existing fluorescent staining protocols and BABB clearing already used in our lab (see Experimental Procedures). Ultimately, we found the modified fluorescent staining and BABB clearing protocol developed in-house to be the optimal method for visualizing central projections of LTMRs for a number of reasons, including minimal tissue distortion, the relatively fast time frame required by the protocol, ease of imaging, and cost of reagents. This method was further optimized by incorporating heparin into the perfusion process to minimize blood vessel autofluorescence as well as careful removal of dura and hemisection of cord and DCN to improve antibody penetration (Figure 2.6 and Experimental Procedures). Thus, we tested and optimized a combination of mouse genetic tools, viral delivery of Flp recombinase, and whole mount preparation of samples to visualize and analyze the peripheral and central projections of LTMRs in a somatotopically-relevant fashion.

Table 2.3. AAV constructs tested for labeling primary sensory neurons via skin injection.

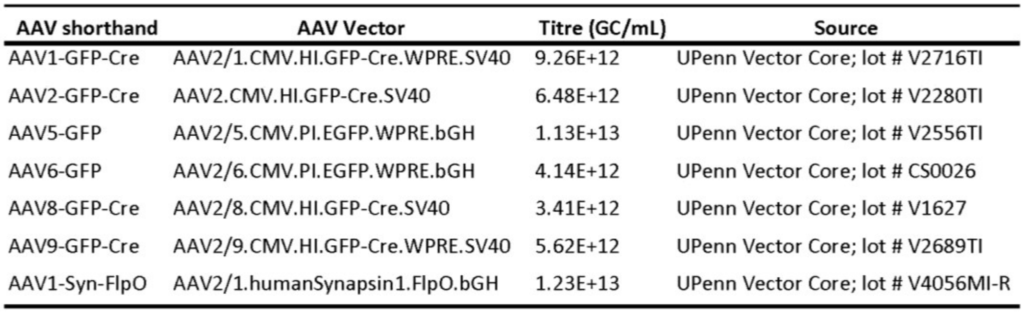

AAV shorthand	AAV Vector	Titre (GC/mL)	Source
AAV1-GFP-Cre	AAV2/1.CMV.HI.GFP-Cre.WPRE.SV40	9.26E+12	UPenn Vector Core; lot # V2716TI
AAV2-GFP-Cre	AAV2.CMV.HI.GFP-Cre.SV40	6.48E+12	UPenn Vector Core; lot # V2280TI
AAV5-GFP	AAV2/5.CMV.PI.EGFP.WPRE.bGH	1.13E+13	UPenn Vector Core; lot # V2556TI
AAV6-GFP	AAV2/6.CMV.PI.EGFP.WPRE.bGH	4.14E+12	UPenn Vector Core; lot # CS0026
AAV8-GFP-Cre	AAV2/8.CMV.HI.GFP-Cre.SV40	3.41E+12	UPenn Vector Core; lot # V1627
AAV9-GFP-Cre	AAV2/9.CMV.HI.GFP-Cre.WPRE.SV40	5.62E+12	UPenn Vector Core; lot # V2689TI
AAV1-Syn-FlpO	AAV2/1.humanSynapsin1.FlpO.bGH	1.23E+13	UPenn Vector Core; lot # V4056MI-R

Table 2.4. Optimal age and volume for injection of AAV1-Syn-FlpO to sparsely label each LTMR subtype.

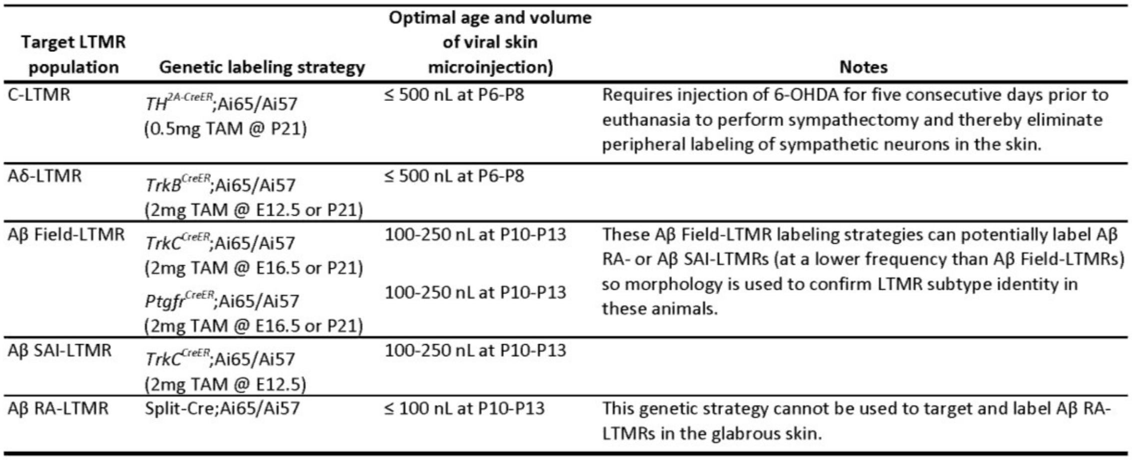

Target LTMR population	Genetic labeling strategy	Optimal age and volume of viral skin microinjection)	Notes
C-LTMR	*TH*$^{2A\text{-}CreER}$;Ai65/Ai57 (0.5mg TAM @ P21)	≤ 500 nL at P6-P8	Requires injection of 6-OHDA for five consecutive days prior to euthanasia to perform sympathectomy and thereby eliminate peripheral labeling of sympathetic neurons in the skin.
Aδ-LTMR	*TrkB*^{CreER};Ai65/Ai57 (2mg TAM @ E12.5 or P21)	≤ 500 nL at P6-P8	
Aβ Field-LTMR	*TrkC*^{CreER};Ai65/Ai57 (2mg TAM @ E16.5 or P21)	100-250 nL at P10-P13	These Aβ Field-LTMR labeling strategies can potentially label Aβ RA- or Aβ SAI-LTMRs (at a lower frequency than Aβ Field-LTMRs) so morphology is used to confirm LTMR subtype identity in these animals.
	Ptgfr^{CreER};Ai65/Ai57 (2mg TAM @ E16.5 or P21)	100-250 nL at P10-P13	
Aβ SAI-LTMR	*TrkC*^{CreER};Ai65/Ai57 (2mg TAM @ E12.5)	100-250 nL at P10-P13	
Aβ RA-LTMR	Split-Cre;Ai65/Ai57	≤ 100 nL at P10-P13	This genetic strategy cannot be used to target and label Aβ RA-LTMRs in the glabrous skin.

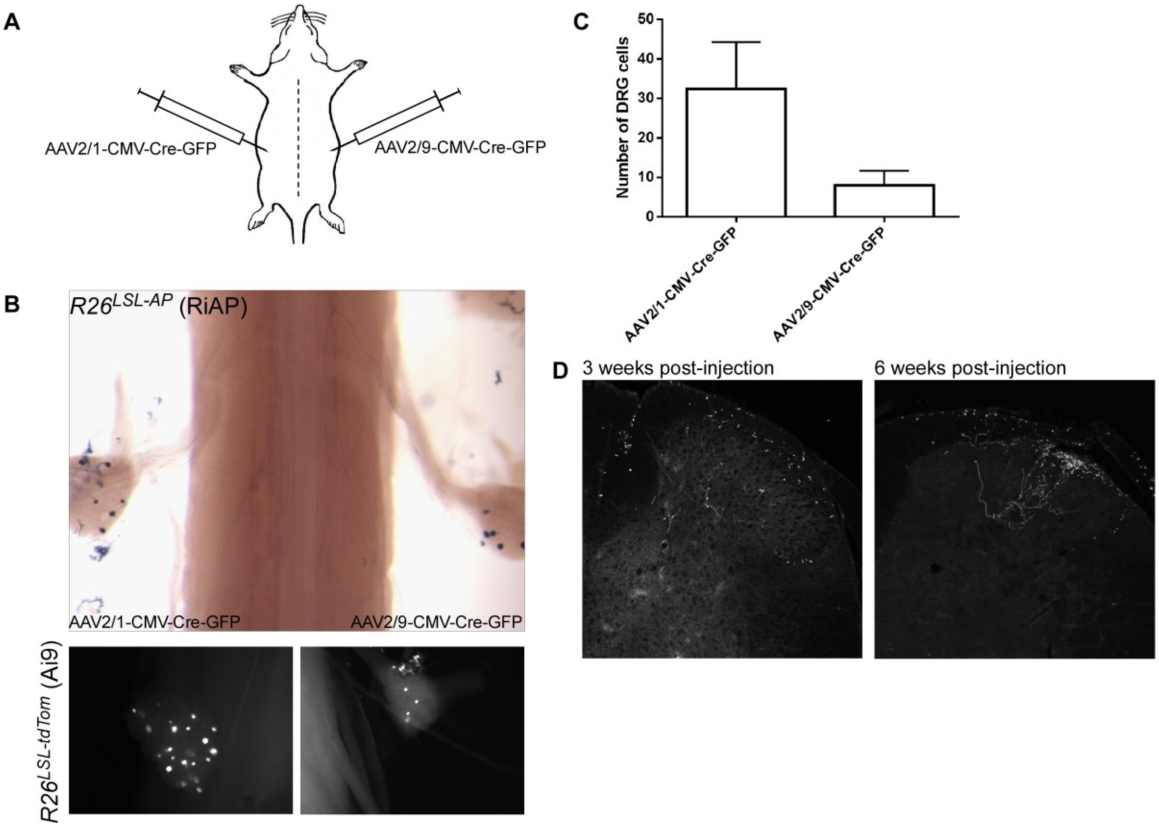

Figure 2.5. Testing AAV serotypes for LTMR labeling efficiency via skin injections. (**A**) Schematic depicting example of injection and labeling strategy for testing AAV serotypes. Within a single animal, 2-6 AAV serotypes were delivered via skin injection to the hairy skin at equal volumes. In this example, AAV1 is applied to left thoracic back hairy skin while AAV9 is applied to right thoracic back hairy skin. (**B**) Representative image of DRG showing labeling efficiency from skin injections of equal volumes of AAV1-CMV-Cre-GFP (left) or AAV9-CMV-Cre-GFP (right) in Cre-dependent alkaline phosphatase (RiAP, top) or tdTomato (Ai9, bottom) reporter animals. AAV1 consistently yielded the most robust labeling (as measured by number of DRG neurons labeled). Also note variation in soma size of labeled neurons, indicating that C- Aδ- and Aβ- subtypes can all be targeted with this viral construct. (**C**) Quantification of labeling efficiency of AAV serotypes adminstered at a volume of approximately 1µL (n=5 animals) (**D**) Representative image of transverse spinal cord dorsal horn of Cre-dependent tdTomato (Ai9) reporter mice administered equal volume injections of AAV1-CMV-Cre-GFP (0.5µL) at P21. Animals were euthanized after three (left) or six (right) weeks and tissue was processed in parallel. While an approximately equal number of DRG cells were labeled, labeling of axon terminals in the spinal cord is more robust after six weeks.

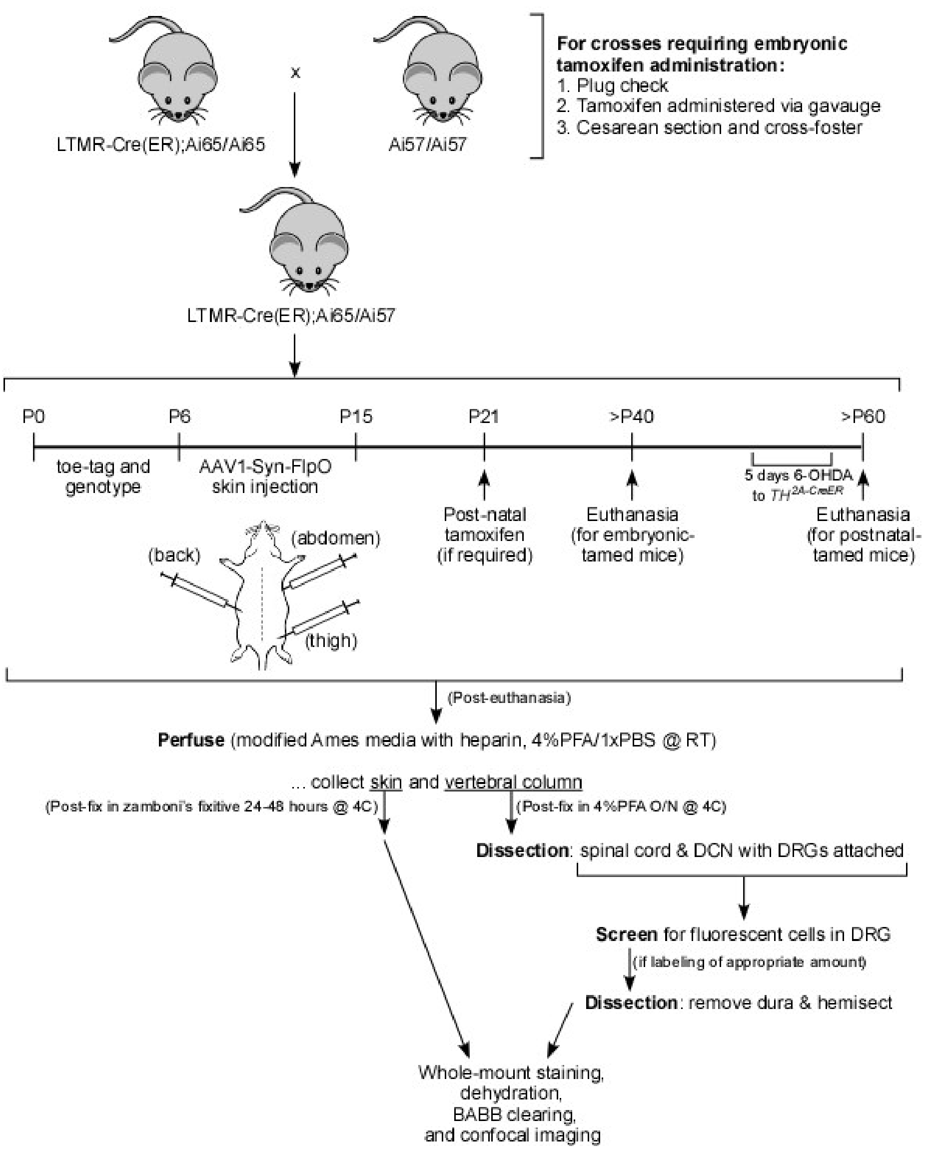

Figure 2.6. Overview of assay to label and image somatotopically organized LTMR peripheral and central projections.

2.3. Organization of LTMR central projections are influenced by body region, LTMR subtype, and orientation of peripheral receptive fields

With an assay that allowed us to label and visualize the peripheral and central projections of specific LTMR subtypes innervating the same small patch of skin (Figure 2.6), we were poised to assess how the peripheral organization of LTMRs is reflected in the central projections of these neurons. We evaluated the relative anatomical organization of LTMRs in animals expressing one or more LTMR-Cre(ER) alleles in combination with the Ai65 and Ai57 dual-recombinase reporter constructs. These samples were prepared and processed as outlined in Figure 2.6 (see Experimental Methods for more details), and from our observations we conclude four major findings.

The first fundamental observation when comparing peripheral and central projections of sparsely-labeled LTMRs is that the central projections of all LTMR subtypes exhibit profound elongation and alignment in the rostrocaudal direction and compression in the mediolateral direction (Figure 2.7). No LTMR subtypes show a bias in peripheral innervation for the rostrocaudal or mediolateral axis at the level of individual neurons, although each LTMR subtype innervates a profoundly different number of hair follicles and total area in the skin (Bai et al., 2015). For example, individual Aβ SAI-LTMRs innervate only one or two hair follicles, while an individual Aβ Field-LTMR may innervate as many as 180 hair follicles. Aβ RA-LTMRs, while innervating comparable numbers of hair follicles as C- and Aδ-LTMRs, occupy a much larger area in the skin (Bai et al., 2015). And yet all LTMR subtypes were observed to represent these peripheral innervation patterns by occupying an area in the spinal cord that, proportionally, is much larger in the rostrocaudal axis and much smaller in the mediolateral axis. While this may reflect only a bias in the anatomy (in the adult mouse, the area of the skin, when considered as a two-dimensional sheet, is approximately 1:0.75 (rostrocaudal: mediolateral), while that of the spinal cord is approximately 10:1), it still informs us that the circuits involved with processing tactile information may be oriented along the rostrocaudal axis. Indeed, we also found that many interneuron populations within the LTMR-RZ show more expansive neurites in the rostrocaudal than the mediolateral axis of the spinal cord (Figure 3.4), supporting this interpretation (Brown, 2012).

The second major observation is that there are body-region specific differences in LTMR central projection patterns. This is most aptly illustrated when comparing central projections of LTMRs that innervate thoracic back hairy skin to those that innervate cervical or thoracic abdomen hairy skin. For C-, Aδ-, Aβ-LTMRs, we observed that LTMRs innervating the back hairy skin consistently project slightly rostrally from the DRG in which their cell body lies (Figure 2.8, n=7 C-LTMRs, n=12 Aδ-LTMRs, n=4 Aβ-LTMRs), consistent with previous work (Brown, 2012). This was also observed for lumbar back and thigh hairy skin. However, those that innervate cervical or thoracic *abdomen* skin instead showed a bias to the caudal direction (Figure 2.8, n=2 C-LTMRs, n=2 Aδ-LTMRs, n=2 Aβ-LTMRs). Specifically, C- and Aδ-LTMRs project caudally from the dorsal root of entry into the spinal cord, and while Aβ-LTMRs still bifurcate and send collaterals in both directions, there are more in the caudal direction than in the rostral direction and, further, no innervation of the DCN is observed. This indicates that there are fundamental differences governing the organization of LTMR projections based on body region/location. The underlying cause of this anatomical difference could, again, reflect solely an issue of anatomy, as there is less area on which cervical and upper thoracic projections can converge. Regardless, it indicates that activation of LTMRs in this region (innervating the abdomen hairy skin) engages spinal cord circuits specifically, as the central projections of these abdomen-innervating neurons project only within the spinal cord itself.

The final two fundamental observations from this work arise from observations seeking to understand how somatotopy is maintained by LTMR central projections across 2-4 neurons with adjacent or overlapping peripheral receptive fields. First, we observed that distinct LTMR populations seem to be governed by different organizational rules when it comes to their central projections relative to peripheral organization; although both C- and Aδ-LTMRs are largely non-overlapping in the periphery (Figure 2.3), C-LTMR central projections display less overlap (~1%) in their central projections (Figure 2.9, n=2) than Aδ-LTMRs, which show a higher degree of overlap (~5-15%) in both the rostrocaudal and mediolateral axes, regardless of the overlap, or lack thereof, of the corresponding peripheral axonal endings (Figure 2.9, n=6). We further observed differences in how these LTMR subtypes translate orientation of peripheral relationships into the spinal cord. While Aδ-LTMRs maintain rostrocaudal alignment from the periphery to central projections (n=4), C-LTMRs seem to invert or neglect this organization (Figure 2.10, n=2). Finally, we observed that within a single LTMR subtype, the organization and maintenance of anatomical orientation from the periphery to the spinal cord may not follow consistent "rules" for all orientation patterns. While Aδ-LTMRs maintain rostrocaudal orientation from the periphery with direct rostrocaudal alignment of central axonal projections, those showing mediolateral alignment in the periphery show subtle mediolateral alignment centrally, but also overlap almost completely (Figure 2.10, n=3). Together, these findings that LTMR subtypes organize differently within the CNS as a function of subtype or peripheral orientation indicate that, for an individual LTMR, both the specific subtype identity as well as the relation to neighboring LTMRs of the same subtype may shape central anatomy and ultimately, perhaps, engagement and integration in neural circuits.

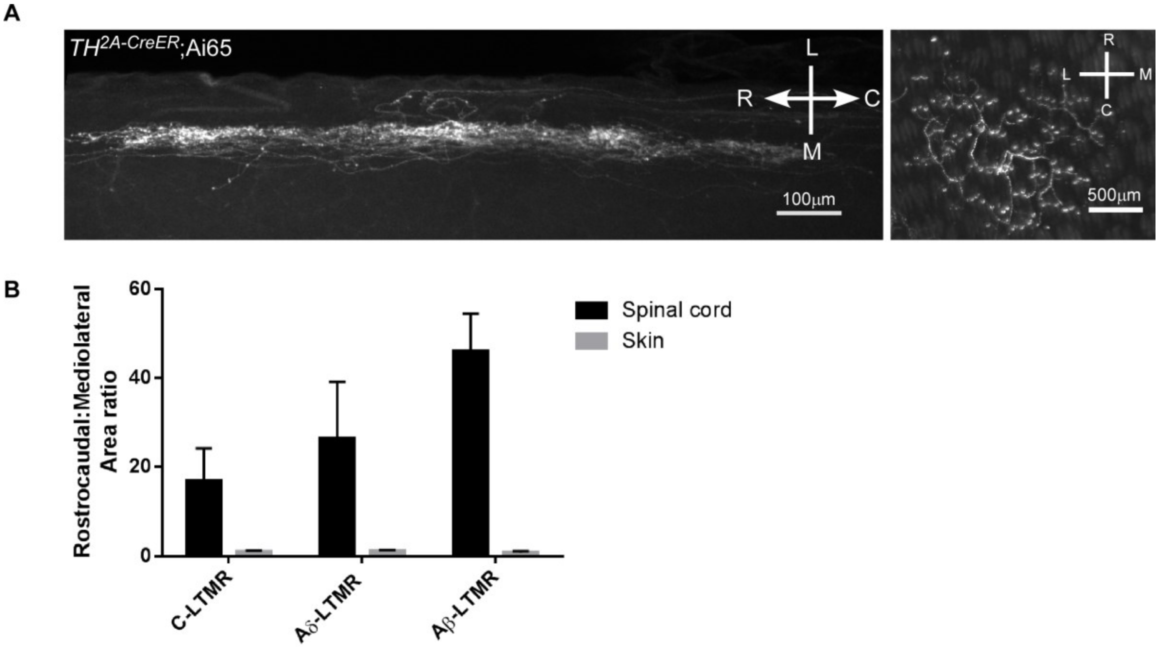

Figure 2.7. All LTMR central projections show rostrocaudal elongation and mediolateral compression as compared to their peripheral projections.
(**A**) Representative images of whole mount stain of spinal cord dorsal horn and back hairy skin. In this example, C-LTMRs are targeted using *TH*$^{2A\text{-}CreER}$;Ai65 with 500nL AAV-Syn-FlpO injection to back hairy skin at P7 and 0.5mg tamoxifen at P21. Images are compressed z-projections. Rostrocaudal and mediolateral axes are indicated. (**B**) Quantification of rostrocaudal:mediolateral ratio of area occupied by individual C-, Aδ-, and Aβ-LTMRs in spinal cord (black) versus hairy skin (grey) (n= 9, 8, and 4 for C-, Aδ-, and Aβ-LTMRs, respectively).

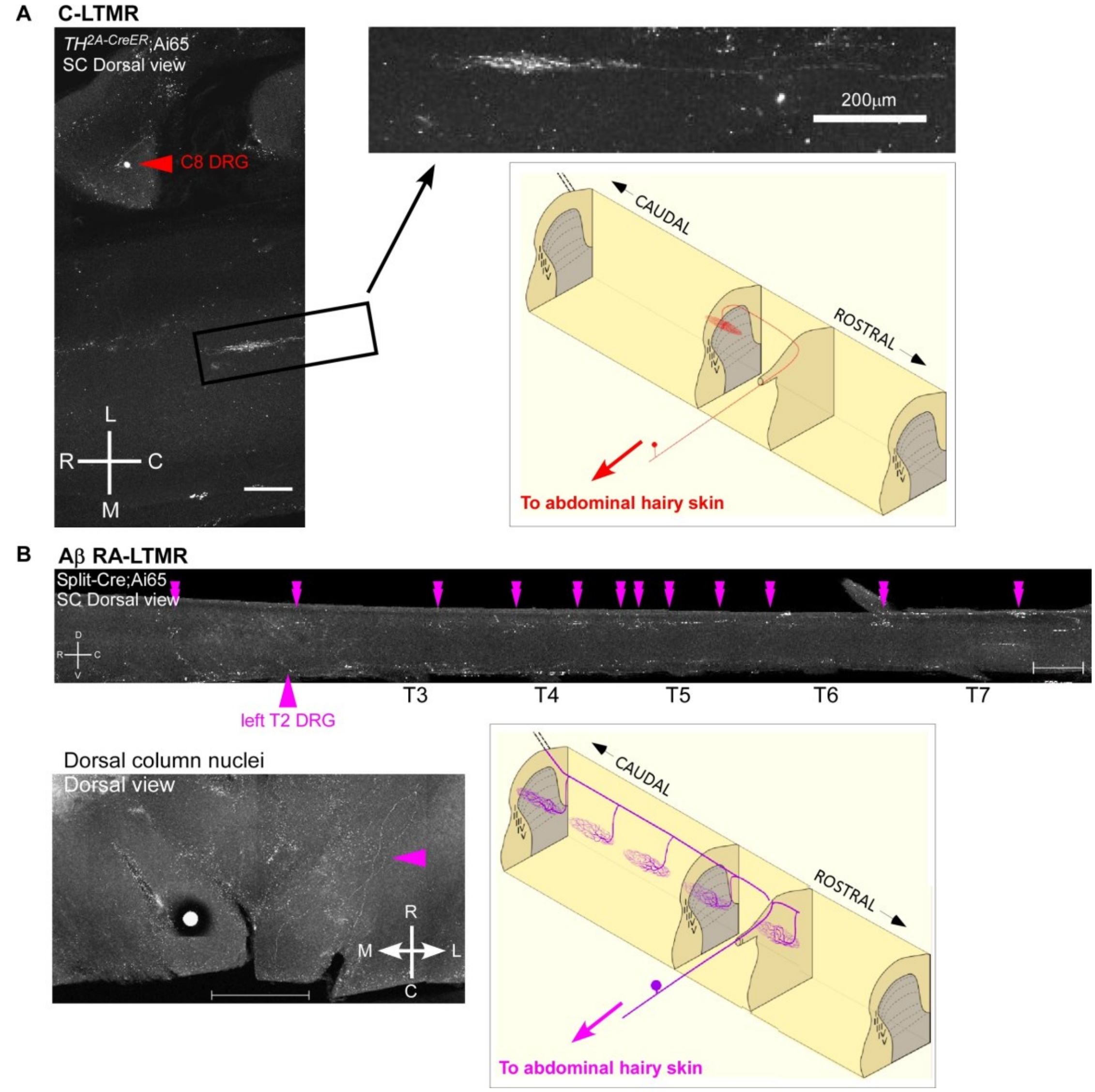

Figure 2.8. Differences in central projections as a function of body region.
(**A**) Representative images of whole mount immunostained spinal cord. In this example, C-LTMRs are targeted using $TH^{2A\text{-}CreER}$;Ai65 with 500nL AAV-Syn-FlpO injection to abdominal hairy skin at P7 and 0.5mg tamoxifen at P21. Inset shows full central projection; red arrowhead labels corresponding soma in C8 DRG. Schematic is used to depict central organization (not to scale). (**B**) Representative images of whole mount immunostained spinal cord and dorsal column nuclei. In this example, Aβ RA-LTMRs are targeted using Split-Cre;Ai65 with 200nL AAV-Syn-FlpO injection to abdominal hairy skin at P10. Schematic is used to depict central organization (not to scale). Large purple arrowhead indicates dorsal root of entry (soma in T2 DRG); double arrowheads denote collaterals in the spinal cord. Within DCN, no terminals are observed on the side ipsilateral to injection, although terminals are observed on right side (purple arrow), where back hairy skin was injected with AAV-Syn-FlpO. Images are compressed z-projections. Rostrocaudal, mediolateral, and dorsoventral axes are indicated. Scale bars = 500μm unless otherwise noted.

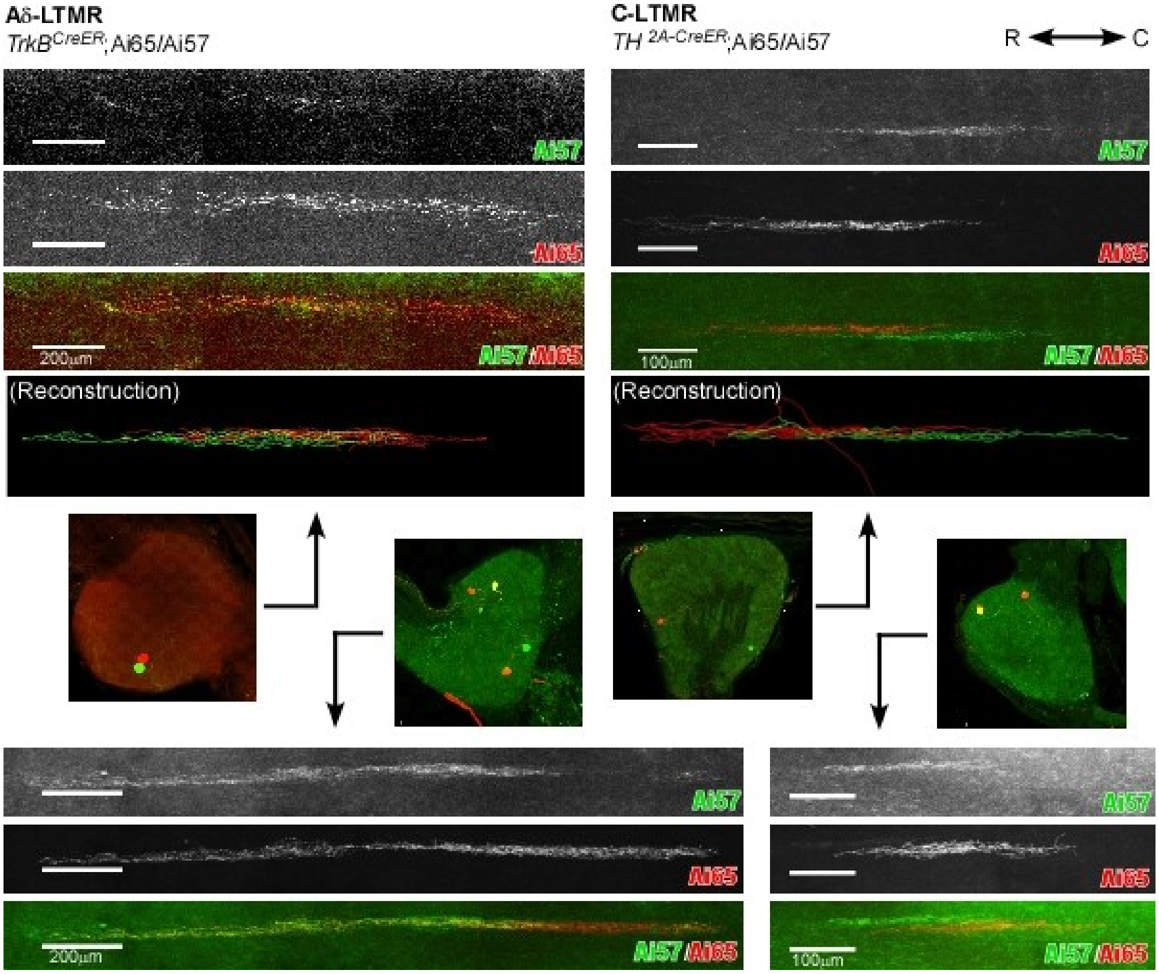

Figure 2.9. C- and Aδ-LTMR central projections show distinct patterns in central projection patterns of overlap.
Representative images of whole mount immunostained spinal cord and DRGs. In these examples, Aδ-LTMRs (left) are targeted using *TrkB*^{CreER};Ai65/Ai57 with 500nL AAV-Syn-FlpO injection to back hairy skin at P7 and 2mg tamoxifen at P21. C-LTMRs (right) are targeted using *TH*$^{2A\text{-}CreER}$;Ai65/Ai57 with 500nL AAV-Syn-FlpO injection to back hairy skin at P7 and 0.5mg tamoxifen at P21. For each sample, single channel labeling of Ai57 and Ai65 are shown in greyscale, with multichannel image below. Immunostained DRGs, showing the labeled LTMR cell bodies, correspond to central projections as indicated. For all spinal cord images, images are compressed z-stacks with rostrocaudal axis located left to right.

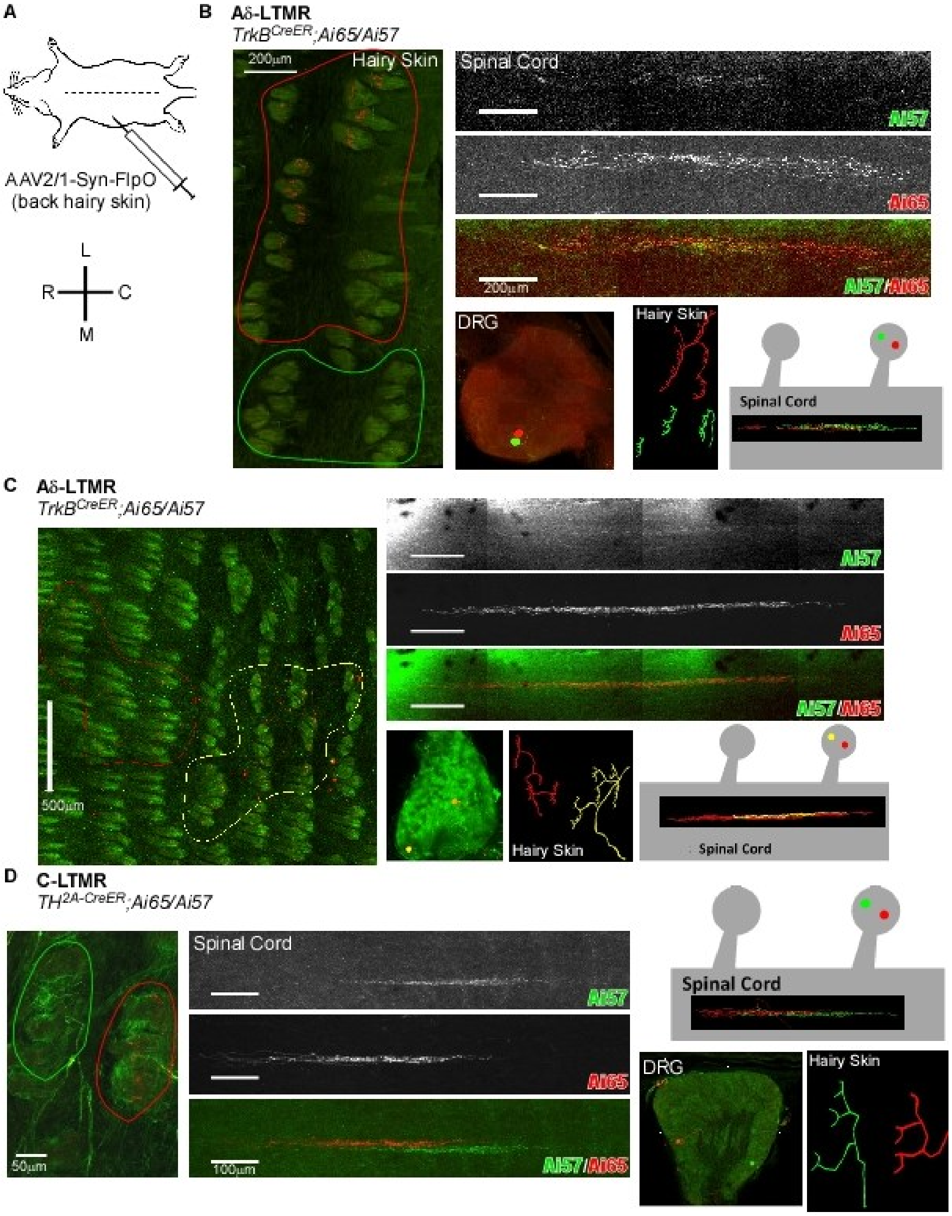

Figure 2.10. C- and Aδ-LTMR central projections maintain directionality differently according to orientation of peripheral innervation.
(**A**) Schematic showing AAV-Syn-FlpO administered via skin injection to the back hairy skin and orientation of rostrocaudal and mediolateral axes. (**B-C**) Aδ-LTMR peripheral alignment in (**B**) mediolateral or (**C**) rostrocaudal plane. Aδ-LTMRs are targeted using *TrkB*^{CreER};Ai65/Ai57 with 500nL AAV-Syn-FlpO injection to back hairy skin at P7 and 2mg tamoxifen at P21. Each panel shows endings in hairy skin (innervation region outlined), corresponding somas in the DRG, central projections, and schematic of arrangement of projections. (**D**) C-LTMRs with peripheral and central alignment. C-LTMRs (right) are targeted using *TH*$^{2A\text{-}CreER}$;Ai65/Ai57 with 500nL AAV-Syn-FlpO injection to back hairy skin at P7 and 0.5mg tamoxifen at P21.

A major function of the somatosensory system is to enable perception of the area of the skin being stimulated, and it is therefore essential that the CNS maintain a central representation of a body map when processing and integrating tactile information. Within the mouse, the somatotopic nature of touch begins with the specific and unchanging set of LTMRs innervating each hair follicle and the reiterative distribution of these hair follicles across the body. Here, we report peripheral organizational patterns within individual LTMR subtypes and how this organization is maintained and represented centrally in the spinal cord dorsal horn. The majority of LTMR subtypes have peripheral receptive fields that are largely non-overlapping with those of the same LTMR subtype, with Aβ RA-LTMRs representing an exception to this observation. A subset, Aβ RA- and Aβ Field-LTMRs, showed differences in relative levels of overlap as a function of hair follicle type, while Aβ SAI-LTMRs were the only subtype to show differences in overlap as a function of body region. All LTMR subtypes show profound rostrocaudal elongation and alignment in their central projections. For all LTMR subtypes examined (C-, Aδ- and Aβ RA-LTMRs), differences were observed in central projection patterns as a function of body region. Specifically, LTMRs innervating the abdomen hairy skin were observed to project caudally in the spinal cord, while LTMRs innervating all other regions (back, lumbar, and thigh hairy skin) were observed to project rostrally. Finally, individual LTMRs showed differences in central organization patterns relative to neighboring LTMRs as a function of both LTMR subtype and peripheral orientation patterns. Together, these findings expand the rules about anatomical organization of neurons conveying innocuous touch information to the spinal cord and reveal that the extent of somatotopic precision for some LTMRs is greater than previously appreciated. For example, C-LTMRs exhibit largely non-overlapping central projections and thus are precisely somatotopically aligned with respect to their peripheral, non-overlapping receptive fields. Further investigation of these complex somatotopic relationships, by including other LTMR subtypes in the analysis for homotypic or even heterotypic comparisons should yield even deeper understanding of the organizational logic of LTMR axonal projections.

CHAPTER 3: EXPERIMENTAL RESULTS[1]

The Cellular Architecture of the Mechanosensory Dorsal Horn

3.1. The mechanosensory dorsal horn is comprised of a large diversity of locally projecting interneurons

The spinal cord dorsal horn represents the site of convergent somatosensory inputs, locally-projecting interneurons, and descending modulatory inputs, which, in some combination, are likely conveyed to long range projection neurons residing within this region. A great deal of research has been devoted to lamina I-II, regions largely responsible for processing of pain, temperature, and itch information. However, the deeper laminae of the dorsal horn (II_{iv}-V), where LTMR central projections reside (the LTMR-recipient zone, or LTMR-RZ), remains less well understood. In particular, little is known about deep dorsal horn interneurons that integrate LTMR inputs and modulate projection neuron outputs conveying innocuous touch information to higher brain centers. Thus, we sought to define the neuronal substrates of innocuous touch information processing within this spinal cord region. Labeling of excitatory and inhibitory neuronal subtypes revealed that ~70% of neurons intrinsic to the LTMR-RZ are excitatory ($vGluT2^+$) while ~30% are inhibitory ($vGAT^+$) (Figure 3.1B). The most prominent ascending pathway emanating from the LTMR-RZ (Lamina IIiv-IV) is the post-synaptic dorsal column (PSDC) pathway (Giesler et al., 1984; de Pommery et al., 1984; Rustioni and Kaufman, 1977). We visualized PSDC neurons by retrograde labeling from the dorsal columns and found them to be located at the lamina III/IV boundary of the LTMR-

---

[1] The work presented in this section is included in a manuscript currently under review at *Cell* (Abraira and Kuehn *et al.*). In this body of work, on which EDK is a co-first author, Drs. Victoria Abraira and Anda Chirila performed the majority of the morphological and physiological characterization.

RZ (Figure 3.1A). Retrograde labeling of PSDCs and other known supraspinal projecting neurons originating in the LTMR-RZ, anterolateral tract neurons (ALT), revealed that these two projection neuron populations represent fewer than 2% of neurons in this region (Figure 3.1B, Seungwon Choi and DDG, unpublished observations for ALT neurons), and thus the vast majority of neurons in the LTMR-RZ project locally, most likely within the spinal cord itself.

We next determined the extent of LTMR-RZ interneuron subtype diversity by assessing their morphological and physiological properties as well as their synaptic organization, which are largely unexplored. Morphological diversity of LTMR-RZ interneurons was addressed using an unbiased genetic labeling approach (see Experimental Procedures) to sparsely label, reconstruct, and morphometrically analyze 305 individual neurons in this region. This analysis revealed a broad range of morphological complexity in the LTMR-RZ (6 examples are shown in Figure 3.1C), with a correlation that suggests an increase in cell body size as a function of distance below, or ventral to the IB4 layer (Figure 3.1D). Moreover, neurons exhibiting a range of spine densities and branching patterns are spread evenly throughout the LTMR-RZ, as revealed by spine measurements and Sholl analysis, respectively, indicating an intermingling within the LTMR-RZ of excitatory and inhibitory neurons with varied morphologies (Figure 3.1E-F). In complementary experiments, the extent of physiological diversity of LTMR-RZ neurons was assessed using whole-cell patch clamp recordings of randomly chosen neurons (n=52) within the LTMR-RZ of juvenile mice. Current injections into randomly chosen neurons revealed neuronal types exhibiting diverse firing patterns, including single spiking, initial bursting, phasic, delayed, gap, regular spiking, and tonic firing patterns (Figure 3.2), many of which have been previously observed in the more superficial pain-processing region of the substantia gelatinosa in mouse and the deep dorsal horn of rat (Grudt and Perl, 2002; Hochman et al., 1997; King et al., 1988; Lopez-Garcia and King, 1994; Prescott and De Koninck, 2002; Punnakkal et al., 2014; Thomson et al., 1989; Yasaka et al., 2010). Taken together, the LTMR-RZ is a complex spinal cord region comprised of neurons exhibiting a wide range of morphological and physiological properties.

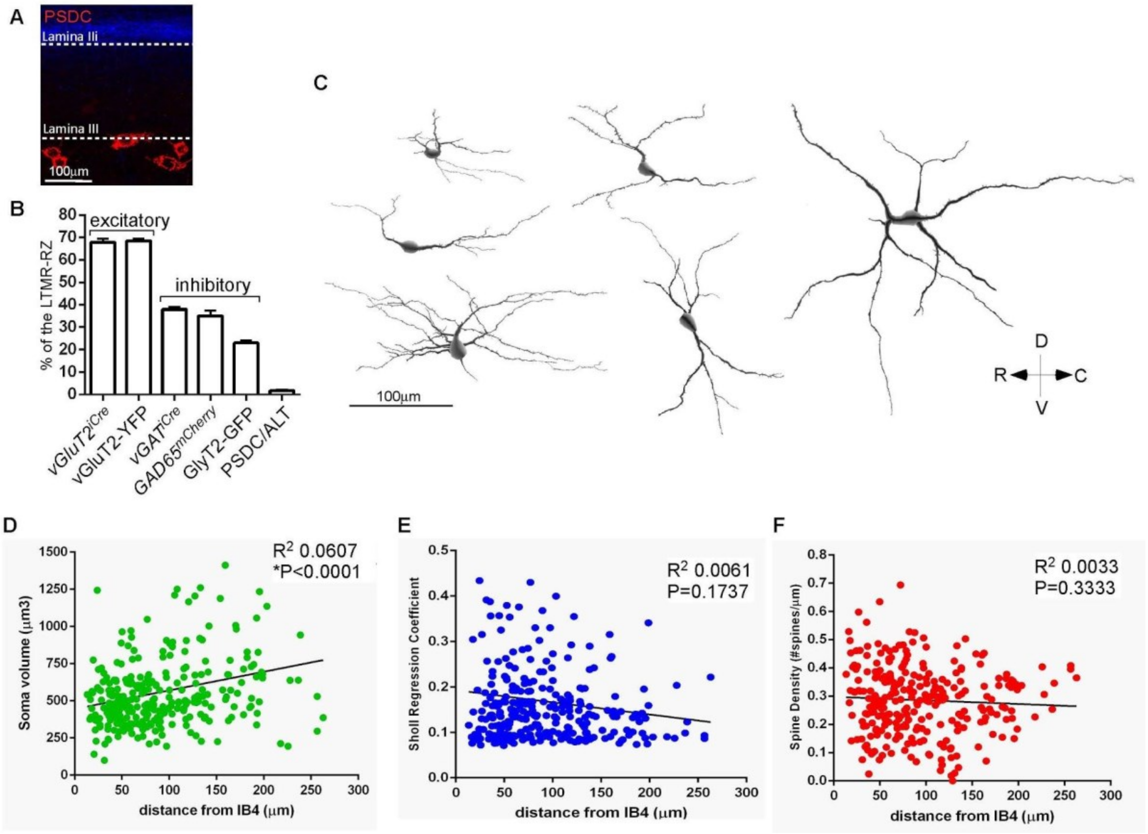

Figure 3.1. The mechanosensory dorsal horn is comprised of a large number of morphologically diverse locally projecting interneurons.
(**A**) Sagittal section of adult mouse spinal cord with CTB555 labeled post-synaptic dorsal column neurons (PSDCs, red). IB4 binding in blue. (**B**) Quantification of the percentage of LTMR-RZ neurons that are excitatory, inhibitory, or projections neurons. Excitatory neurons are labeled with *vGluT2*$^{ires\text{-}Cre}$*;R26*$^{LSL\text{-}YFP}$(Ai3) or *vGluT2*^{YFP}. Inhibitory neurons are labeled with *vGAT*$^{ires\text{-}Cre}$*;*Ai3, *GAD65*^{mCherry}, and GlyT2-GFP. PSDC and ALT neurons are labeled retrogradely from the dorsal columns and lateral parabrachial nucleus with CTB555, respectively. Quantification depicted as percentage of total NeuN$^+$ neurons within the LTMR-RZ. (**C**) Sample Neurolucida reconstructions of LTMR-RZ interneurons labeled randomly with *R26*^{CreER}*;*Ai3 and 100μg of tamoxifen at E13.5. (**D**) Plot of soma volume as a function of distance from IB4 (Lamina IIiv/III boundary). (**E**) Plot of Sholl Regression Coefficient (k) as a function of distance from IB4. Sholl Regression Coefficient (k) is a Sholl-based measure that describes the change in dendrite density as a function of distance from the cell body. A low k value is often associated with a high neurite complexity. These results show that both simple and complex neurite morphologies can be found throughout the LTMR-RZ. (**F**) Plot of spine density as a function of distance from IB4. Spine density measurements can be an indicator of excitatory and inhibitory subtypes. With inhibitory neurons often having very low spine density counts. These results suggest that both excitatory and inhibitory interneurons can be found throughout the LTMR-RZ.

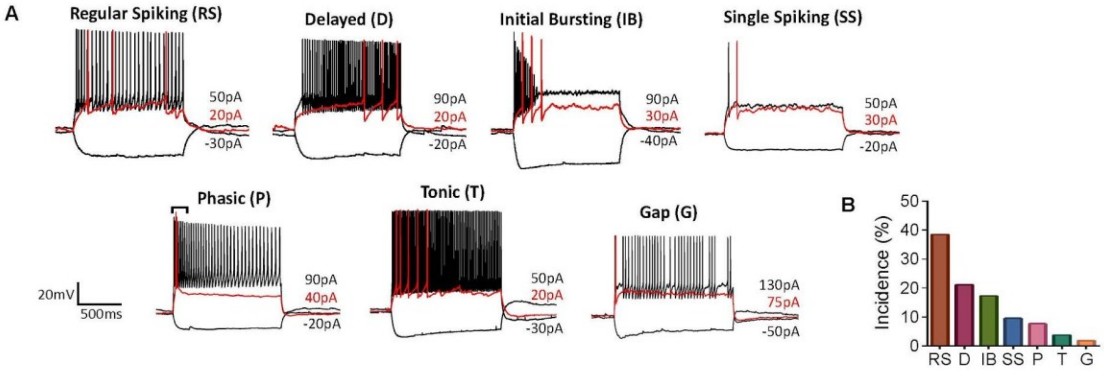

Figure 3.2. Neurons of the LTMR-RZ exhibit a diversity of firing patterns. (**A**) Sample action potential discharge patterns of randomly recorded LTMR-RZ interneurons during somatic injection of hyperpolarizing and depolarizing currents steps of increasing magnitude (black traces, rheobase trace in red, current step magnitude noted in pA). Bracket over phasic trace denotes the burst of APs at rheobase distinctive of this particular discharge pattern. (n=52). (**B**) Quantification of the percent incidence of the seven LTMR-RZ interneuron firing properties depicted in (H). RS= Regular Spiking, D= Delayed, IB= Initial Bursting, P= Phasic, T= Tonic, SS= single spiking, G= Gap.

3.2 A dorsal horn molecular-genetic toolbox for excitatory and inhibitory interneuron subtypes of the LTMR-RZ

We next sought to establish mouse molecular-genetic tools useful for defining the properties, organization and function of the morphologically and physiologically diverse interneuron populations within the LTMR-RZ. We conducted *in silico* screens of publicly available atlases that report spinal cord gene expression patterns: Gene Expression Nervous System Atlas (GENSAT, http://www.gensat.org/index.html) and Allen Brain Atlas (ABA, http://mousespinal.brain-map.org). We searched for genes that exhibited both sparse and dense patterns of expression within the adult mouse LTMR-RZ, but not the intermediate or ventral spinal cord, and that spanned cervical, thoracic and lumbar regions of the spinal cord. The entirety of the GENSAT and ABA spinal cord gene expression patterns were screened to identify 31 genes meeting our criteria. For these 31 genes, a series of immunohistochemistry and *in situ* hybridization validation experiments was performed (data not shown), and this culminated in the characterization and/or production of 10 fluorescent reporter BAC transgenic or knock-in mouse lines that label morphologically homogeneous subsets of LTMR-RZ interneurons (Figure 3.3A and 3.4). Each of these lines labels 13% or less of all LTMR-RZ neurons (Figure 3.3A). The LTMR-RZ mouse lines include GENSAT BAC-GFP transgenic lines for genes that encode the cell adhesion molecules Cadherin-3 (Cdh3) and Cerebellin-2 (Cbln2), the neuropeptide cholecystokinin (CCK), Serotonin Receptor 6 (5HTr6), Insulin-like Growth Factor Binding Protein 5 (Igfbp5), Kv Channel Interacting protein-2 (Kcnip2), and Neurogenic Differentiation Factor-4 (NeuroD4). Non-GENSAT BAC lines that emerged from this screen include a PV-TdTomato BAC transgenic line (Kaiser et al., 2016).

Finally, we generated or obtained $PKC\gamma^{mGFP}$ and $Ror\beta^{GFP}$ knockin lines, respectively, which label the PKCγ^{+} and Rorβ^{+} interneuron populations (Table 3.1 and (Liu et al., 2013).

The extent to which the 10 genetically labeled interneuron lines represent unique subsets of excitatory or inhibitory neurons within the LTMR-RZ was next determined. For this, each fluorescent reporter line (Figure 3.3A) was crossed with mice in which excitatory and inhibitory interneurons were labeled using either $vGluT2^{iresCre}$ or $vGAT^{iresCre}$ and a Cre-dependent fluorescent reporter. This analysis revealed that six of the 10 fluorescent reporter lines (Cbln2, CCK, 5HTr6, Igfbp5, NeuroD4, and PKCɣ) predominantly label excitatory neurons, while three lines (Cdh3, Rorβ, and Kcnip2) label inhibitory interneurons (Figure 3.3B). Approximately 70% of PV^{+} interneurons in laminae I-III of the rat spinal cord dorsal horn have been shown to contain GABA and glycine (Antal et al., 1991; Laing et al., 1994); (Hughes et al., 2012), and despite there being more PV^{+} cells in lamina III in the mouse, our findings mirror this pattern. Therefore, the PV^{+} neuronal population was subdivided into PVe and PVi subtypes, thus yielding a total of 10 genes that label 11 neuronal subtypes. Anatomical distribution analysis of these 11 labeled subtypes showed that each is broadly distributed throughout the LTMR-RZ, with a subset being more prominently localized to particular lamina (Figure 3.5).

We next sought to increase the versatility of the LTMR-RZ interneuron genetic toolbox by generating or acquiring Cre, CreER or FlpO recombinase tools for the majority of the 10 genes that label LTMR-RZ neuronal subsets. We generated Cdh3-CreER, 5HTr6-CreER, and Kcnip2-CreER BAC transgenic lines as well as $PKC\gamma^{CreER}$ and $Ror\beta^{CreER}$

knock-in mouse lines and acquired the previously reported CCK^{CreER} and PV^{FlpO} knock-in mouse lines (Figure 3.6A and Table 3.2, (Taniguchi et al., 2011). These recombinase mouse lines enabled interneuron subtype interrogation by crossing them with Cre-dependent GFP and tdTomato reporters to visualize neuronal morphology, synaptophysin-tdTomato and synaptophysin-GFP reporters to visualize synaptic boutons, and various silencing or ChR2 mouse lines to assess function and connectivity (Madisen et al., 2012, 2015). The recombinase lines also enabled an assessment of the extent of overlap between the 11 LTMR-RZ interneuron populations. Thus, using combinations of the fluorescent reporter lines, CreER and FlpO lines, and antibodies for immunohistochemistry, these genetic tools were found to represent largely non-overlapping populations within the excitatory and inhibitory cohorts, with some notable but minor exceptions (Figure 3.6B). Taking into consideration the percent coverage of each fluorescent reporter line, as well as the excitatory/inhibitory matrix analysis, the overlap measurements revealed that the fluorescent reporter lines together account for between 71% and 82% coverage of all LTMR-RZ neurons (Figure 3.6B).

Table 3.1. Fluorescent reporter mouse lines for studying the interneuron diversity of the LTMR-RZ.

Mouse line	MGI gene name	BAC Address	Exon KI	Genotyping primers:	Additional information
Cbln2-GFP	**Cbln2**	RP23-168P8-GFP	x	5'CATTTGGAAGGGACTGGAGA3' 5'AAGTCGTGCTGCTTCATGTG3'	GENSAT Founder #: IF387
Cdh3-GFP	**Cdh3**	RP23-199J15-GFP	x	5'TTCCATCGAAGCCAGAGACT3' 5'GAACTTCAGGGTCAGCTTGC3'	GENSAT Founder #: BK102
CCK-GFP	**Cck**	RP23-234I17-GFP	x	5'CAGGAAAGCAAGAGGAAACG3' 5'GAACTTCAGGGTCAGCTTGC3'	GENSAT Founder #: BJ203
5HTr6-GFP	**Htr6**	RP23-65B16-GFP	x	5'GGTGGCTCTATTCCATTCCA3' 5'TAGCGGCTGAAGCACTGCA3'	GENSAT Founder #: FV41
Igfbp5-GFP	**Igfbp5**	RP24-159O10 -GFP	x	5'GAGTGGGGTTGCGTTTTAGA3' 5'GAACTTCAGGGTCAGCTTGC3'	GENSAT Founder #: JE168
Kcnip2-GFP	**Kcnip2**	RP23-146N4-GFP	x	5'CGCTCTCACTTGCTGCCCAA3' 5'GGTCGGGGTAGCGGCTGAA3'	GENSAT Founder #: KN211
NeuroD4-GFP	**Neurod4**	RP23-55O18-GFP	x	5'GCTTGGGATCATAGGCATGT3' 5'GTTCACCTTGATGCCGTTCT 3'	GENSAT Founder #: EU70
PKCγ^{GFP}	**Prkcg**	x	ATG-myrGFP	5'GTGTTGCTTTCTGCCGTGT3' 5'AGGTTGGCTGCTTGAAGAAA3' 5'CCGTCGTCCTTGAAGAAGAT3'	See Experimental Procedures
PV-tdTom	**Pvalb**	RP24-306A6-tdTom	x	5'ACTGCAGCGCTGGTCATATGAGC3' 5'ACTCTTTGATGACCTCCTCG3'	Kaiser et al., 2016
Rorβ^{GFP}	**Rorb**	x	ATG-GFP	5'ACATCATGCGAGGTAAGCGAGC3' 5'GACAACCACTACCTGAGCAC3' 5'TTCAGCGTCCTGCCAAAATC3'	Liu et al., 2013

Table 3.2. Recombinase reporter mouse lines for studying the interneuron diversity of the LTMR-RZ.

					Validation of Recombinase lines:		
Mouse line	**BAC Address**	**Exon KI**	**Genotyping primers:**	**Tamoxifen**	**Method:**	**Results:**	**Additional information**
Cdh3-CreER	RP23-267K22-CreERT2	x	5'TTCCATCGAAGCCAGAGACT3' 5'TAAGCAATCCCCAGAAATGC3'	P21-23 (2mg/day)	overlap with BAC-GFP	99.6 ± 0.4% overlap (n=2)	Founder # NIDA158
CCK^{CreER}	x	ATG-CreERT2	5'GACTTCTGTGTGCGGGACTT3' 5'GAGCGGACACCCTTACCTTT3' 5'ATGCAGGCAAATTTTGGTGT3'	P21-23 (2mg/day)	homozygosity test with antibody	no antibody binding in KO	JAX#012710
5HTr6-CreER	RP23-65B16-CreERT2	x	5'GGTGGCTCTATTCCATTCCA3' 5'TAAGCAATCCCCAGAAATGC3'	P21-23 (2mg/day)	overlap with BAC-GFP	97.2 ± 1.6% overlap (n=5)	Founder # NIDA108
Kcnip2-CreER	RP23-146N4-CreERT2	x	5'CTTCTGCTCCGCTCTCACTT3' 5'TAAGCAATCCCCAGAAATGC3'	P21-23 (2mg/day)	overlap with BAC-GFP	98.4 ± 0.9% overlap (n=3)	Founder #NIDA099
PKCγ^{CreER}	x	ATG-CreERT2	5'GCCCCTGTCCTTCCTATCTC3' 5'AATCGCGAACATCTTCAGGT3' 5'GGTCAGTGCAAAGAGGGGTA3'	P15 (2mg)	homozygosity test with PCR	loss of WT band	See Experimetal Procedures
PV^{FlpO}	x	STOP-2a-FlpO	5'TGTTTCTCCAGCATTTCCAG3' 5'GGATGCTTGCCGAAGATAAG3' 5'CTGAGCAGCTACATCAACAGG3'	x	overlap with PV antibody	95.5 ± 3.3% overlap (n=3)	JAX#022730
Rorβ^{CreER}	x	ATG-CreERT2	5'AGCGGAATTTTTGGGTTCTC3' 5'CGCGCTTATAGACTGCTCCT3' 5'GCAAACGGACAGAAGCATTT3'	P18 (2mg)	homozygosity test with PCR	loss of WT band	See Experimental Procedures

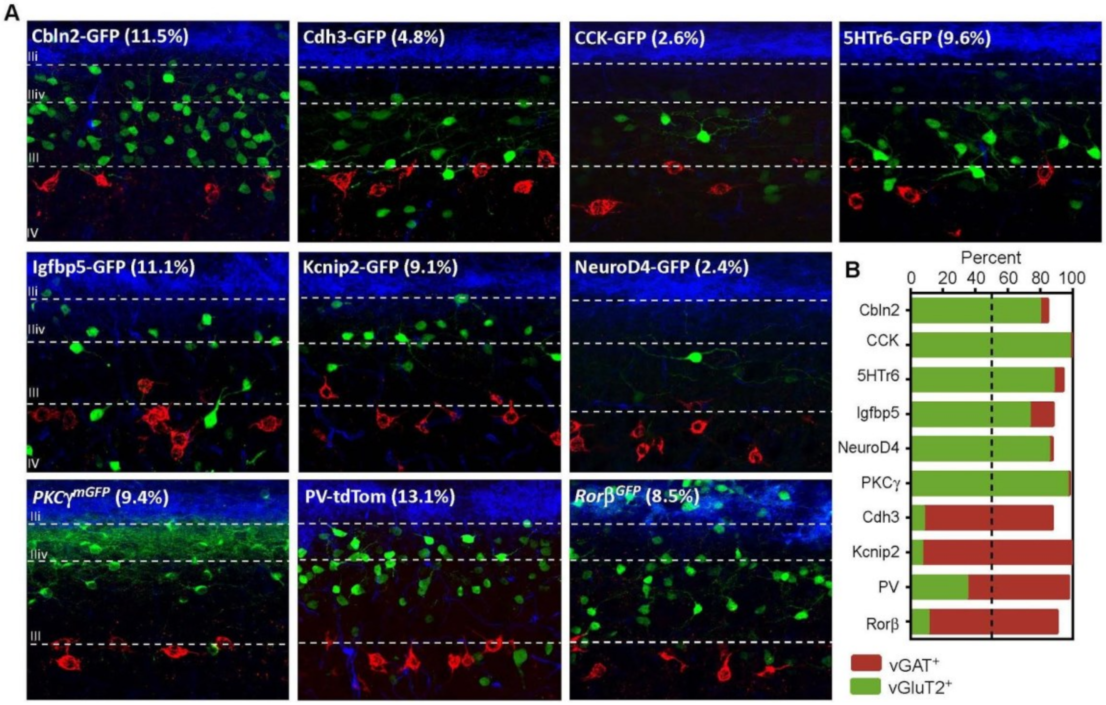

Figure 3.3. An LTMR-RZ genetic toolkit.
(**A**) Sagittal sections of the LTMR-RZ from the 10 interneuron GFP/Tomato mouse lines. Fluorescent reporters are in green. CTB labeled PSDCs in red. IB4 in blue. Percent of the LTMR-RZ in parentheses. Percentages calculated from total NeuN$^+$ cells in the LTMR-RZ. Cbln2: 633 GFP$^+$ neurons counted (n=3 animals); Cdh3: 201 GFP$^+$ neurons counted (n=3 animals); CCK: 243 GFP$^+$ neurons counted (n=6 animals); 5HTr6: 350 GFP$^+$ neurons counted (n=3 animals); Igfbp5: 592 GFP$^+$ neurons counted (n=3 animals); Kcnip2: 487 GFP$^+$ neurons counted (n=3 animals); NeuroD4: 155 GFP$^+$ neurons counted (n=4 animals); PKCγ: 471 PKCγ$^+$ neurons counted (n=3 animals); PV: 320 TdTom$^+$ neurons counted (n=3 animals); Rorβ: 437 GFP$^+$ neurons counted (n=3 animals). (**B**) Neurotransmitter quantification for the 10 interneuron lines. Excitatory and inhibitory neurons labeled with *vGluT2*^{iresCre} and *vGAT*^{iresCre} mouse lines respectively. For specific mouse crosses see Experimental Procedures.

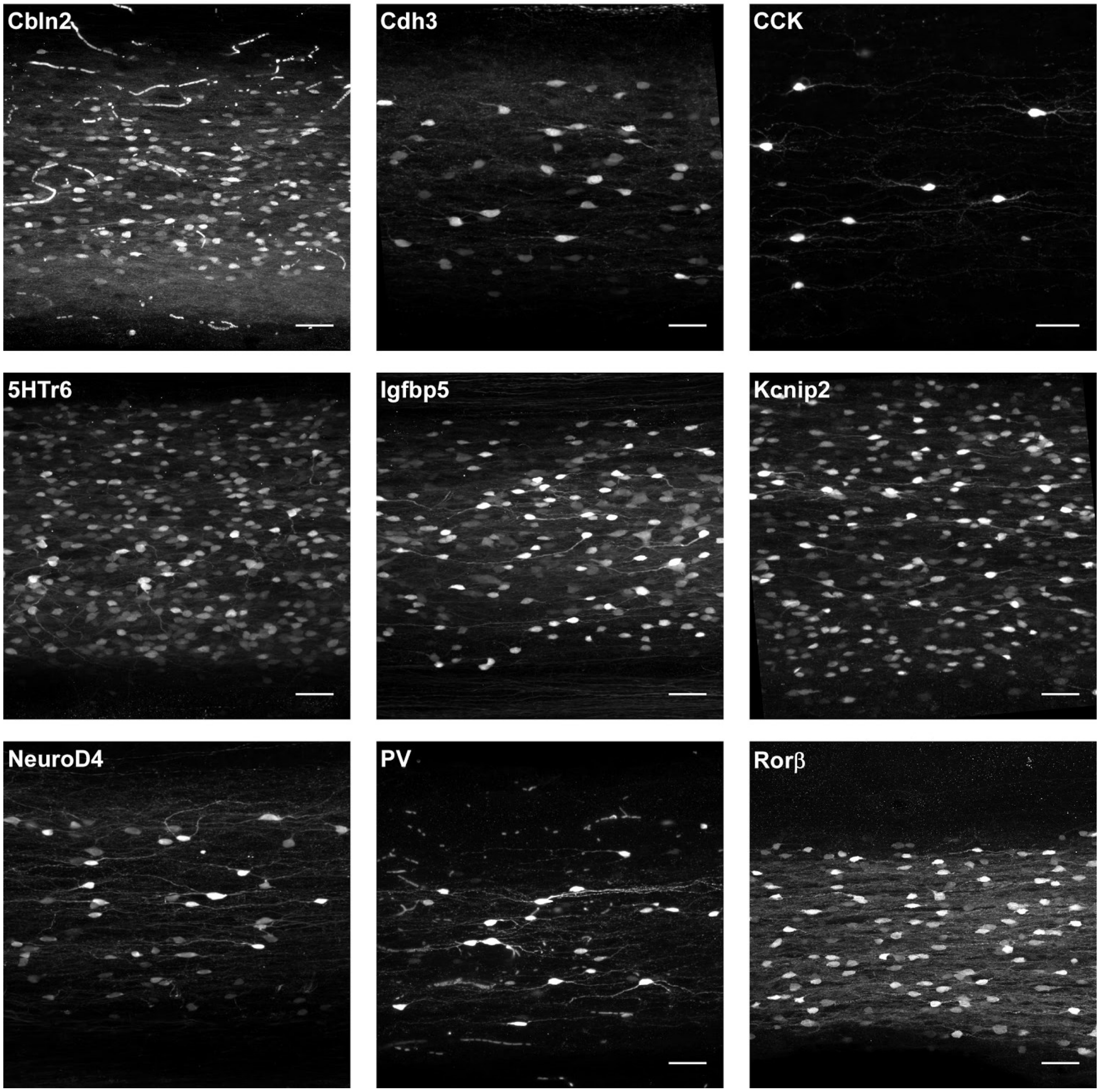

Figure 3.4. Whole-mount staining of interneurons of the LTMR-RZ reveals most project along the rostrocaudal axis.
Representative images of whole mount immunostaining of spinal cords to label genetically-targeted interneuron populations of the LTMR-RZ. Scale = 50μm.

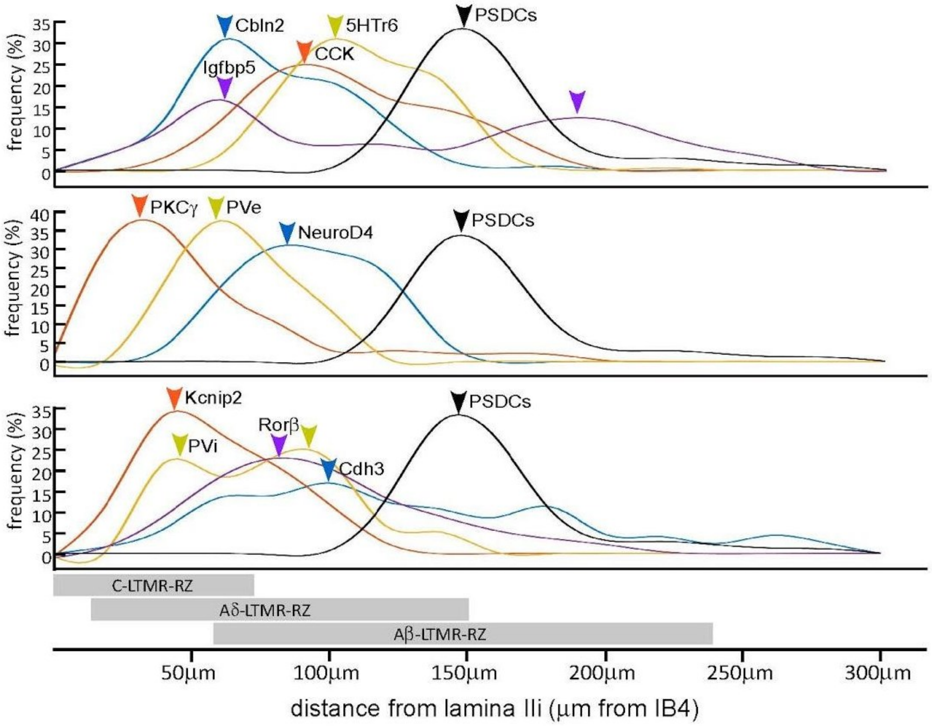

Figure 3.5. Distribution of genetically labeled interneuron populations across the LTMR-RZ.

Smoothened cell body histogram distribution of LTMR-RZ interneuron lines (location of somas). Arrows indicate peak frequency of soma location within the LTMR-RZ.

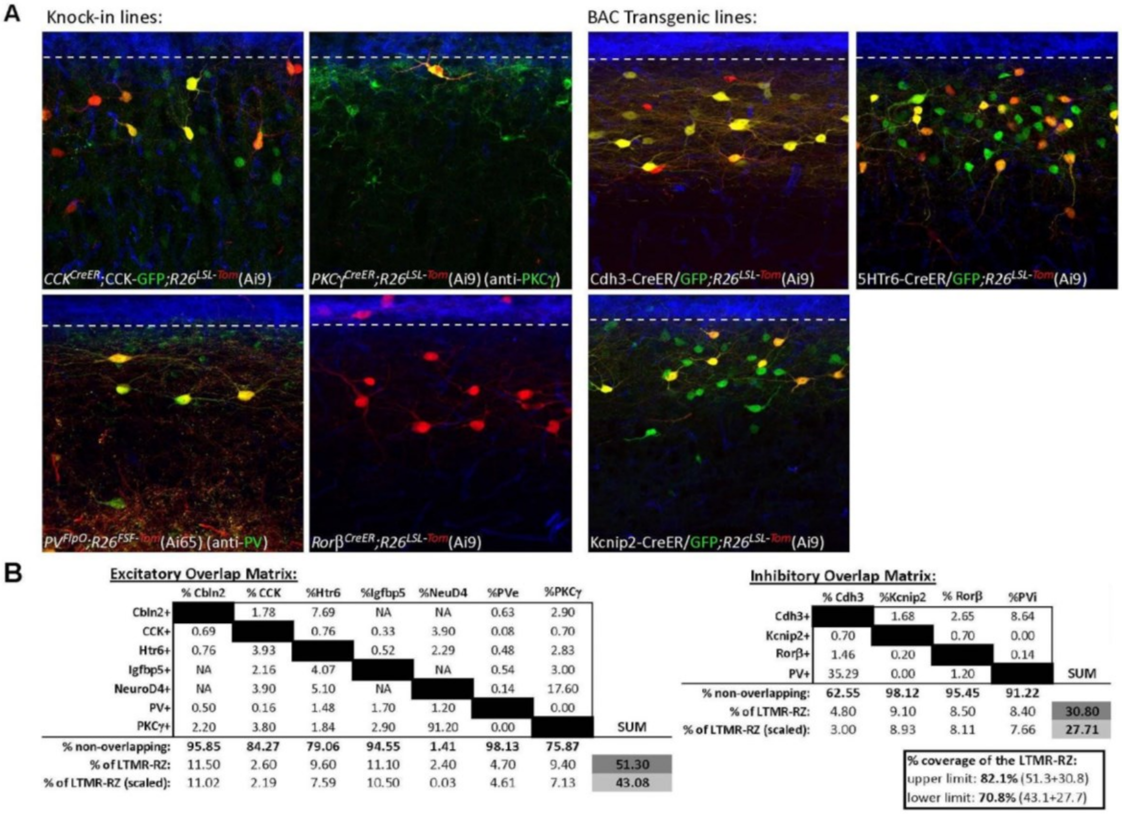

Excitatory Overlap Matrix:

	% Cbln2	% CCK	%Htr6	%Igfbp5	%NeuD4	%PVe	%PKCγ	
Cbln2+	■	1.78	7.69	NA	NA	0.63	2.90	
CCK+	0.69	■	0.76	0.33	3.90	0.08	0.70	
Htr6+	0.76	3.93	■	0.52	2.29	0.48	2.83	
Igfbp5+	NA	2.16	4.07	■	NA	0.54	3.00	
NeuroD4+	NA	3.90	5.10	NA	■	0.14	17.60	
PV+	0.50	0.16	1.48	1.70	1.20	■	0.00	
PKCγ+	2.20	3.80	1.84	2.90	91.20	0.00	■	SUM
% non-overlapping:	**95.85**	**84.27**	**79.06**	**94.55**	**1.41**	**98.13**	**75.87**	
% of LTMR-RZ:	11.50	2.60	9.60	11.10	2.40	4.70	9.40	**51.30**
% of LTMR-RZ (scaled):	11.02	2.19	7.59	10.50	0.03	4.61	7.13	**43.08**

Inhibitory Overlap Matrix:

	% Cdh3	%Kcnip2	% Rorβ	%PVi	
Cdh3+	■	1.68	2.65	8.64	
Kcnip2+	0.70	■	0.70	0.00	
Rorβ+	1.46	0.20	■	0.14	
PV+	35.29	0.00	1.20	■	SUM
% non-overlapping:	**62.55**	**98.12**	**95.45**	**91.22**	
% of LTMR-RZ:	4.80	9.10	8.50	8.40	**30.80**
% of LTMR-RZ (scaled):	3.00	8.93	8.11	7.66	**27.71**

% coverage of the LTMR-RZ:
upper limit: **82.1%** (51.3+30.8)
lower limit: **70.8%** (43.1+27.7)

Figure 3.6. Second generation recombinase tools for genetically identified and largely non-overlapping populations of LTMR-RZ interneurons.
(**A**) Sagittal sections of the LTMR-RZ from CreER/FlpO knock-in animals (left) and BAC-transgenic CreER lines (right). IB4 binding in blue. Animal genotype on the bottom left corner. Recombinase activity is depicted in red. Antibody binding, in the case for PKCγ and PV, or overlap with fluorescent reporter lines depicted in green. Also, see Figure S7B. (**B**) Excitatory and inhibitory overlap matrix used to calculate the percent coverage of the LTMR-RZ represented by the eleven genetically labeled interneuron lines. Each box in the matrix represents a unique mouse cross to assess the amount of overlap between the two mouse lines. For each mouse line, the "% non-overlapping" is derived by adding the percent overlap (ie each matrix box in the column) and subtracting it from 100. The "% of the LTMR-RZ" are as depicted in Figure 3.3A for each individual line, the sum of which represents the coverage of the LTMR-RZ without consideration for potential overlap (51.3%+30.8%=82.1%). The "% of LTMR-RZ (scaled)" represents the percentage of the LTMR-RZ that each line represents scaled for the overlapping population. The sum of this scaled percentage represents the coverage of the LTMR-RZ taking into consideration the amount of overlap across each mouse line (43.1%+27.7%=70.8%). See experimental procedures for mouse crosses, at least 100 GFP$^+$ neurons counted per animal, at least 3 animals per cross. Percent overlap with PVe and PVi is calculated as 36% excitatory and 64% inhibitory. NA: mouse lines not available for compatible crosses.

3.3. LTMR-RZ interneurons contribute to tactile perception

Our characterization of recombinase tools that label LTMR-RZ interneuron subtypes also resulted in the identification of “large lineage” genetic tools, including *CCK*^{iresCre} and *Rorβ*^{iresCre}, which label 27% and 18% of LTMR-RZ interneurons, respectively (Figure 3.7A, (Taniguchi et al., 2011). Neurotransmitter characterization of *CCK*^{iresCre} and *Rorβ*^{iresCre} LTMR-RZ lineages revealed that *CCK*^{iresCre}-labeled neurons are 92% excitatory while *Rorβ*^{iresCre}-labeled neurons are 62% inhibitory (Figure 3.7B). Thus, these *CCK*^{iresCre} and *Rorβ*^{iresCre} lineage tools are useful for functionally manipulating large cohorts of excitatory and inhibitory LTMR-RZ interneurons, enabling us to ask whether LTMR-RZ interneurons contribute to tactile perception. In order to restrict neuronal manipulations to the spinal cord, as most of the genes identified, including *CCK* and *Rorβ*, are expressed in supraspinal centers (Taniguchi et al., 2011) and also in non-neuronal tissues (Chaudhri et al., 2006), we developed an intersectional genetic strategy by generating a neural specific enhancer Cdx2-FlpO mouse line (Cdx2-NSE-FlpO, (Coutaud and Pilon, 2013a)) that expresses FlpO in the spinal cord, but not in the brain, skin or internal organs (Figure 3.7C-D). Thus, intersectional inactivation of large LTMR-RZ lineages using either *CCK*^{iresCre} and *Rorβ*^{iresCre} together with Cdx2-NSE-FlpO and the previously characterized dual recombinase tetanus toxin mouse line, *RC:PFtox* (Kim et al., 2009; Niederkofler et al., 2016) was done to determine the role of LTMR-RZ interneurons in tactile perception (Figure 3.8A-B).

To assess texture discrimination abilities in mice, we used a texture-specific novel object recognition test (NORT), ‘textured NORT’, utilizing acrylic cubes (4 cm^3) that differ only in texture (rough or smooth) (Orefice et al., 2016). In this assay, mice are first exposed to two identical cubes for ten minutes. In the subsequent testing phase, one object is replaced with a novel object that differs only in texture. As observed previously, control mice preferentially explored the cube with a novel texture during the test phase, indicating an ability to discriminate between the familiar and novel textured objects and hence perception of textured surfaces. In contrast, mice in which either *CCK*^{iresCre} or *Rorβ*^{iresCre} labeled interneuron lineages were silenced using the intersectional genetic strategy did not show a preference for the novel textured object in this assay (Figure 3.9A). This deficit does not reflect a lack of tactile exploration, as both control and mutant littermates spent comparable amounts of time investigating the objects during the testing phase of this assay (Figure 3.9C). Furthermore, novelty seeking behavior is not impaired in mutant animals, as both control and mutant mice showed a significant preference for novel objects that differ in color and shape (Figure 3.9A).

Next, we asked whether the LTMR-RZ contributes to hairy skin sensitivity using a tactile prepulse inhibition of the startle reflex assay (tactile PPI), in which a light air puff prepulse (1.5PSI) is applied to back hairy skin followed by a startle pulse of broadband white noise (125dB) to elicit an acoustic startle reflex (Orefice et al., 2016). As with acoustic PPI, a light air puff prepulse reduced the magnitude of an acoustic startle response in control animals (Figure 3.9B). However, mutant mice in which either *CCK*^{iresCre} or *Rorβ*^{iresCre} lineages were silenced exhibited a reduction in tactile PPI performance (Figure 3.9B). This deficit is specific to tactile responses as both control and mutant littermates performed comparably in the acoustic version of PPI, where the prepulse is a broadband white noise of 15 decibels (Figure 3.9B). Aside from these specific texture discrimination and hairy skin sensitivity defects, both mutant lines exhibited normal gross locomotive behaviors as well as responses to temperature (Figure 3.9F). Thus, excitatory and inhibitory LTMR-RZ interneuron subtypes are required for texture discrimination as well as normal hairy skin tactile sensitivity, implicating LTMR-RZ interneurons as critical for innocuous touch perception. These behavioral findings motivated an extensive analysis of the morphological, physiological and synaptic properties of the 11 genetically labeled interneuron subtypes, and their relationships to ascending projection pathways, to define the nature of LTMR-RZ circuits that underlie touch information processing in the spinal cord dorsal horn.

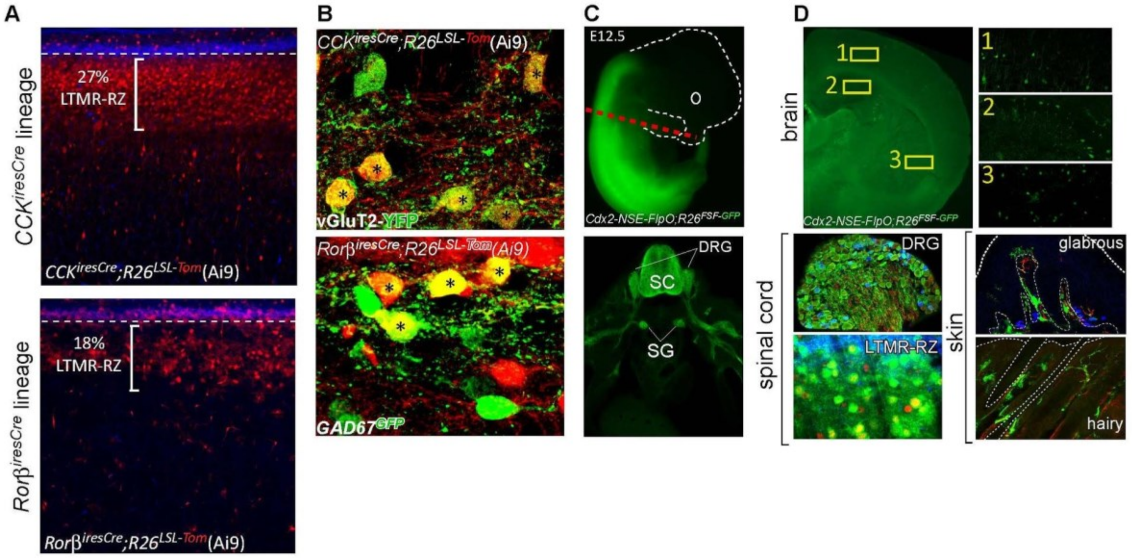

Figure 3.7. The characterization of mouse lines to target LTMR-RZ lineages and a neural-specific CDX2-FlpO.
(**A**) Sagittal spinal cord section from a $CCK^{iresCre}$;$R26^{LSL\text{-}tdTom}$(Ai9) mouse (top) and an $Ror\beta^{iresCre}$;$R26^{LSL\text{-}TdTom}$(Ai9) mouse (bottom) LTMR-RZ outlined with a white bracket. IB4 lamina IIiv in blue. (**B**) Neurotransmitter characterization of $CCK^{iresCre}$ and $Ror\beta^{iresCre}$ lineages in the LTMR-RZ. Asterisk denotes overlap. (**C**) Cdx2-NSE-FlpO;$R26^{FSF\text{-}GFP}$ E12.5 embryo depicting caudal expression of FlpO (top). Cross section at red dotted line (bottom). Early in development Cdx2-NSE-FlpO recombination is restricted to posterior neural plate, prospective spinal cord territory. See experimental procedures and (Coutaud and Pilon, 2013a). Note specific FlpO expression in caudal neuronal tissues (spinal cord, SC; dorsal root ganglia, DRG; sympathetic ganglia, SG) but not in brain, internal organs or skin. (**D**) Adult characterization of brain, spinal cord and skin tissue from a Cdx2-NSE-FlpO; $R26^{FSF\text{-}GFP}$ animal. Adult brain characterization reveals very sparse FlpO activity in the brain (top). Yellow insets show very low levels of recombination in the cortex (1), hippocampus (2), and striatum (3). Adult DRG and spinal tissue show near complete FlpO recombination (bottom left, IB4 binding in blue). Adult glabrous and hairy skin sections (bottom right) show no FlpO activity in skin cells (outlined in white dotted lines) including Troma1+ merkel cells depicted in blue for the glabrous skin inset. Neurofilament 200 staining in red, GFP staining in green.

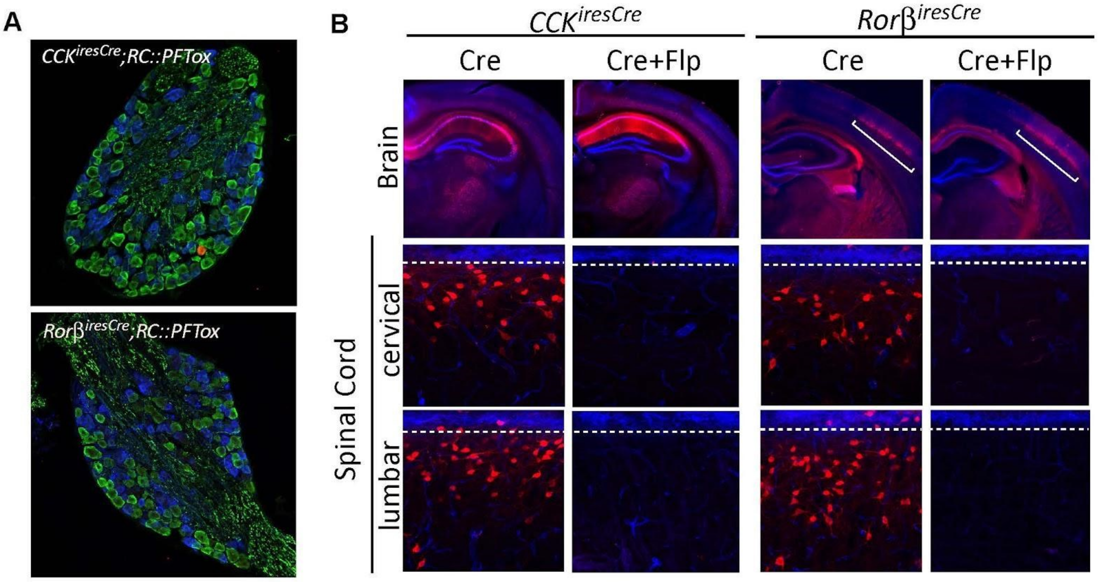

Figure 3.8. Confirmation of specific recombination in animals used for behavioral analysis.

(**A**) DRG cross-sections from *$CCK^{iresCre}$;RC::PFtox* (top) and *$Ror\beta^{iresCre}$;RC::PFtox* (bottom) animals. *Cre* recombination of *RC::PFtox* results in *mCherry* expression, depicted in red. Note very minimal DRG Cre recombination of *$CCK^{iresCre}$* (top) and no DRG Cre recombination of *$Ror\beta^{iresCre}$* (bottom). IB4 binding in blue, Neurofilament-200 staining in green. (**B**) Cross-sections through brain and cervical/lumbar spinal cords from *$CCK^{iresCre}$;RC::PFtox, $CCK^{iresCre}$;*Cdx2-NSE-FlpO*;RC::PFtox*, *$Ror\beta^{iresCre}$;RC::PFtox and $Ror\beta^{iresCre}$;*Cdx2-NSE-FlpO*;RC::PFtox* animals (left to right). Cre recombination of *RC::PFtox* results in mCherry expression in brain and spinal cord, depicted in red. Combined Cre and Flp recombination from Cdx2-NSE-FlpO of *RC::PFtox* results in loss of mCherry expression and expression of Tetanus Toxin specifically in spinal cord but not in the brain. For brain sections NeuN is depicted in blue, for spinal cord sections IB4 binding is depicted in blue.

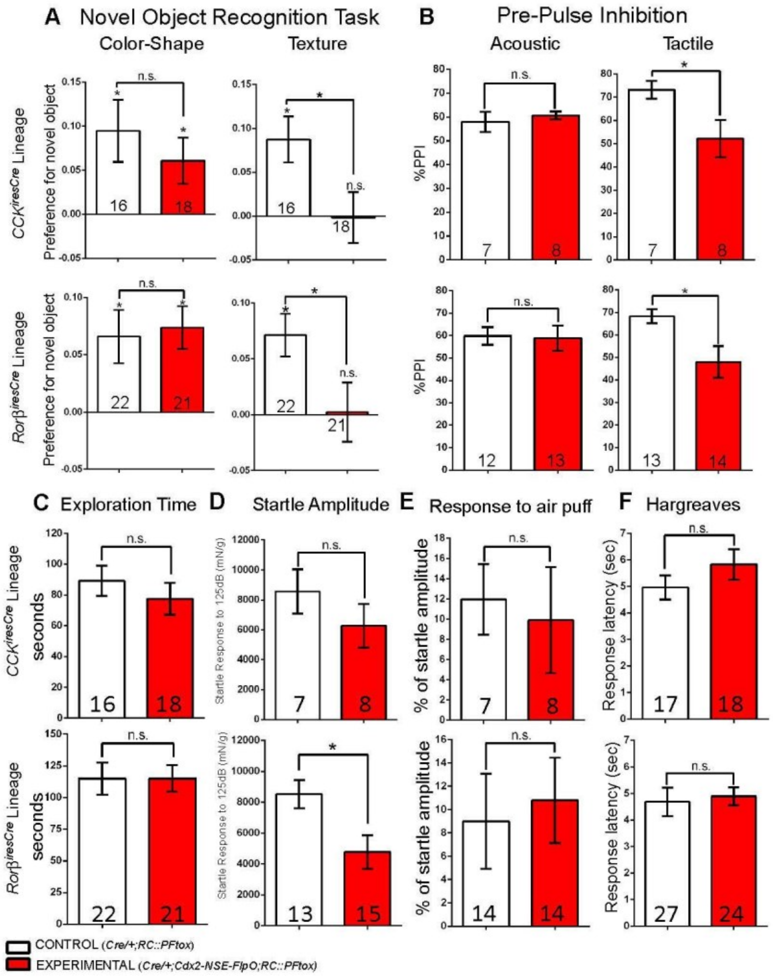

Figure 3.9. Contributions of LTMR-RZ interneurons to tactile perception.
(**A-F**) Behavior assays. *CCK*^{iresCre};Cdx2-NSE-FlpO*;RC::PFtox* (top panels), *Rorβ*^{iresCre};Cdx2-NSE-FlpO*;RC:;PFtox* (bottom panels). (**A**) Discrimination indices for color-shape NORT (left) and texture NORT (right). A positive value indicates a preference for the novel object compared to the familiar object. $*p<0.05$. (**B**) Percent inhibition of startle response to 125dB noise in control and mutant littermates when the startle noise is preceded by a 15dB prepulse (left) or a light air puff of 1.5PSI (right). $*p<0.05$. For *CCK*^{iresCre};Cdx2-NSE-FlpO*;RC::PFTox* animals (top) 100ms ISI tactile PPI results displayed (main effect of genotype across all ISIs, two-way ANOVA: $*p<0.05$, F[1,65]=8.578). For *Rorβ*^{iresCre};Cdx2-NSE-FlpO*;RC::PFTox* (bottom) 50ms ISI tactile PPI displayed (main effect of genotype across all ISIs, two-way ANOVA: $*p<0.05$, F[1,125]=5.717). (**C**) Exploration time during texture NORT. (**D**) Startle amplitude to 125dB noise during PPI test. *Rorβ*^{iresCre};Cdx2-NSE-FlpO*;RC::PFtox* mutant animals display a much lower startle response than control littermates, indicating some motor deficits ($*p<0.05$). (**E**) Response to a light air puff stimulus alone. Responses are expressed as a percent of startle response to a 125-dB noise. (**F**) Hargreaves temperature sensitivity assay.

3.4. LTMR-RZ interneuron subtypes exhibit distinctive physiological and morphological properties

We next aimed to establish the morphological and physiological properties of the 11 genetic subtypes to define features that distinguish them and to gain insight into the cellular and physiological nature of LTMR-RZ excitatory and inhibitory components. For morphological comparisons, 351 individual neurons representing all 11 genetically labeled subtypes were reconstructed using Neurolucida (Figures 3.10A and 3.11A), and 46 parameters that define the morphological features for each neuron were analyzed, including cell body size, dendrite length, spine density, dendrite complexity using various Sholl-based metrics, and Branching Index measurements (Figure 3.12A-D, see Experimental Procedures). This analysis revealed that excitatory LTMR-RZ interneuron subtypes tend to have smaller cell bodies (Figure 3.12A) and more complex neurite morphologies (Figure 3.12C-D), and greater spine densities (Figure 3.12B) than the inhibitory subtypes. Importantly, linear discriminant analysis (LDA) using the 26 most salient morphological parameters suggests that each genetically labeled interneuron subtype exhibits a unique, distinguishable combination of morphological features (Figure 3.10C and 3.11C). We used these combinations of morphological features to create linear classifiers that recognize interneuron subtypes with 83% and 88% accuracy for excitatory and inhibitory interneuron subtypes, respectively (Figure 3.10D and 3.11D). By removing specific, related groups of variables from the LDA to assess their importance in classifier performance, we found that dendrite morphology parameters were most important to distinguish excitatory interneurons from one another, whereas spine density was most important to distinguish inhibitory interneuron subtypes (Figure 3.12E).

We next asked whether the 11 genetically and morphologically distinct interneuron subtypes also exhibit unique intrinsic physiological properties. For this, whole cell patch clamp recordings were performed for each LTMR-RZ interneuron subtype (Figure 3.10B and 3.11B, n=128 neurons). This analysis revealed that each of the seven types of physiological profiles observed in LTMR-RZ interneuron random recordings (Figure 3.2) was represented within the genetically-labeled cohorts, with six profiles associated with excitatory interneuron subtypes (Figure 3.10B,B') and five with inhibitory subtypes (Figure 3.11B, Figure 3.13A). Moreover, each of the genetically labeled LTMR-RZ interneuron subtypes exhibited characteristic firing patterns. For example, within the excitatory cohort, Cbln2$^+$ interneurons are the only population that exhibited initial bursting firing properties and PKCγ$^+$ interneurons are the only excitatory subtype that exhibited delayed spiking properties (Figure 3.10B). Although reluctant firing profiles were not found in LTMR-RZ random recordings, they represent the most common profile for the excitatory 5HTr6$^+$ interneurons (Figure 3.10B). Furthermore, although excitatory PV$^+$ LTMR-RZ interneurons showed a marked difference in morphology when compared to their inhibitory counterparts, PVe and PVi interneurons had virtually indistinguishable physiological profiles, with both populations exhibiting tonic firing properties (Figures 3.10B and 3.11B). In contrast to the excitatory cohort, LTMR-RZ inhibitory interneuron subtypes uniquely exhibited either tonic (PVi), delayed (Kcnip2$^+$ and Rorβ$^+$), or gap firing properties (Cdh3$^+$) (Figure 3.11B). In sum, the LTMR-RZ is comprised of seven excitatory and four inhibitory interneuron subtypes, each of which is readily distinguished by a unique combination of morphological and physiological properties.

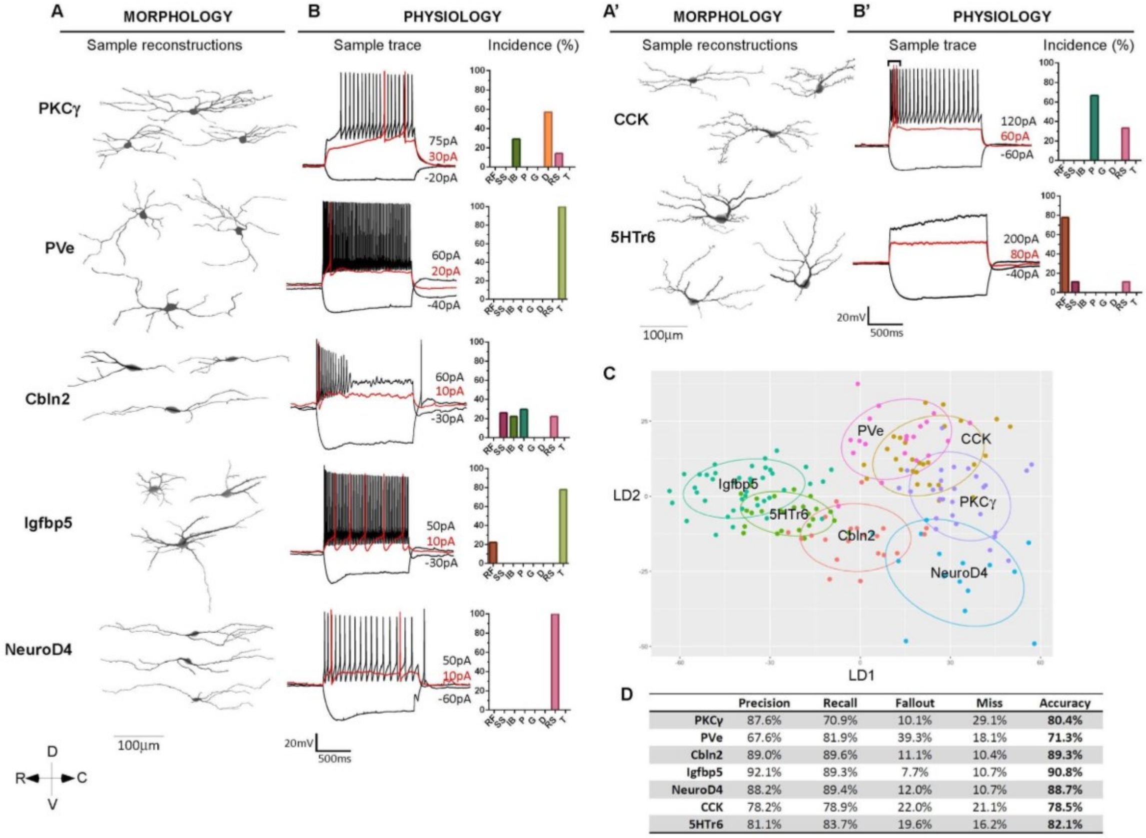

	Precision	Recall	Fallout	Miss	Accuracy
PKCγ	87.6%	70.9%	10.1%	29.1%	**80.4%**
PVe	67.6%	81.9%	39.3%	18.1%	**71.3%**
Cbln2	89.0%	89.6%	11.1%	10.4%	**89.3%**
Igfbp5	92.1%	89.3%	7.7%	10.7%	**90.8%**
NeuroD4	88.2%	89.4%	12.0%	10.7%	**88.7%**
CCK	78.2%	78.9%	22.0%	21.1%	**78.5%**
5HTr6	81.1%	83.7%	19.6%	16.2%	**82.1%**

Figure 3.10. Morphological and physiological characterization of excitatory LTMR-RZ interneurons.

(**A** and **A'**) Sample Neurolucida reconstructions from the seven excitatory LTMR-RZ interneuron lines. PKCγ (n=31); Cbln2 (n=25); NeuroD4 (n=17); PVe (n=28); CCK (n=33); 5HTr6 (n=29); Igfbp5 (n=41). For mouse crosses see Experimental Procedures. (**B** and **B'**) Sample action potential discharge patterns (left) during somatic injection of hyperpolarizing and depolarizing currents steps of increasing magnitude (black traces, rheobase trace in red, current step magnitude noted in pA). Percent quantification of firing properties (right). RF= Reluctant Firer, SS= single spiking, IB= Initial Bursting, P= Phasic, G= Gap, D= Delayed, RS= Regular Spiking; T= Tonic. Total number of neurons recorded for PKCg (n=7); Cbln2 (n=27); NeuroD4 (n=10); PVe (n=10); CCK (n=10); 5HTr6 (n=10); Igfbp5 (n=9). For mouse crosses see Experimental Procedures. (**C**) Representative plot of an excitatory interneuron training set chosen at random for linear discriminant analysis (LDA), demonstrating grouping of excitatory interneuron classes when described by the first two linear discriminants. Ellipses demarcate significant 95% confidence intervals for each interneuron subtype. (**D**) Performance of an excitatory interneuron classifier generated using linear discriminant analysis (LDA). Classifier predictive performance is quantified by precision (positive predictive value), recall (true positive value), fallout (false positive rate), miss (false negative rate), and accuracy (true positive and true negative rate).

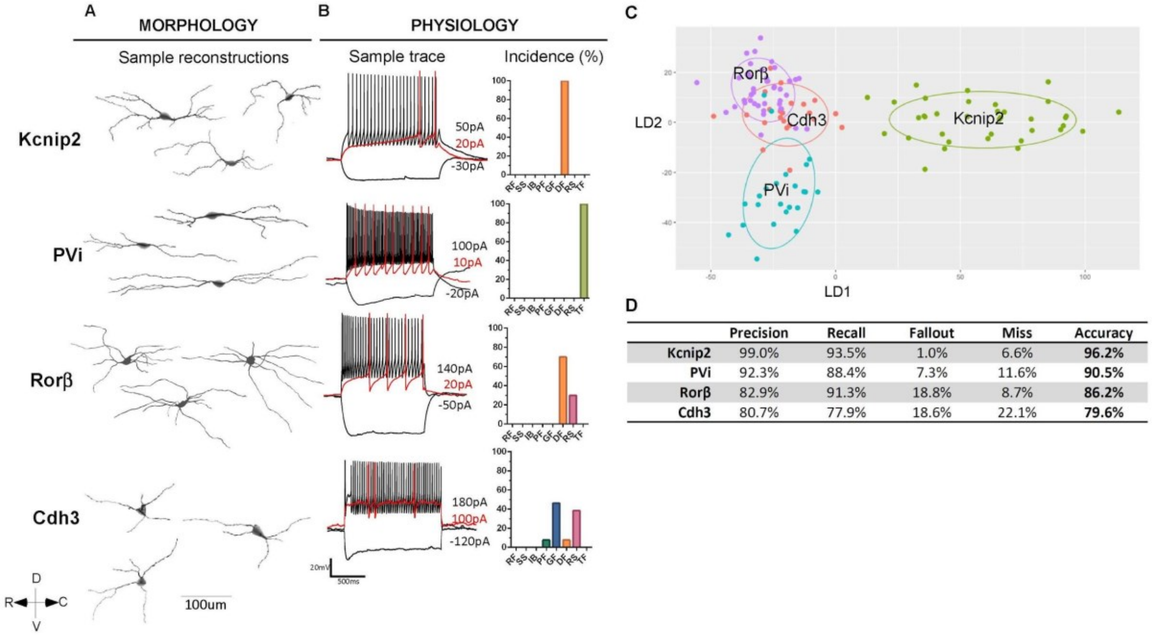

	Precision	Recall	Fallout	Miss	Accuracy
Kcnip2	99.0%	93.5%	1.0%	6.6%	**96.2%**
PVi	92.3%	88.4%	7.3%	11.6%	**90.5%**
Rorβ	82.9%	91.3%	18.8%	8.7%	**86.2%**
Cdh3	80.7%	77.9%	18.6%	22.1%	**79.6%**

Figure 3.11. Morphological and physiological characterization inhibitory LTMR-RZ interneurons.

(**A**) Sample Neurolucida reconstructions from the four inhibitory LTMR-RZ interneuron lines. PVi (n=31); Kcnip2 (n=41); Rorβ (n=43); Cdh3 (n=32). For mouse crosses see Experimental Procedures. (**B**) Sample action potential discharge patterns (left) during somatic injection of hyperpolarizing and depolarizing currents steps of increasing magnitude (black traces, rheobase trace in red, current step magnitude noted in pA). Percent quantification of firing properties (right). RF= Reluctant Firer, SS= single spiking, IB= Initial Bursting, P= Phasic, G= Gap, D= Delayed, RS= Regular Spiking; T= Tonic. Total number of neurons recorded for PVi (n=9); Kcnip2 (n=12); Rorβ (n=12); Cdh3 (n=12). For mouse crosses see Experimental Procedures. (**C**) Representative plot of an inhibitory interneuron training set chosen at random for linear discriminant analysis (LDA), demonstrating grouping of excitatory interneuron classes when described by the first two linear discriminants. Ellipses demarcate significant 95% confidence intervals for each interneuron subtype. (**D**) Performance of an inhibitory interneuron classifier generated using linear discriminant analysis (LDA). Classifier predictive performance is quantified by precision (positive predictive value), recall (true positive value), fallout (false positive rate), miss (false negative rate), and accuracy (true positive and true negative rate).

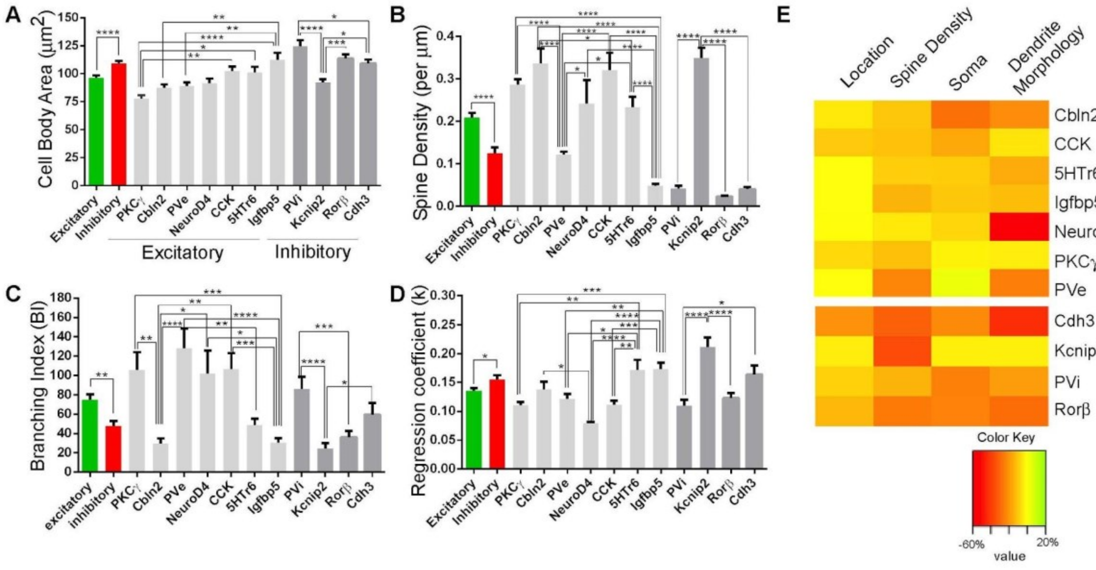

Figure 3.12. Additional morphometric characterization of 11 interneurons of the LTMR-RZ.
(**A**) Cell body area summary for excitatory and inhibitory subtypes. For excitatory vs. inhibitory comparison: (unpaired t-test ****$p<0.0001$). For excitatory group: (one-way ANOVA: $p<0.0001$, F[6,201]=6.562). For inhibitory group: (one-way ANOVA: $p<0.0001$, F[3,142]=12.47). Post-hoc Tukey's test: *$p<0.05$, **$p<0.01$, ***$p<0.0005$, ****$p<0.0001$. (**B**) Spine density measurements for excitatory and inhibitory subtypes. For excitatory vs. inhibitory comparison: (unpaired t-test **$p<0.0001$). For excitatory group: (one-way ANOVA: $p<0.0001$, F[6,187]=24.39). For inhibitory group: (one-way ANOVA: $p<0.0001$, F[3,125]=132.1). Post-hoc Tukey's test: *$p<0.05$, ****$p<0.0001$. (**C**) Branching index (BI) summary describing ramification patterns for excitatory and inhibitory subtypes. BI values are positively correlated to branching complexity. For excitatory vs. inhibitory comparison: (unpaired t-test **$p<0.005$). For excitatory group: (one-way ANOVA: $p<0.0001$, F[6,194]=9.207). For inhibitory group: (one-way ANOVA: $p<0.0001$, F[3,138]=8.952). Post-hoc Tukey's test: *$p<0.05$, **$p<0.005$, ***$p<0.0005$, ****$p<0.0001$. (**D**) Regression Coefficient (k) summary for excitatory and inhibitory cohorts describing one sholl-based metric of neurite complexity. k values are negatively correlated to branching complexity. For excitatory vs. inhibitory comparison: (unpaired t-test *$p<0.05$). For excitatory group: (one-way ANOVA: $p<0.0001$, F[6,194]=9.28). For inhibitory group: (one-way ANOVA: $p<0.0001$, F[3,138]=13.17). Post-hoc Tukey's test: *$p<0.05$, **$p<0.005$, ***$p<0.0005$, ****$p<0.0001$. (**E**) Heatmap of changes in classifier accuracy for excitatory and inhibitory interneurons when metrics related to cell location, soma morphology, dendritic spines, or dendrite morphology are omitted from LDA (see Experimental Procedures for detailed metric membership in each category). Heatmap quantities are displayed as percent change in accuracy (true positive and true negative rate) when one of these categories are omitted, as compared to when all metrics are used to train the linear discriminant model.

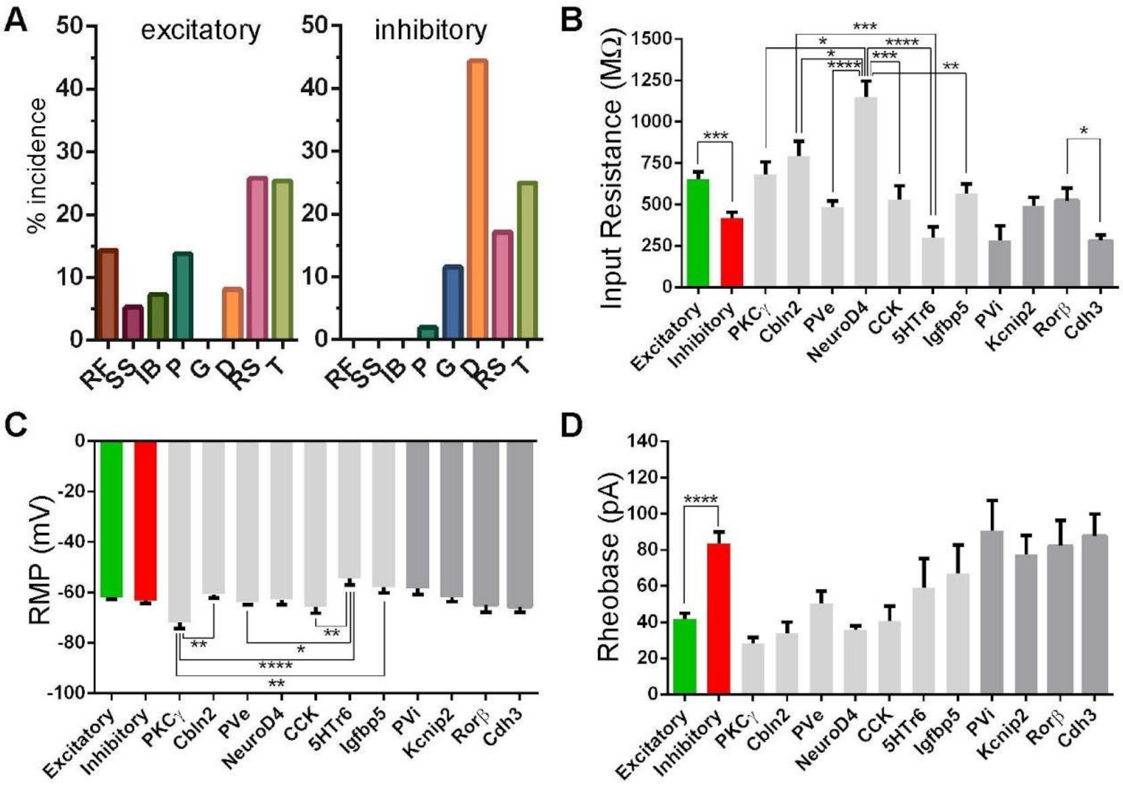

Figure 3.13. Additional physiological characterization of 11 interneurons of the LTMR-RZ.

(**A**) Percent quantification of action potential discharge patterns for excitatory (left) and inhibitory (right) cohorts. RF= Reluctant Firer, SS= single spiking, IB= Initial Bursting, P= Phasic, G= Gap, D= Delayed, RS= Regular Spiking; T= Tonic. (**B**) Input Resistance for excitatory and inhibitory subtypes. For excitatory vs. inhibitory cohort comparison: (unpaired t-test ***$p<0.0005$). For excitatory group: (one-way ANOVA: $p<0.0001$, F[6,70]=9.516). For inhibitory group: (one-way ANOVA: $p<0.05$, F[3,39]=3.950). Post-hoc Tukey's test: *$p<0.05$, **$p<0.005$, ***$p<0.0005$, ****$p<0.0001$. (**C**) Resting membrane potential for excitatory and inhibitory subtypes. For excitatory vs. inhibitory cohort comparison: (unpaired t-test: n.s.). For excitatory group: (one-way ANOVA: $p<0.001$, F[6,10]=5.966). For inhibitory group: (one-way ANOVA: $p=0.1918$, F[3,39]=1.658). Post-hoc Tukey's test: *$p<0.05$, **$p<0.01$, ****$p<0.0001$. (**D**) Rheobase currents for excitatory and inhibitory subtypes. For excitatory vs. inhibitory cohort comparison: (unpaired t-test ****$p<0.0001$). For excitatory group: (one-way ANOVA: $p=0.0497$, F[6,61]=2.255). For inhibitory group: (one-way ANOVA: $p=0.9032$, F[3,37]=0.1891).

CHAPTER 4: EXPERIMENTAL RESULTS[2]

The Synaptic Architecture of the Mechanosensory Dorsal Horn

4.1. The deep dorsal horn is defined by overlapping LTMR and cortical inputs

We localized initial sites of innocuous touch information processing by visualizing LTMR subtype endings in the spinal cord dorsal horn. The organization of synaptic inputs of C-LTMRs, Aδ-LTMRs, Aβ RA-LTMRs, Aβ SAI-LTMRs, and Aβ Field-LTMRs in the mouse dorsal horn was assessed by taking advantage of LTMR-CreER and intersectional mouse genetic tools (Table 2.1, Figure 4.1A, (Bai et al., 2015; Li et al., 2011; Luo et al., 2009; Rutlin et al., 2015). This analysis showed that LTMR inputs in the dorsal horn are organized in a highly overlapping fashion spanning ~250μm immediately below $IB4^+$ lamina IIi, in a region of the spinal cord dorsal horn which we have termed the LTMR-Recipient Zone (LTMR-RZ, Figure 4.1E). We estimate that the total number of C-LTMR, Aδ-LTMR and individual Aβ-LTMR subtype synapses within the LTMR-RZ are comparable (See Experimental Procedures and Figure 4.2), suggesting equal synaptic allocation of LTMR subtypes within this spinal cord region. Interestingly, sensory neurons and locally projecting interneurons together account for only ~70% of total glutamatergic excitatory inputs to the LTMR-RZ (Figure 4.1C). Thus, we next sought to uncover additional synaptic inputs that contribute to the excitatory drive in the LTMR-RZ.

---

[2] The work presented in this section is included in a manuscript currently under review at *Cell* (Abraira and Kuehn *et al*.). In this body of work, on which EDK is a co-first author, EDK performed the majority of the synaptic characterization.

In other sensory systems, cortical inputs to CNS relay regions play a crucial role in sensory processing (Fanselow and Nicolelis, 1999; Ortuño et al., 2014; Otazu et al., 2015; Xiao and Suga, 2002), and yet relatively little is known about the organization and function of cortical inputs to the dorsal horn. Historically, much emphasis has been placed on the role of corticospinal neurons in transmission of motor commands by direct and indirect modulation of the ventral horn (Greig et al., 2013). However, a large fraction of corticospinal neurons originate in the somatosensory cortex and preferentially innervate the dorsal horn of species from rodents to primates (Casale et al., 1988; Cheema et al., 1984; Ralston and Ralston, 1985). Indeed, labeling of cortical projection neurons in mice using *Emx1*^{Cre} (Gorski et al., 2002) revealed that cortical neuron synapses account for ~40% of vGluT1^{+} synapses in the LTMR-RZ which, together with primary somatosensory terminals labeled with *Advillin*^{Cre} mice, accounts for virtually 100% of vGluT1^{+} synapses within this region (Figure 4.1D). Remarkably, cortical projection neuron synapses and LTMR subtype synapses together sharply define the upper region of the LTMR-RZ, with only sparse inputs terminating in laminae I and IIo/i (Figure 4.BA and 4.1E).

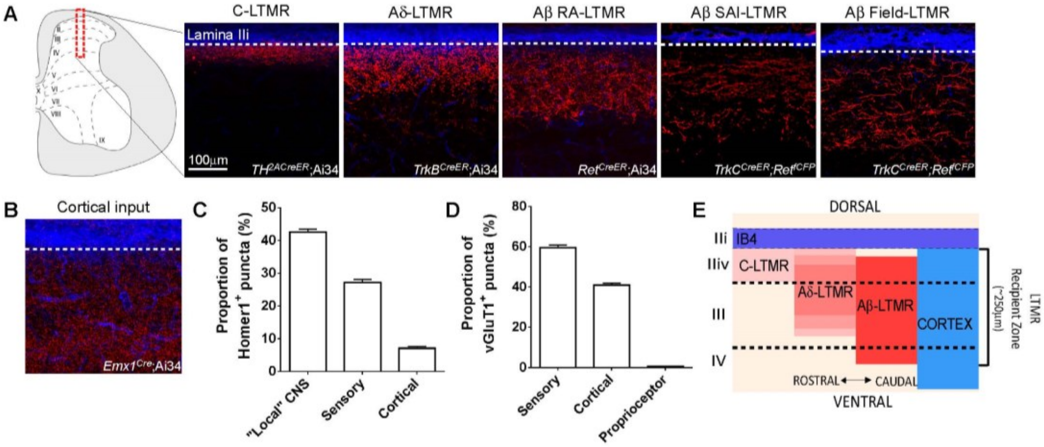

Figure 4.1. The mechanosensory dorsal horn is defined by overlapping LTMR and cortical inputs.
(**A**) Sagittal sections of adult mouse lumbar spinal cord dorsal horn at the level shown in the schematic (left) depicting inputs from all genetically defined classes of LTMRs as well as cortical input. IB4 binding in blue delineates the bottom boundary of Lamina IIiv (white dotted line). C-LTMR inputs labeled with *TH*$^{2A\text{-}CreER}$;*R26*$^{LSL\text{-}synaptophysin\text{-}tdTom}$(Ai34) (0.5 mg tamoxifen treatment at P21); Aδ-LTMRs inputs labeled with *TrkB*^{CreER};Ai34 (2 mg tamoxifen at P21); Aβ RA-LTMRs labeled with *Ret*^{CreER};Ai34 (2 mg tamoxifen at E10.5-11.5); Aβ SAI-LTMRs and Aβ Field-LTMRs labeled with a *TrkC*^{CreER};*Ret*^{fCFP} intersectional strategy (3 mg tamoxifen at E13.5 to label Aβ SAI-LTMRs and 2 mg tamoxifen at P21 to label Aβ Field-LTMRs). (**B**) Sagittal section of adult mouse spinal cord with cortical inputs labeled with *Emx1*^{Cre};Ai34. IB4 binding in blue. (**C**) Quantification of the percentage of Homer1^{+} puncta within the LTMR-RZ opposed to synaptic inputs originating in the spinal cord, dorsal root ganglia, and cortex (n=3 for each input population). Spinal cord inputs are labeled with *Lbx1*^{Cre}, sensory inputs with *Advillin*^{Cre}, and cortical inputs with *Emx1*^{Cre}. All lines are crossed to Ai34 to visualize inputs. *Lbx1*^{Cre} accounts for 94.75±0.96% of all NeuN^{+} cells in the LTMR-RZ (n=3 animals counted), indicating that these inputs are largely emanating from locally-projecting spinal cord interneurons. (**D**) Quantification of the percentage of vGluT1^{+} terminals within the LTMR-RZ that overlap with sensory, cortical, and proprioceptive inputs (n=3 for each input population). Sensory inputs are labeled with *Advillin*^{Cre};Ai34. Cortical inputs are labeled with *Emx1*^{Cre};Ai34. Proprioceptive inputs are labeled with *PV*$^{2A\text{-}CreER}$;*Advillin*^{FlpO};*R26*^{FPSit} (2 mg tamoxifen at P21). (**E**) Schematic summarizing input modalities and anatomical depth of the LTMR-RZ (~250μm below IB4).

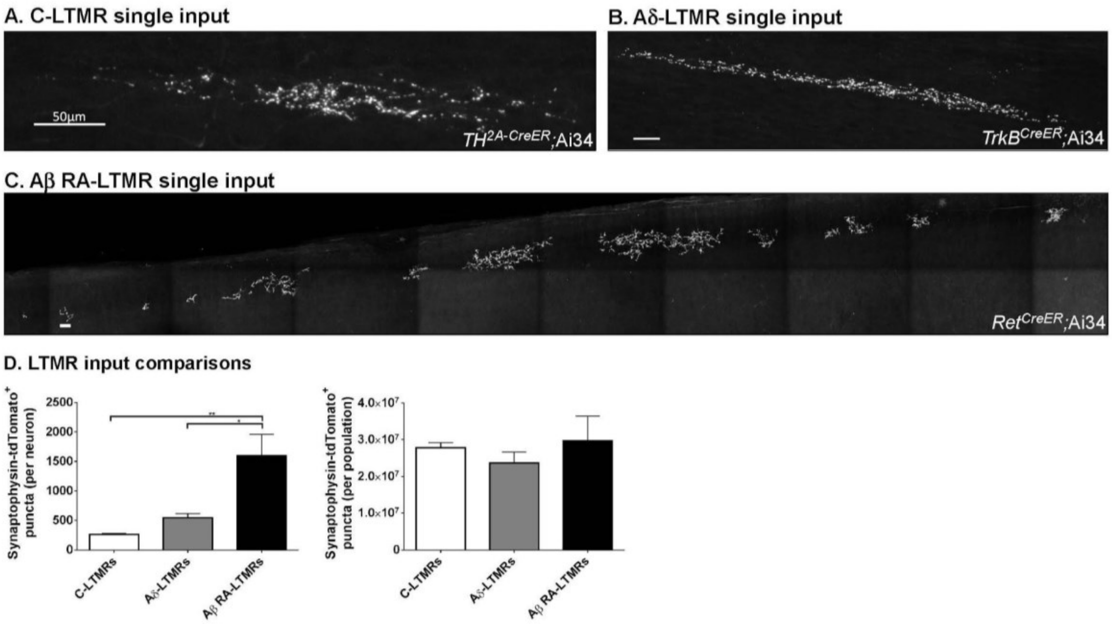

Figure 4.2. LTMR subtypes exhibit different amounts of synaptic inputs at the level of individual neurons but comparable amounts at the level of the population.
(**A**) Whole mount labeling of a single C-LTMR input with $TH^{2A\text{-}CreER}$; $R26^{LSL\text{-}synaptophysin\text{-}tdTomato}$(Ai34) and 0.02mg of tamoxifen at P21. (**B**) Whole mount labeling of a single Aδ-LTMR input with $TrkB^{CreER}$;Ai34 and 0.25mg of tamoxifen at P21. (**C**) Whole mount labeling of a single Aβ RA-LTMR input with Ret^{CreER};Ai34 and 0.02mg of tamoxifen at E10.5. (**D**) LTMR single input comparisons. Top panel shows average number of synapses per neuron (n=4 for each LTMR subtype). Published data citing an average of 10,000 neurons per mouse DRG (Gjerstad et al., 2002a), and relative proportions of DRG neurons that comprise the C-, Aδ-, and Aβ RA-LTMR populations as 15-20%, 7%, and 5%, respectively (Li et al., 2011; Luo et al., 2009; Rutlin et al., 2015) was used to subsequently calculate the approximate number of total synapses from each population (lower panel, see Experimental Procedures). For puncta per neuron: (one-way ANOVA: $P=0.0039$, $F(2,9)=10.96$). Post-hoc Tukey's test: $*p<0.05$, $**p<0.01$.

4.2. LTMR-RZ interneurons form synapses that reside within the LTMR-RZ

We next asked whether the morphologically and physiologically distinct interneuron populations project locally and are likely to form synapses within the LTMR-RZ itself, thereby contributing to LTMR information processing. Also, since inhibitory neurons are likely to make both axodendritic and axoaxonic synapses, we determined which of these types of putative synaptic inputs the four LTMR-RZ inhibitory interneuron subtypes make. For these analyses, the second-generation LTMR-RZ interneuron recombinase tools (CreER and FlpO mouse lines, Table 3.2) were used in conjunction with Cre-dependent synaptophysin-reporter mice to define the anatomical localization and type of LTMR-RZ interneuron synapses. Experiments using a low dose of tamoxifen to achieve sparse labeling revealed that the distribution of synapses emanating from individual interneurons of 8/8 (Cdh3$^+$, CCK$^+$, 5HTr6$^+$, PKCγ$^+$, Knip2$^+$, PVe, PVi, and Rorβ$^+$) interneuron subtypes examined are predominantly restricted to the LTMR-RZ itself (Figure 4.3A-B). In fact, while the number of synapses per neuron for each interneuron subtype is variable (Figure 4.3C), individual interneurons form synapses that are mainly restricted to the lamina in which its cell body resides (Figure 4.3B).

Axodendritic synapses mediate feed-forward excitation and inhibition, whereas axoaxonic contacts between inhibitory spinal cord interneurons and primary afferent terminals provide critical modulation of incoming sensory information through presynaptic inhibition and represent a major component of spinal cord dorsal horn inhibitory circuits (Todd, 1996; Watson et al., 2002). At the light microscope level, putative axoaxonic contacts are distinguished by the close apposition of vGluT1$^+$ and vGAT$^+$ puncta (Figure 4.4C and Hughes et al., 2012). Within the LTMR-RZ, inhibitory axoaxonic contacts are largely restricted to vGlutT1$^+$ *sensory* inputs; descending cortical vGluT1$^+$ inputs are associated with few vGAT$^+$ appositions (Figure 4.4A, 4.5A-B). Thus, as observed for corticospinal projections to the ventral horn (Hanaway and Smith, 1979; Jackson et al., 2006), excitatory glutamatergic projections from the cortex to the LTMR-RZ are largely devoid of axoaxonic contacts (Figure 4.4A, 4.5A-B, and Valtschanoff et al., 1993).

Each sensory neuron vGluT1$^+$ axon terminal within the LTMR-RZ receives on average 2.9 ± 0.1 vGAT$^+$ axoaxonic contacts (Figure 4.5B). PV$^+$ interneurons are known to provide at least some of these inputs within lamina IIiv and III (Hughes et al., 2012). Consistent with this, we found that PVi$^+$ neurons account for half (1.5 ± 0.1) of the vGAT$^+$ contacts within the LTMR-RZ (Figure 4.5D), with a majority (72.2%) of vGluT1$^+$ terminals in this region receiving PV$^+$ vGAT$^+$ contacts (Figure 4.5C). To identify the remaining vGAT$^+$ axoaxonic contacts, immunostaining and light microscopy analysis was done using inhibitory neuron subtype GFP and CreER tools (Tables 3.1 and 3.2, Figure 4.4B). This analysis showed that Cdh3$^+$ inhibitory interneurons also form vGAT$^+$ axoaxonic contacts within the LTMR-RZ, averaging 0.9 ± 0.1 contacts per vGluT1$^+$ terminal and contacting 52.5% of vGluT1$^+$ terminals (Figure 4.5C-D). In contrast, Rorβ$^+$ and Kcnip2$^+$ inhibitory interneurons form few, if any, axoaxonic contacts in the LTMR-RZ (Figure 4.4D, 4.5C-D). As previously noted, PVi$^+$ and Cdh3$^+$ interneuron populations label an intersecting population (Figure 3.6B), and PV/Cdh3 double positive cells also form axoaxonic contacts in the LTMR-RZ (Figure 4.5C-D). We also observed that virtually all Cdh3$^+$, Kcnip$^+$, Rorβ$^+$ and PVi terminals are associated with at least 1 gephyrin punctum (Figure 4.4E, 4.5E), which are most prevalent in axodendritic and axosomatic inhibitory synapses and absent at axo-axonic synapses on primary afferents (Mitchell et al., 1993; Todd et al., 1996; Lorenzo et al.,2014). Thus, all genetically labeled LTMR-RZ inhibitory interneurons are likely to make axodendritic synapses to promote feedforward inhibition within the LTMR-RZ, while a subset (PV^+, $Cdh3^+$, and to a lesser extent $Ror\beta^+$) are also likely to mediate presynaptic inhibition via axoaxonic synapses.

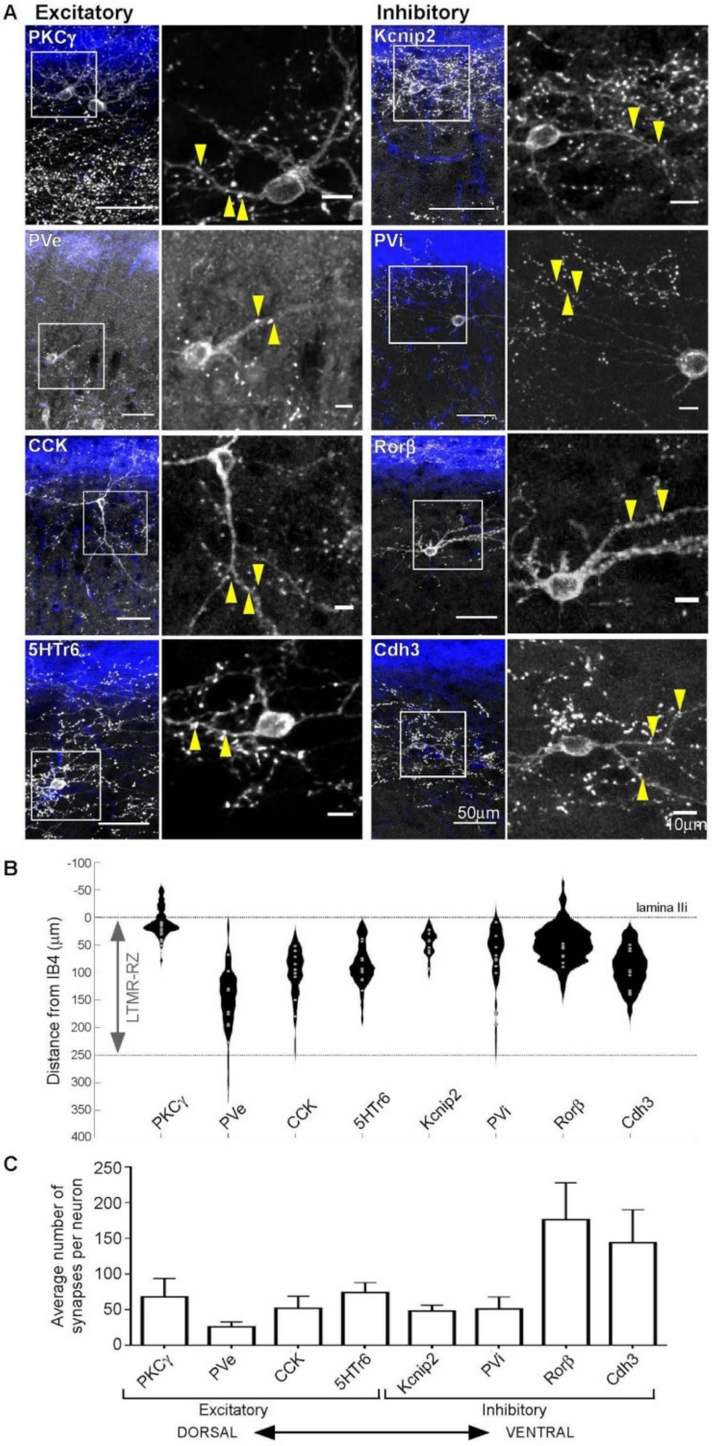

Figure 4.3. LTMR-RZ interneurons make synapses largely within the LTMR-RZ. (**A**) IHC images of adult (P30-P35) lumbar sagittal sections (50µm) spinal cord dorsal horn (SC DH) showing synaptophysin-tdTomato (Ai34) or synaptophysin-GFP (*R26*^{FPSit}) expression driven by recombinase mouse lines to target PKCγ$^+$ (*PKCγ*^{CreER}*;* Ai34), PVe(*PV*^{FlpO}*;Lbx1*^{Cre}*; R26*^{FPSit}), CCK$^+$(*CCK*^{CreER}*;* Ai34), 5HTr6$^+$(5HTr6- CreER*;*Ai34), Kcnip2$^+$ (Kcnip2-CreER*;*Ai34), PVi$^+$ (*PV*^{FlpO}*;vGAT*^{Cre}*;R26*^{FPSit}), Rorβ$^+$ (*Rorβ*^{CreER}*;*Ai34), and Cdh3$^+$ (Cdh3-CreER*;*Ai34) interneuron subtypes. Mice were treated with 0.5-2mg tamoxifen at P21. IB4 (blue) labels lamina IIiv border in large-scale view (left panels), with inset magnified in right panels. Arrowheads indicate synaptophysin-tdTomato$^+$ puncta from individual interneurons. (**B**) Violin plots depicting quantification of synaptic number and location by interneuron subtype, as determined by synaptophysin-reporter expression (n=3 animals; 10 neurons total for each interneuron subtype) relative to LTMR-RZ. Black plots indicate presence of synapses at specific dorsal-ventral locations (distance from IB4, y-axis) and the relative number of synapses at those levels (depicted by plot width) for the 10 cells of each interneuron type (soma location plotted with grey circles). (**C**) Average number of synapses per neuron for 8/11 LTMR-RZ interneuron populations (n=3 per population).

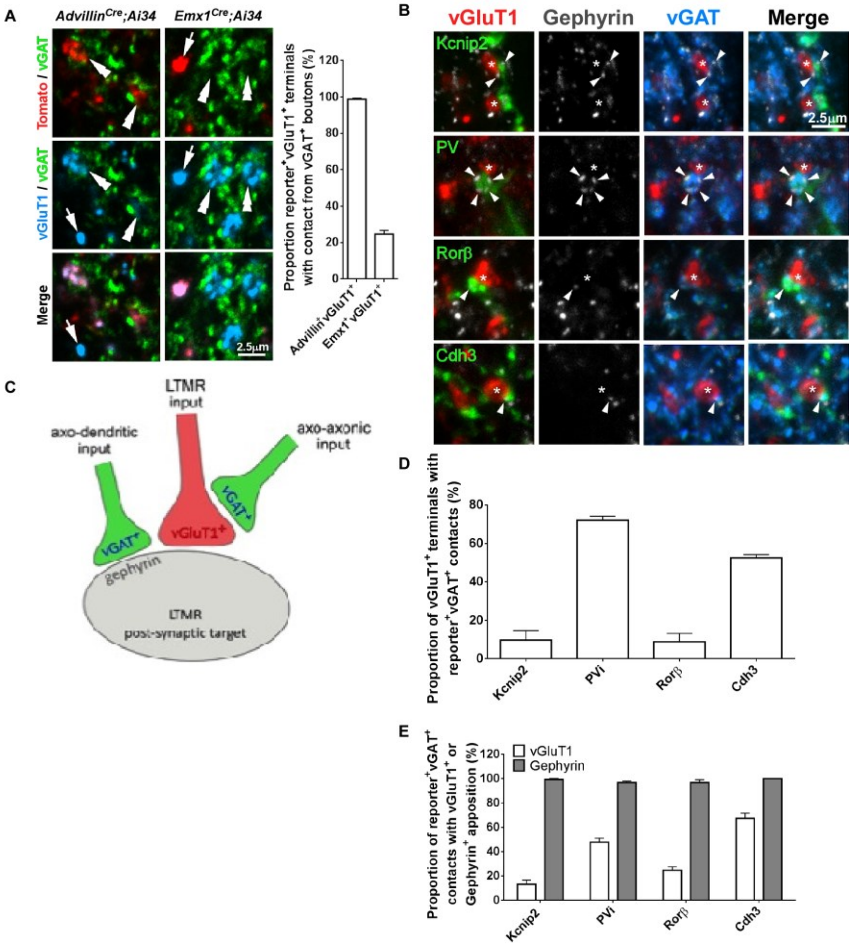

Figure 4.4. LTMR-RZ interneurons contribute to both pre- and post-synaptic inhibition in this region.

(**A**) IHC images of transverse sections (60μm) of SC DH showing synaptophysin-tdTomato (Ai34) expression driven by *Advillin*^{Cre} or *Emx1*^{Cre} to label sensory and cortical inputs to the LTMR-RZ, respectively. Co-labeling with vGAT and vGluT1 is used to determine axo-axonic contacts onto these terminals which were quantified across the LTMR-RZ (n=4 for each reporter line, see Experimental Procedures). Double arrowheads and arrows indicate vGluT1$^+$ terminals with and without vGAT$^+$ contacts, respectively. Quantification shown in graph to right. (**B**) IHC images of transverse sections (60μm) of SC DH showing labeling of PV$^+$ (immunostaining), Cdh3$^+$ (Cdh3-GFP), Rorβ$^+$ (*Rorβ*^{CreER}*;*Ai34), and Kcnip2$^+$ (Kcnip2-CreER*;*Ai34) inhibitory neuron subtype terminals (green). Co-labeling with vGAT (blue), vGluT1 (red, asterisks), and gephyrin (white, arrowheads) is used to determine axo-axonic and axo-dendritic contacts made by these boutons. (**C**) Schematic of axo-dendritic and axo-axonic putative connections. (**D**) Quantification of vGluT1$^+$ (n=4) apposition to interneuron-reporter$^+$vGAT$^+$ boutons: relative proportion of all vGluT1$^+$ boutons in LTMR-RZ receiving axo-axonic contacts from each inhibitory interneuron population. (**E**) Quantification of vGluT1$^+$ (n=4) and gephyrin$^+$ (n=3) apposition to interneuron-reporter$^+$vGAT$^+$ boutons, representing axoaxonic and axodendritic contacts, respectively. Relative proportion of vGAT$^+$ boutons from each inhibitory interneuron population in contact with vGlut1$^+$ terminals or gephyrin$^+$ puncta.

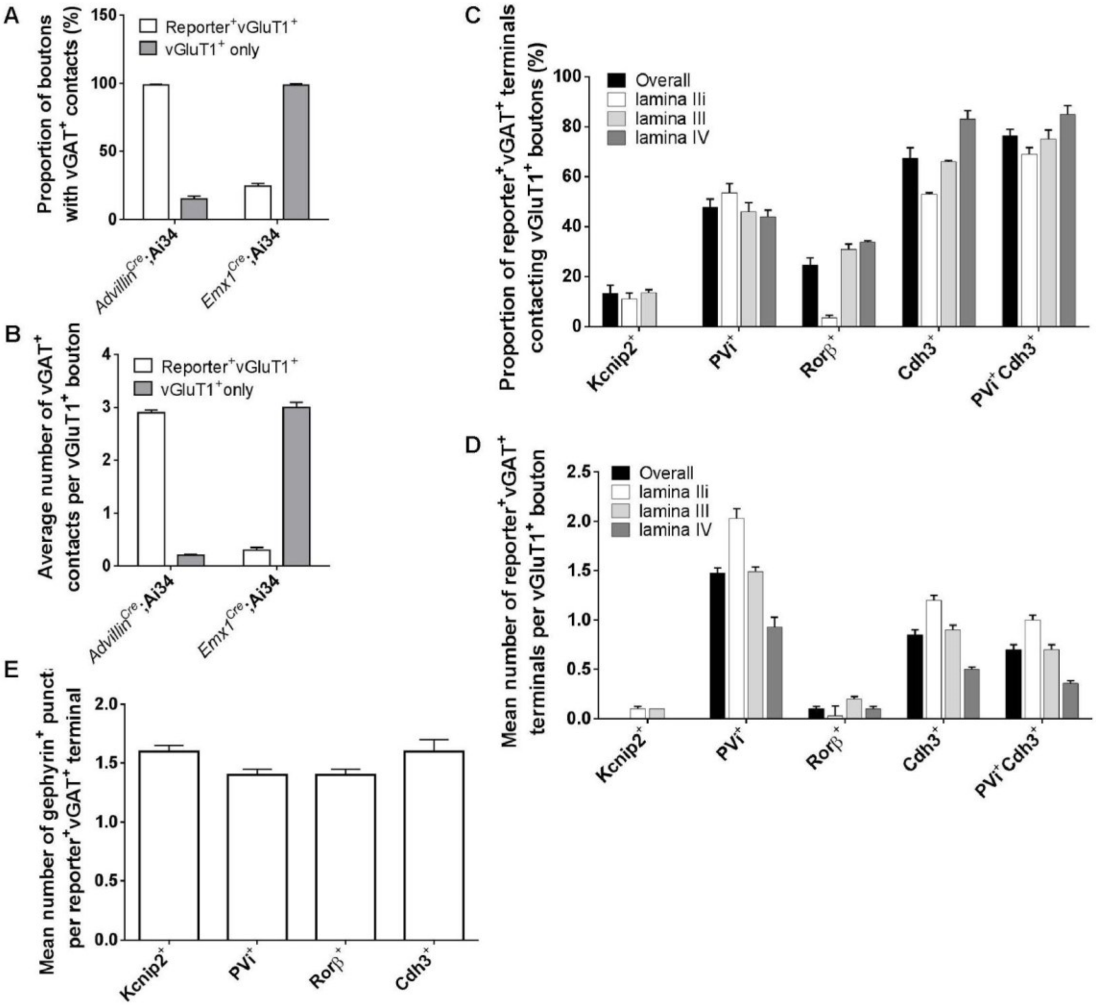

Figure 4.5. Additional quantifications of contributions to pre- and post-synaptic inhibition by LTMR-RZ interneurons.
(**A**) Proportion of Tomato$^+$vGluT1$^+$ and vGluT1$^+$ only terminals receiving vGAT$^+$ contacts in *Advillin^{Cre};R26$^{LSL\text{-}synaptophysin\text{-}tdTomato}$*(Ai34) and *Emx1^{Cre};*Ai34 animals (n=4 for each population). (**B**) Average number of vGAT$^+$ contacts to Tomato$^+$vGluT1$^+$ and vGluT1$^+$ only terminals in *Advillin^{Cre};*Ai34 and *Emx1^{Cre};*Ai34 animals (n=4 for each population). (**C**) Proportion of Reporter$^+$vGAT$^+$ contacts to vGluT1$^+$ boutons as a function of LTMR-RZ lamina (n=4 for each population). (**D**) Average number of Reporter$^+$vGAT$^+$ contacts to individual vGluT1$^+$ boutons as a function of LTMR-RZ lamina (n=4 for each population). (**E**) Average number of gephyrin$^+$ puncta per Reporter$^+$vGAT$^+$ bouton (n=3 for each population).

4.3. Each LTMR-RZ interneuron subtype receives input from LTMRs, cortex, and other CNS sources

The remarkable degree of interneuron subtype diversity in the LTMR-RZ raises intriguing questions about allotment of function. Do individual LTMR-RZ interneuron subtypes function as dedicated recipients of particular sensory modalities, or do some LTMR-RZ interneuron subtypes receive inputs from select LTMRs while others receive descending inputs from corticospinal neurons? The availability of genetic tools that label 11 LTMR-RZ interneuron subtypes, in conjunction with LTMR and forebrain neuron genetic labeling strategies and synaptic markers, enabled us to define basic principles of LTMR-RZ excitatory synaptic organization (Figure 4.6A). Excitatory synapses were identified using Homer1 antibody overlap with each of the 11 genetically labeled interneurons (Gutierrez-Macinas et al., 2016). Synapses were defined as originating from an input population of interest when the pre-synaptic marker of that population partially or fully overlapped with a Homer1$^+$ punctum (Figure 4.6B). Histologically defined synaptic contacts were validated by array tomography analysis that assessed the overlap between primary sensory synaptic boutons and a range of synaptic markers (Figure 4.7). This approach enabled a high-throughput, quantitative analysis of LTMR subtype and cortical neuron synaptic contacts made onto each of the 11 LTMR-RZ interneuron subtypes.

We first compared the amount and distribution of excitatory inputs onto each of the 11 LTMR-RZ interneuron populations. Interestingly, each interneuron subtype receives approximately the same density of excitatory synaptic contacts, defined by Homer1$^+$ puncta: cell bodies have 0.119 ± 0.003 Homer1$^+$ puncta/μm^2 (measured as a function of surface area), while proximal and distal dendrites have considerably more synapses, exhibiting 0.836 ± 0.020 and 0.787 ± 0.018 puncta/μm, respectively. This compares favorably to the number of excitatory synaptic contacts onto PSDC output (projection) neurons, which exhibit fewer excitatory inputs on cell bodies (0.062 ± 0.004 Homer1$^+$ puncta/μm^2) but comparable levels on proximal and distal dendrites (0.895 ± 0.060 and 0.743 ± 0.067 puncta/μm, respectively). We next assessed the number of LTMR, cortical projection neuron, and other "non-cortical" CNS inputs onto each of the 11 genetically labeled LTMR-RZ interneuron subtypes. This analysis revealed that the relative proportions of excitatory inputs onto each of the 11 interneuron subtypes are comparable and range from 30-55% sensory neuron inputs, 13-18% cortical projection neuron inputs, and 30-55% non-cortical CNS inputs (Figure 4.8A). The non-cortical CNS inputs are likely predominantly vGluT2$^+$ input from locally-projecting interneurons, as Homer1$^+$ in the LTMR-RZ is largely accounted for by sensory, cortical, and local interneuron inputs (Figure 4.1). Thus, each of the 11 interneuron subtypes is likely to receive the majority of its excitatory input from local CNS neurons and/or primary somatosensory neurons, and a lesser, but substantial, number of synaptic inputs from corticospinal projection neurons. For all interneuron subtypes, this convergence of PNS and CNS synaptic inputs occurs at the level of individual neurons, not just for interneuron populations as a whole. Indeed, individual neurons of each subtype receive inputs from both corticospinal neurons (*Emx1^{Cre};*Ai34) and Aβ-LTMRs or Aδ-LTMRs (defined as vGluT1$^+$ puncta that do not co-localize with *Emx1^{Cre};*Ai34), often in close proximity on the same dendrite (Figure 4.8B-C). We conclude that each of the 11 LTMR-RZ interneuron subtypes receives convergent inputs originating from LTMRs, cortex, and local spinal cord interneurons.

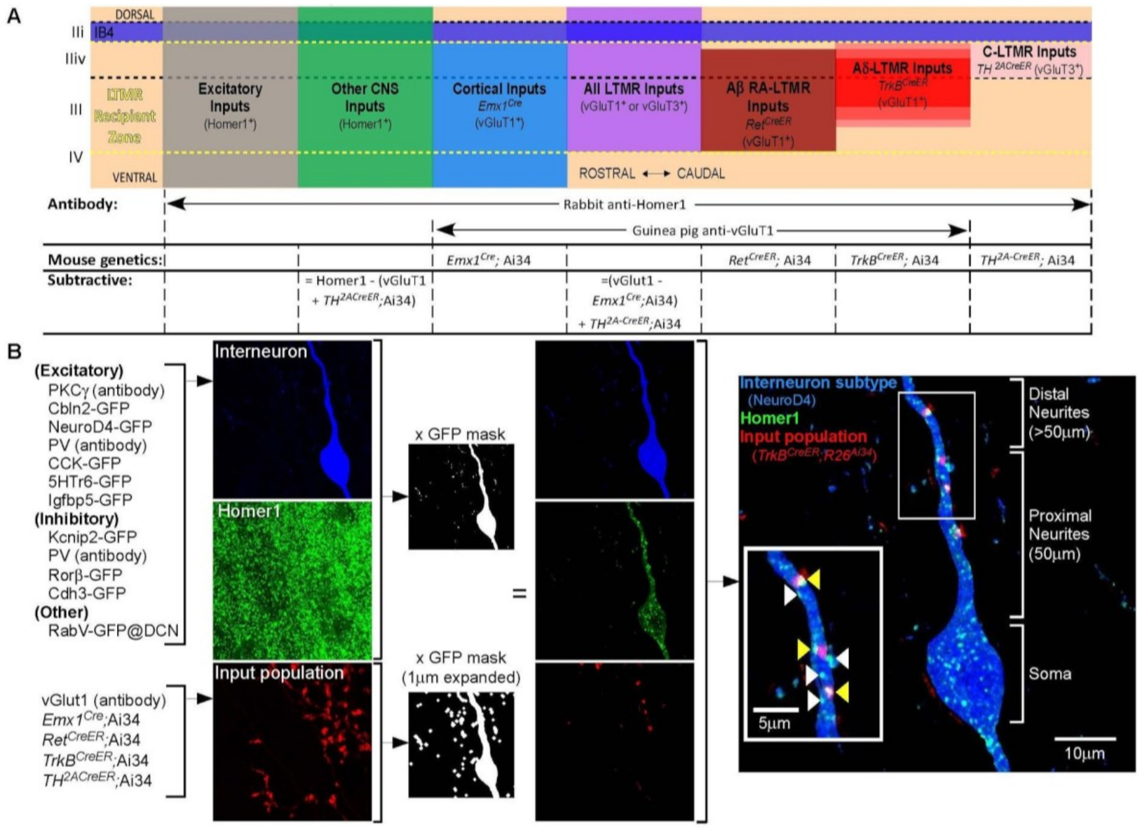

Figure 4.6. Tools and approach for labeling quantifying anatomically-defined synapses for input analysis.
(**A**) Overview of genetic tools, antibodies, and subtractive methods used to identify and dissect the relative contributions of various input populations to each interneuron population's excitatory connectome. Schematic shows relative location of these input populations to the SC DH (sagittal view). Tamoxifen regimens for labeling input populations were as follows: 0.4mg at P21 for *TH*$^{2A\text{-}CreER}$;*R26*$^{LSL\text{-}synaptophysin\text{-}tdTomato}$(Ai34), 2mg at P21 for *TrkB*^{CreER};Ai34, and 2.5mg at E10.5-11.5 for *Ret*^{CreER};Ai34. All animals used in this analysis were collected at P30-P40 and lumbar SC was used for analysis. (**B**) Outline of methods used for quantifying anatomically-defined synapses. IHC images were collected and the interneuron channel was used to generate two masks (one containing only interneuron label and the other containing this same region expanded in all directions by 1µm) that could then be used to isolate only post-synaptic labeling within the interneuron mask and pre-synaptic labeling within the expanded mask. When recombined, counts of inputs with (yellow arrows) and without (white arrows) contacts from the input population of interest were quantified according to cellular compartment (soma, proximal neurite, distal neurite). See Experimental Procedures.

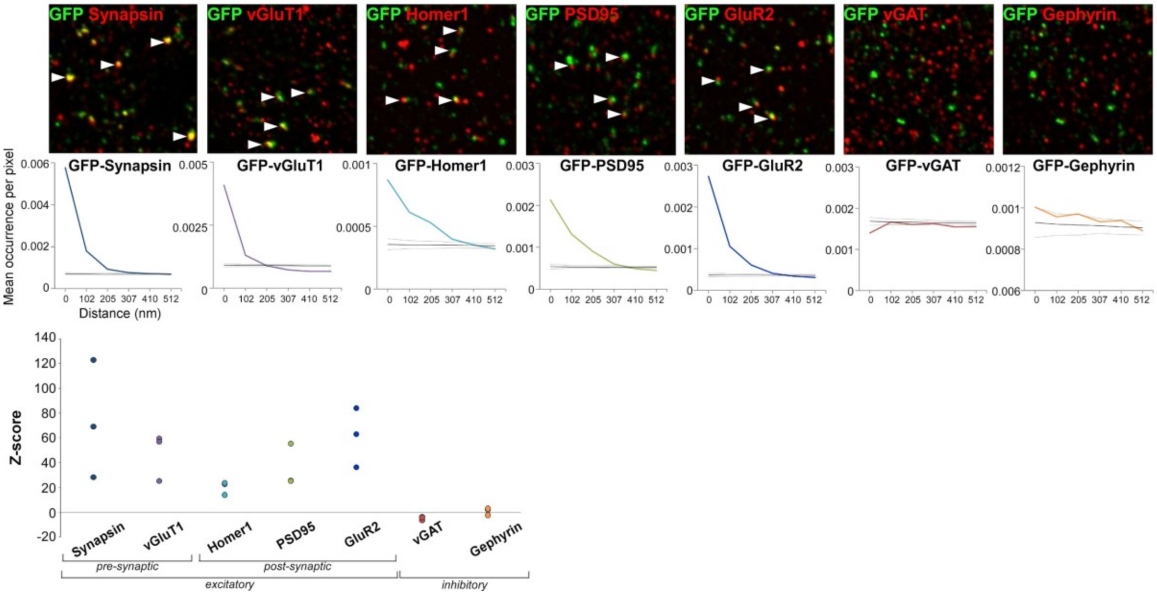

Figure 4.7. Array tomography analysis and validation with known synaptic markers.

Co-localization analysis of genetically labelled sensory presynaptic axon terminals ($Advillin^{FlpO};R26^{FSit}$) using array tomography. Single planes of IHC labelling show association of synaptic markers with GFP$^+$ terminals (arrows). Quantifications show mean occurrence of GFP-immunolabeling co-localization per pixel as a function of distance from the center of GFP$^+$ boutons. Colored lines represent real data; black and grey lines represent the mean +/- standard deviation of randomized data. *Z* scores for mean marker densities within GFP$^+$ terminals for real (n=3 animals) versus randomized data (n=4 stacks) indicate higher densities in the real data.

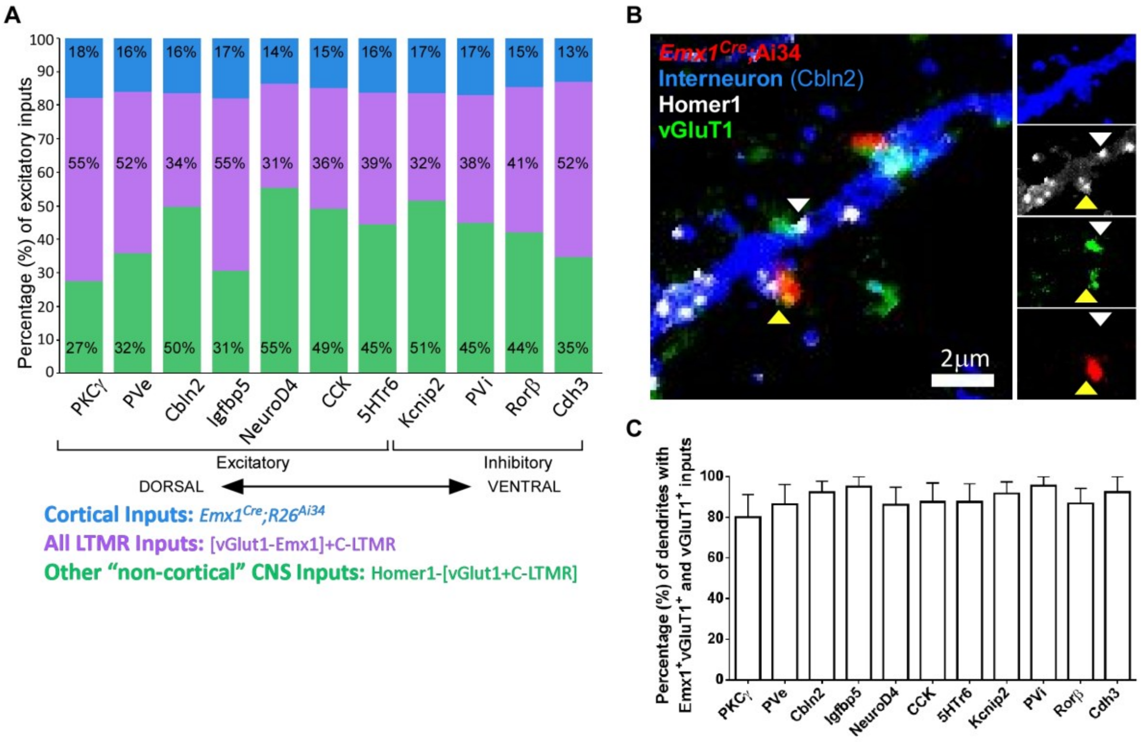

Figure 4.8. All LTMR-RZ interneuron subtypes receive inputs from the periphery, cortex, and other CNS regions.
(**A**) Compiled quantifications of excitatory inputs from cortex (blue), all LTMRs (purple), and non-cortical CNS (green) onto the 11 interneuron populations (n=3 for each interneuron and input population combination). Quantifications shown are for proximal+distal neurites, as somatic inputs were minimal to all subtypes and no significant difference as a function of proximal versus distal was observed in overall excitatory input (as measured by Homer1$^+$) or broad input quantifications. (**B**) IHC image illustrating convergent inputs onto a single dendrite of an interneuron in the LTMR-RZ. Both cortical (Ai34$^+$ vGluT1$^+$, yellow arrowhead) and sensory (Ai34$^-$ vGluT1$^+$, white arrowhead) inputs were verified by Homer1$^+$ apposition. (**C**) Quantification shows the relative proportion of dendrites that receive such convergent inputs for all 11 interneuron populations (n=3 for each interneuron population).

4.4. LTMR-RZ interneuron subtypes receive unique patterns of convergent LTMR inputs

LTMR-RZ interneuron subtypes exhibit remarkably comparable proportions of excitatory inputs from primary somatosensory neurons, corticospinal neurons, and local CNS neurons (Figure 4.8A). On the other hand, spinal cord slice electrophysiology experiments using ChR2-assisted circuit mapping demonstrated different levels of synaptic drive from one LTMR subtype, the Aβ RA-LTMR, onto Cbln2$^+$, Kcnip2$^+$ and Rorβ$^+$ interneurons (data not shown). Thus, we hypothesized that the number of synaptic contacts derived from select LTMR subtypes is a distinguishing feature of LTMR-RZ interneuron subtypes. To address this possibility, and to map the patterns of LTMR subtype synapses onto each of the 11 LTMR-RZ interneuron subtypes, a high-throughput histological approach was used to construct an LTMR subtype-specific connectivity atlas of the LTMR-RZ.

To generate the LTMR subtype-specific connectivity map of the LTMR-RZ, we quantified the number of synaptic contacts between three physiologically distinct LTMR subtypes using LTMR-CreER tools and a Cre-dependent synaptophysin-tdTomato (Ai34) reporter mouse, and the 11 LTMR-RZ interneuron subtypes using compatible fluorescent reporters (Figure 4.6B). This analysis revealed that LTMR-RZ interneurons display unique "LTMR synaptic connectivity profiles" (Figure 4.9A). The relative number of synaptic contacts derived from each of the three individual LTMR subtypes is usually small and comparable to that observed for cortical inputs, on the order of 10-20% of total excitatory inputs; however, larger variations in the number of input proportions were observed, ranging from 0% to 30%. Interestingly, the majority of interneuron subtypes receive input from two or more LTMR subtypes. Moreover, as observed for cortical neuron and pan-sensory neuron inputs, the convergence of multiple LTMR subtypes onto interneuron subtypes is also evident at the level of individual neurons. Indeed, experiments using *TrkB*^{CreER}*;*Ai34 to label Aδ-LTMR inputs and vGluT1 staining to label other myelinated somatosensory and descending cortical inputs (vGluT1^{+} puncta that do not co-localize with *TrkB*^{CreER}*;* Ai34*)* showed convergence of these inputs (Figure 4.9B-C). Thus, each of the 11 LTMR-RZ interneuron subtypes samples converging synaptic inputs from two or more physiologically distinct LTMR subtypes as well as local interneurons and corticospinal neurons.

The relative proportion of LTMR subtype synapses distributed across each of the 11 interneuron subtypes was next calculated to identify post-synaptic partner preferences for the different LTMRs (Figure 4.10). This analysis indicated that C-LTMRs and, to a lesser extent, Aβ RA-LTMRs exhibit postsynaptic partner selectivity, forming the majority of their synapses onto a subset of the 11 LTMR-RZ interneuron types. C-LTMRs form synapses onto 4/11 interneuron subtypes, and three of those (PKCγ^{+}, PVe^{+}, and Rorβ^{+}) receive 80% of all C-LTMR synaptic contacts. Aβ RA-LTMR form synapses onto 9/11 interneuron subtypes, with five subtypes (PVe^{+}, Igfbp5^{+}, PVi^{+}, Rorβ^{+}, and Cdh3^{+}) receiving nearly 70% of Aβ RA-LTMR inputs. Importantly, these patterns of synaptic input specificity are not simply a reflection of anatomical organization or the location of LTMR subtype endings and interneuron populations. For example, both Kcnip2^{+} and Cbln2^{+} interneurons reside within the C-LTMR termination zone (Figure 3.5), but neither receives an appreciable number of C-LTMR synaptic contacts. In stark contrast to the C-LTMR and Aβ RA-LTMR subtype synaptic partner profiles, Aδ-LTMRs have no preferred interneuron partners, and instead divide their synaptic inputs equally across the 11 interneuron subtypes (~9% each). This remarkably broad Aδ-LTMR synaptic distribution pattern is similar to that of descending cortical inputs. Thus, the majority of LTMR-RZ interneurons receive input from at least two LTMR subtypes, and physiologically distinct LTMR subtypes exhibit a divergence of synaptic contacts onto at least 4 and as many as 11 LTMR-RZ interneuron subtypes.

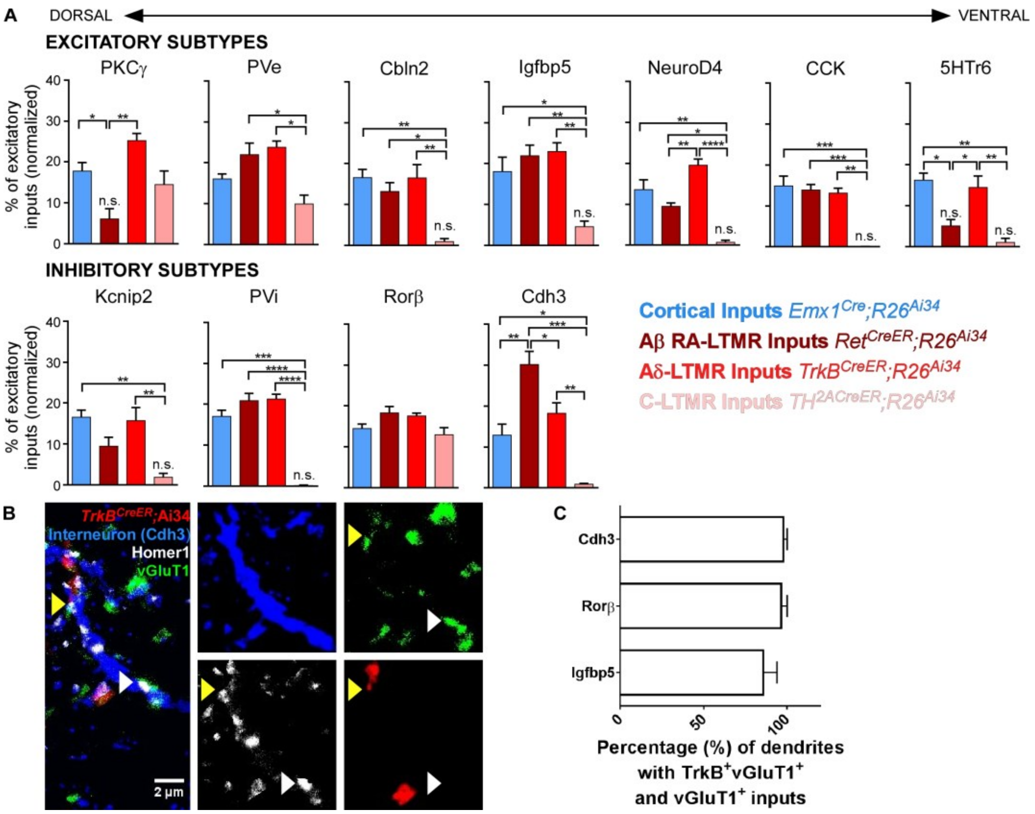

Figure 4.9. LTMR-RZ interneuron subtypes display unique patterns of convergent tactile synaptic inputs.

(**A**) Compiled quantifications of excitatory inputs from, left to right, cortex (blue), Aβ RA-LTMRs (dark red), Aδ-LTMRs (red) and C-LTMRs (light red) onto each of the 11 interneuron populations (onto proximal+distal neurites). Values are normalized percent of excitatory input as measured by Homer1$^+$ puncta (n=3 for each interneuron and input population combination. See Experimental Procedures). To determine if inputs are truly above 0, a one-sample t-test was used. If input values were not statistically significantly (p>0.05) above 0%, lack of significance was indicated by "n.s." above the respective bar graph. For comparisons between input lines onto individual interneuron populations, statistics are denoted above bars by brackets. For PKCγ: (one-way ANOVA: P = 0.0042, F[3,8] = 10.19). For Cbln2: (one-way ANOVA: P = 0.0031, F[3,8] = 11.16). For NeuroD4: (one-way ANOVA: P = 0.0001, F[3,8] = 27.46). For PVe: (one-way ANOVA: P = 0.0110, F[3,7] = 8.143). For CCK: (one-way ANOVA: P = 0.0003, F[3,8] = 21.63). For 5HTr6: (one-way ANOVA: P = 0.0012, F[3,8] = 15.08). For Igfbp5: (one-way ANOVA: P = 0.0031, F[3,8] = 11.23). For Kcnip2: (one-way ANOVA: P = 0.0046, F[3,8] = 9.874). For PVi: (one-way ANOVA: P < 0.001, F[3,7] = 55.47). For Rorβ: (one-way ANOVA: P = 0.0.678, F[3,8] = 3.540). For Cdh3: (one-way ANOVA: P = 0.0002, F[3,8] = 24.45). Post-hoc Tukey's test: *p<0.05, **p<0.01, ***p<0.0005, ****p<0.0001. (**B**) IHC image illustrating convergent inputs onto a single dendrite of an interneuron in the LTMR-RZ. Both Aδ-LTMRs (Ai34$^+$vGluT1$^+$) and other sensory or cortical (Ai34$^-$ vGluT1$^+$) inputs were verified by Homer1$^+$ apposition. (**C**) Quantification shows the relative proportion of dendrites that receive convergent LTMR inputs for three interneuron populations (n=3 for each interneuron population).

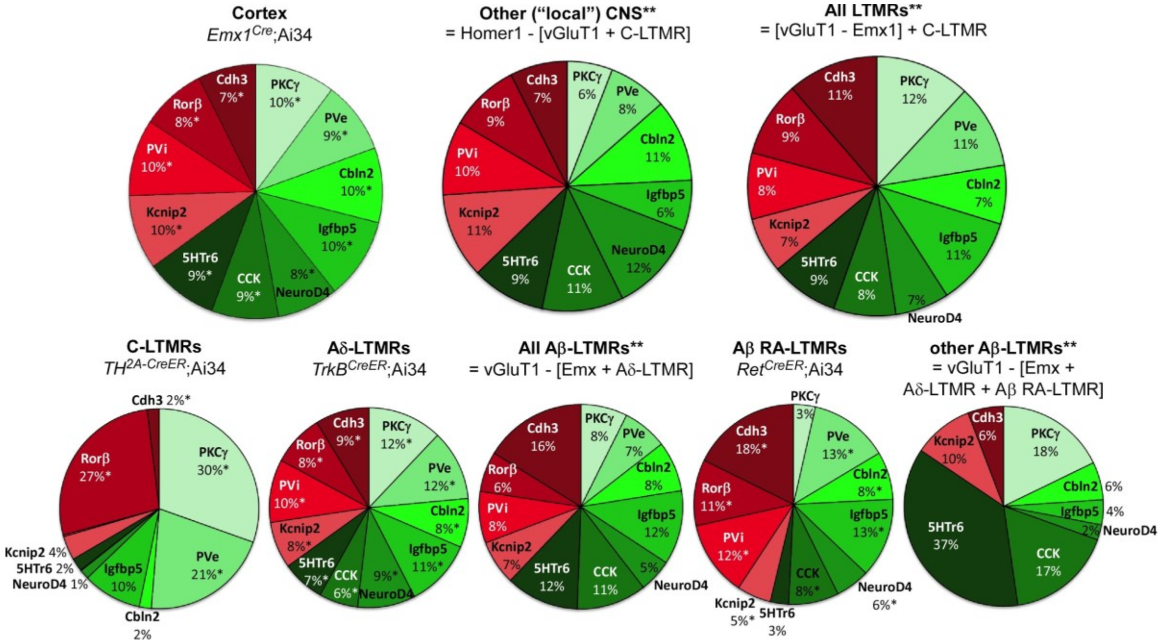

Figure 4.10. Interneuron preference of input populations.
Compiled quantification of LTMR inputs onto the 11 interneuron populations, demonstrating how broad input populations and distinct LTMR subtypes allocate their anatomically-defined synapses onto the 11 identified interneuron populations of the LTMR-RZ. (n = 3 for each interneuron and input population combination). In each pie graph, interneuron populations are color coordinated as excitatory (green) or inhibitory (red) and are listed in order (clockwise) of dorsal to ventral location within the excitatory/inhibitory category. Contributions from LTMR input populations that were found to be greater than 0% of an interneuron population's excitatory input (using a one-sample t-test) are denoted with asterisks: *$p<0.05$. Note that a subset of these quantifications are calculated via subtractive means (denoted by **, see Experimental Procedures), and therefore cannot be analyzed for statistical significance.

4.5. LTMR-RZ interneurons modulate output pathways that convey tactile information to the brain

A key to understanding the nature of tactile processing that occurs in the LTMR-RZ is defining the activity of output neurons that carry tactile information to higher regions such as the DCN. The postsynaptic, ascending cutaneous touch pathways that reside in the dorsal horn are the post-synaptic dorsal column (PSDC) pathway, the spinocervical tract (SCT) and, possibly, subdivisions of the anterolateral tract (ALT) (Morin, 1955; Rustioni and Kaufman, 1977; Todd, 2010). There exists relatively little evidence for the presence of the SCT pathway in mice (Giesler et al., 1987), and retrograde labeling of PSDC and ALT showed that PSDC neurons are the predominant output neurons located within the LTMR-RZ (Figure 3.1A, data not shown). Thus, we next compared the synaptic connectivity profile of PSDC neurons with those of the 11 LTMR-RZ interneuron subtypes. In contrast to each of the 11 LTMR-RZ interneuron subtypes, PSDC projection neurons receive synaptic inputs largely from local spinal cord interneurons (60%), considerably fewer from sensory neurons (34%), and very few from cortical projection neurons (6%) (Figure 4.11A). In addition, PSDC neurons receive more restricted types of LTMR synaptic inputs, receiving no contacts from C-LTMRs and fewer synaptic contacts from Aδ-LTMRs than any of the 11 interneuron subtypes (Figure 4.11B). Thus, in contrast to the 11 LTMR-RZ interneuron subtypes, PSDC neurons receive excitatory synaptic inputs mainly from local LTMR-RZ interneurons and, to a lesser extent, Aβ-LTMRs (Maxwell et al., 1985, 1995).

The relatively low number of direct LTMR and cortical inputs and high number of local excitatory inputs onto PSDC neurons suggests a model in which LTMR-RZ interneuron subtypes receive unique combinations of LTMR and cortical inputs and, in turn, connect to PSDC neurons to modulate their output activities. Indeed, preliminary *ex vivo* recordings of mouse PSDC neurons indicate that they exhibit complex tuning and receptive field properties that are highly distinct from any individual LTMR subtype (data not shown). Therefore, we next asked whether PSDC output responses are shaped by a combination of monosynaptic inputs from Aβ-LTMRs and indirect (polysynaptic) inputs, driven by Aβ-LTMRs, Aδ-LTMRs, and C-LTMRs and conveyed to PSDCs via LTMR-RZ interneurons. Indeed, whole cell patch clamp recordings of retrogradely-labeled PSDC neurons and electrical stimulation of dorsal roots using a stimulus intensity that selectively activates Aβ fibers revealed the presence of both mono- and poly-synaptic inputs onto PSDCs (Figure 4.11C-D). Recordings carried out with holding potentials at -70mV and 0mV and pharmacological dissection of input properties indicated that the polysynaptic inputs onto PSDCs are both excitatory and inhibitory in nature (Figure 4.11D,F). When the electrical stimulation intensity was increased to activate both Aβ- and Aδ-fibers, we observed an alteration in the polysynaptic waveforms, indicating that inputs from Aδ-fibers are conveyed via LTMR-RZ interneuron polysynaptic connections to PSDCs (data not shown). In complementary experiments, we targeted PSDC neurons in spinal cord slices from *TrkB*^{CreER}*;*Ai32 mice, expressing ChR2 exclusively in Aδ-LTMRs. Concomitant electrical stimulation of Aβ fibers with optical stimulation of Aδ-LTMR terminals revealed convergent inhibitory polysynaptic inputs from Aβ fibers and Aδ-LTMRs onto PSDCs (Figure 4.11D-E). This stimulation paradigm further demonstrated polysynaptic connections that convey tactile information from LTMRs to PSDCs through LTMR-RZ interneurons. Taken together, these findings suggest that

PSDC neurons receive not only monosynaptic and polysynaptic excitatory drive from Aβ fibers, but also polysynaptic inhibitory inputs from Aβ and Aδ-LTMRs. Thus, a major output population of the LTMR-RZ, PSDC neurons, receive both direct, monosynaptic Aβ-LTMR synaptic inputs and indirect excitatory and inhibitory inputs via LTMR-RZ interneurons, which are themselves driven by multiple LTMR subtypes, LTMR-RZ interneurons and, potentially, cortical projection neurons.

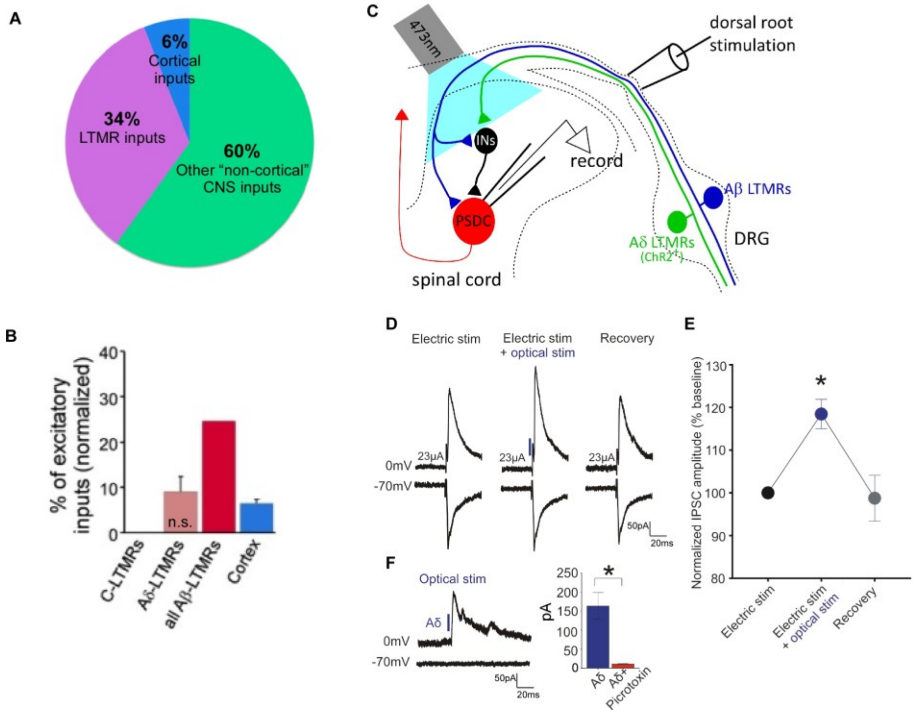

Figure 4.11. LTMR-RZ interneuron subtypes contribute to a dorsal horn output population, the post-synaptic dorsal column (PSDC) neurons.
(**A**) Compiled quantifications of excitatory inputs from cortex (blue), all LTMRs (purple), and non-cortical CNS (green) onto PSDC neurons. (**B**) Compiled quantifications of excitatory inputs from C-LTMRs, Aδ-LTMRs, all Aβ-LTMRs and cortex onto PSDC neurons. (onto proximal+distal neurites). Values are normalized percent of excitatory input as measured by Homer1$^+$ puncta (n=3 for each interneuron and input population combination. See Experimental Procedures), except for "all Aβ-LTMR inputs" which are determined via subtraction (= vGluT1 – [cortex + Aδ-LTMRs]). To determine if inputs are truly above 0, a one-sample t-test was used. If input values were not statistically significantly ($p>0.05$) above 0%, lack of significance was indicated by "n.s." above the respective bar graph. (**C**) Schematic showing conditions for synaptic physiology, with PSDC whole-cell voltage-clamp recordings, dorsal root stimulation and optogenetic stimulation using whole-field illumination. (**D**) Average of twelve consecutive traces showing Aβ-evoked synaptic responses with electrical stimulation of dorsal roots (23 uA) taken just before (left panel), during (middle panel) and after (right panel) optogenetic activation of Aδ-LTMR terminals (blue rectangle). At V_h= 0mV, optical stimulation of Aδ-LTMRs increases the amplitude of the feedforward polysynaptic Aβ-evoked IPSCs (n=4/4 cells). At V_h= -70mV, the electrical evoked EPSC does not change with concomitant optical stimulation (5ms pulses during electrical stimulation; blue rectangle; n=9 PSDC neurons). (**E**) Normalized mean IPSC amplitude ± SEM; *$p < 0.05$ (paired t-test). (**F**) Left: Optical stimulation (blue rectangle) of Aδ-LTMRs evokes polysynaptic IPSCs onto PSDC neurons. Right: Mean optical IPSC in the absence and presence of the GABA$_A$R receptor antagonist picrotoxin (100 μM). *$p < 0.05$ (paired t test).

CHAPTER 5: DISCUSSION

These studies reveal the complex anatomical organization of LTMR peripheral and central projections, as well as the profound cellular diversity and integrative synaptic architecture of the deep dorsal horn, where LTMRs synapse and contribute to neural circuits involved in processing innocuous touch information. We found that peripheral axonal projections from LTMRs are largely organized to comprehensively cover the mammalian skin with minimal overlap within a single subtype. This ‘tiled’ pattern was observed to vary by body region or hair follicle type for Aβ-LTMRs. Aβ SAI-LTMRs show more overlap in abdominal hair innervation than other body regions, while Aβ Field- and Aβ RA-LTMRs show no such body-region distinction but instead show greater overlap in guard hairs than in other hair types (Figure 2.4). Peripheral somatotopic organization is maintained within the LTMR central projections, with this structure being influenced by body region innervated, LTMR subtype, and orientation of the corresponding peripheral axons. Together, these findings provide fundamental insights into how LTMR projections are organized and thus how tactile information is integrated and transformed in the CNS in a somatotopically meaningful way. In an endeavor to gain genetic access to the neuronal populations of the deep dorsal horn that lie post-synaptic to LTMRs, we generated and utilized an array of mouse molecular genetic tools that illuminate the cellular and synaptic landscape and organizational logic of the mechanosensory dorsal horn. We found that the LTMR-RZ, which is critical for sensorimotor gating (Bui et al., 2013; Duysens and Pearson, 1976) and touch perception (Figure 3.9 of the present study), exhibits remarkably intricate neuronal and synaptic complexity. These findings strengthen the contention that a labeled line model of tactile information processing inaccurately reflects the complexity and malleable nature of touch perception.

5.1. Implications for peripheral organization of LTMR subtypes

Each LTMR subtype exhibits a combination of unique qualities that together influence individual neuronal responses to mechanical stimuli to ultimately shape tactile experiences and perception. Such qualities include, but are not limited to: association with peripheral end organs, such as hair follicles or Merkel cells; the number and distribution of axonal endings in the periphery (consider Aβ SAI- and Aβ Field-LTMRs, which innervate 1-2 or up to 180 hair follicles, respectively); axon conduction velocity; and modulatory inputs within the CNS, such as inhibitory axo-axonic synapses. As the skin is the site of initial LTMR stimulation and activation, understanding the basic organization of LTMR peripheral endings as a population can be profoundly informative when considering the processing of tactile information, and thus, can be considered one such quality that sculpts LTMR responses to mechanical stimuli.

The majority of LTMRs within a single subtype population are largely non-overlapping in the periphery, and the function of such 'tiling' maybe interpreted in several ways. First, this finding can be considered analogous to observations of 'tiled' neuronal organization in other areas of the nervous system, where neurons self-avoid or avoid cells of the same functional type to maximize coverage of shared territory and minimize redundancy (Grueber and Sagasti, 2010). This phenomena has been observed in a number of sensory systems, including in the tiling of leech or *Drosophila* mechanosensory neurons (Grueber et al., 2002; Kramer and Kuwada, 1983), *Drosophila* olfactory projection neurons (Zhu and Luo, 2004), and retinal ganglion cells within the mammalian retina (Dacey, 1993; Wassle and Riemann, 1978; Wässle et al., 1981). The utility of a ‘tiled’ organization of LTMR endings in the periphery indicates that each individual LTMR neuron of a particular subtype is performing the same function or has a uniform response property, as has been shown in other systems and organisms. Second, these results indicate that the majority of our genetic tools for targeting LTMR subtypes likely label irreducible populations. As redundancy is costly to biological systems (Barlow, 2001, 2012), the existence of profound overlap in any one population may be explained by the assumption that these two (or three) neurons innervating a single hair follicle are performing different tasks within the circuit. In the case of Aβ RA-LTMRs, it is possible that our genetic labeling strategy using Ret^{CreER} (Luo et al., 2009) may label two or more separate populations that have distinguishing qualities not apparent through present physiological recording experiments. However, the finding that these and Aβ Field-LTMRs show greater within-population overlap at guard hairs than zigzag and awl/auchene hairs may be indicative of a functional role for this overlap. In the mouse, guard hairs are longer, less prevalent, and more widely dispersed than zigzag and awl/auchene hairs, and thus, are likely stimulated under different conditions than other hairs. Computations and circuits engaged by guard hair deflection or movement may therefore be unique compared to those engaged by that of zigzag and/or awl auchene hairs. Interestingly, while all Aβ RA-LTMRs innervate several (five to forty) awl/auchene hair follicles, only a subset of those *also* innervate one to two guard hairs (unpublished observation). This distinction, innervation of guard hairs or lack thereof, may indicate that Aβ RA-LTMRs can be subdivided into two functional subtypes with unique functions in tactile processing. The peripheral organization of LTMR populations presented in this study offers some clues as to the organization of LTMRs and thus to the somatotopic nature of touch. Noteably, sensory systems are under many constraints that determine the ultimate neural architecture, from evolutionary inheritance, and metabolic constraints, to the existence of electrical noise (Gazzaniga, 2004). Any number of these constraints could also be influencing the organizational principles observed in both the peripheral and central projections of LTMRs.

5.2. Somatotopic and organizational logic of LTMR peripheral and central projections

The organizational principles uncovered in this study reveal clues as to how the sensation of touch to a particular region of skin is translated from this two-dimensional space into the intricate three-dimensional neural circuits of the spinal cord in a somatotopically relevant fashion. The observation that all LTMRs show a greater volumetric representation and alignment within the rostrocaudal axis of the spinal cord may be only a function of anatomical spatial constraints, as the spinal cord is indeed much longer than it is wide, but this observation may also inform our study of other components of touch circuitry. For example, the interneurons of the deep dorsal horn, the majority of which receive input from one or more LTMR subtype (Figure 4.9) are oriented with much more elaborate and lengthy neurites within the rostrocaudal axis as compared to observations of interneurons in lamina I-II (Figure 3.4 and (Yasaka et al., 2010). This organization argues that post-synaptic partners of LTMRs integrate across multiple LTMR subtypes from a small peripheral area, as opposed to integrating across one type of LTMR over a large area (as might be concluded if post-synaptic partners of LTMRs showed more expansive mediolateral neurites). This organizational logic would allow, at the first synapses of LTMR information, for the integration of *modalities across a small area* rather than the integration of one modality across a large area. In the same manner, it is possible that the central projections of LTMRs innervating abdomen hairy skin project caudally instead of rostrally due to anatomical space constraints. However, the absence of abdomen-innervating Aβ RA-LTMR projections to the DCN indicates that these neurons may be engaging different circuits than LTMRs innervating other regions of the body. Different regions of the body are stimulated under different external circumstances. This may provide an explanation of why anatomical projections of LTMRs differ across body regions. On a mouse, for example, hair follicles of the abdomen might be better suited than those of the back or thigh for detecting stimuli related to allogrooming, mating behaviors, nursing, surfaces, and vibrations conveyed from below. The observation that Aβ SAI-LTMRs show more dual innervation to Merkel endings in abdomen hairy skin than back or thigh may further support the idea that different functions of skin regions require different neuronal organizations.

The differences observed in somatotopic organization of central projections of LTMRs with adjacent or overlapping peripheral innervation indicate that the LTMR subtype itself may influence much of these ‘nearest-neighbor’ relationships. Why do Aδ- and C-LTMRs exhibit different organization of their central projections when their peripheral projections are comparable? Both innervate only zigzag and awl/auchene hairs, display largely non-overlapping peripheral anatomical receptive fields, and are optimally stimulated by hair follicle deflection (Abraira and Ginty, 2013; Li et al., 2011). C-LTMRs occupy less physical area within the spinal cord than Aδ-LTMRs, and although this may be somewhat accounted for by the observation that individual C-LTMRs on average innervate fewer hair follicles over a slightly smaller area (Bai et al., 2015), it may ultimately explain the observation that the central projections of Aδ-LTMRs show a great deal more overlap than those of C-LTMRs. One considerable difference between these two subtypes that might further explain these alignment differences is that Aδ-LTMRs have lanceolate endings that are concentrated on the caudal side of hair follicles, while C-LTMRs distribute their lanceolate endings evenly around the hair follicle (Rutlin et al., 2015). In fact, Aδ-LTMRs are the only LTMR subtype to show such polarization in anatomical endings, resulting in the preferential tuning to deflection of body hairs in the caudal-to-rostral direction (Rutlin et al., 2015). Thus, being inherently tuned to deflection in the rostrocaudal axis may contribute both to the differences in central alignment of Aδ- versus C-LTMRs, as well as the observation that Aδ-LTMRs align differently as a function of peripheral organization. Less overlap in central projections is observed between Aδ-LTMRs that align peripherally in the rostrocaudal plane than those aligning mediolaterally. With the innate sensitivity to rostrocaudal deflection "built-in" to Aδ-LTMR activation, perhaps a second signal to post-synaptic partners would be redundant. Activation of multiple Aδ-LTMRs with mediolateral alignment may thus converge on postsynaptic partners to convey relative "intensity" of stroke or hair deflection, as the central projections are often almost entirely overlapping. With distinct central branching patterns and post-synaptic partners, deciphering this anatomical organization of LTMRs is just one clue into the complex realm of touch processing in the spinal cord dorsal horn.

5.3 LTMR-RZ interneuron diversity and implications for innocuous touch processing

The LTMR-RZ is comprised of a highly diverse array of at least 11 interneuron subtypes, each distinguished from the others by a unique combination of physiological, morphological, and neurotransmitter properties. LTMR-RZ interneuron heterogeneity is further reflected by the observation that each interneuron subtype receives a unique combination of inputs from LTMR subtypes, other LTMR-RZ interneurons, and corticospinal neurons. Indeed, no two LTMR-RZ interneurons exhibit the same combination of physiological and morphological properties and patterns of LTMR synaptic inputs. For example, $Cdh3^+$ inhibitory interneurons are distinguished by their radial-like morphology, gap action potential discharge patterns, few if any spines, a large number of synaptic inputs from Aβ RA-LTMRs, and the formation of both axoaxonic and axodendritic synapses. Conversely, $PKC\gamma^+$ excitatory interneurons exhibit islet-like morphologies and an abundance of spines, delayed firing patterns, and receive synaptic inputs from Aδ-LTMRs and C-LTMRs, but not an appreciable amount of input from Aβ RA-LTMRs. Thus, as a result of the profound diversity of LTMR-RZ interneuron subtypes, and the integrative circuits they engage, analysis of the LTMR-RZ as a whole, rather than of single interneuron types or lineages, will be needed to advance understanding of the function of the dorsal horn as a tactile information processing center. It is within this context that the purpose of LTMR-RZ interneuron subtype morphological, physiological, and synaptic diversity will be revealed.

5.4. LTMR input comparisons, parallel processing modules and descending cortical input define innocuous touch processing in the mechanosensory dorsal horn

Four principles emerge from consideration of the cellular and synaptic architecture of the mechanosensory dorsal horn. The first stems from our observation that each LTMR-RZ interneuron receives direct synaptic input from multiple LTMR subtypes in a manner that is not simply a reflection of its laminar position. For example, PKCγ^+ interneurons receive predominantly C-LTMR and Aδ-LTMR input, and negligible Aβ RA-LTMR input, whereas other, neighboring interneuron subtypes receive Aβ RA-LTMR and Aδ-LTMR synapses but few if any C-LTMR synapses (Figure 4.9A). Thus, LTMR-RZ interneuron subtypes sample unique combinations of LTMR inputs, and interneuron outputs may therefore be defined by weighted averages of distinct input modalities. Because LTMR subtypes differ in tuning properties, action potential conduction velocities, receptive field sizes and adaptation properties, the outputs of LTMR-RZ interneuron subtypes have, in principle, the potential to reflect a myriad of ensembles of LTMR subtypes. Thus, LTMR and LTMR-RZ interneuron subtype diversity and their broad, overlapping synaptic arrangements at the earliest stages of LTMR inputs to the CNS may underlie our ability to perceive a “rainbow” of tactile experiences. Indeed, the cellular and synaptic complexity of the LTMR-RZ may provide a rich substrate for touch information processing that underlies perception of texture, direction and velocity of movement of tactile stimuli, stiffness, acuity, and form/shape or their precursors, encoded by virtually unlimited ensembles of LTMR activities, and, through modification by descending input, different states of sensitivity.

The second principle is parallel LTMR processing modules, which emerges from two basic observations. First, individual LTMR subtypes diverge to directly contact four or more postsynaptic LTMR-RZ interneuron classes. This is most dramatically exemplified by the synaptic partner profile of Aδ-LTMRs, which show a strikingly even distribution across each of the 11 LTMR-RZ interneuron subtypes described (Figure 4.10). Second, in considering the entirety of the excitatory connectome for each LTMR-RZ interneuron type, individual LTMR subclasses represent a minor fraction of the inputs, ranging from 0 to 30% at most (Figure 4.9). This finding indicates sparse LTMR input allocation that is distributed broadly across the LTMR-RZ, a synaptic architecture best described as parallel LTMR input modules. A major implication of these parallel channels is increased network interconnectivity. Indeed, in order for a sparse sensory input to perturb a network there must be sufficient network interconnectivity such that alterations in the activity of a few neurons can spread to other neurons in the network (Bui and Brownstone, 2015; Feldt et al., 2011; Laurent, 2002; Morgan et al., 2016; Rozell et al., 2008). Our observation that the vast majority of synapses formed by LTMR-RZ interneurons reside within the LTMR-RZ itself (Figure 4.3B), coupled with the finding that the majority of excitatory inputs that form onto all 11 LTMR-RZ interneurons originate in the spinal cord (Figure 4.1C), indicates a high degree of interconnectivity within the LTMR-RZ. This is also evident in subtype specific LTMR-modules. For example, a "C-LTMR specific module" would include PKCγ^{+} and PV^{+} interneurons (Figure 4.10), and within the C-LTMR recipient zone there appears to be a high degree of PKCγ-PV interneuron interconnectivity (Petitjean et al., 2015). Performing LTMR input computations in parallel rather than hierarchically enables enormous cellular and circuit-level substrate for integration, plasticity, and context-specific output and may enable selective gating of certain modalities under particular physiological states.

The third principle is that excitatory synaptic input from corticospinal neurons is broad and directly engages each LTMR-RZ interneuron (Figure 4.9A, 4.10), with little evidence for pre-synaptic modulation (Figure 4.4A). At the most basic level, the presence of robust cortical input targeting the LTMR-RZ and, remarkably, not the superficial dorsal horn (Lamina I-IIiv, Figure 4.1B), suggests that the LTMR-RZ is a locus for modulation during conscious tactile exploration. Our observation that cortical inputs are evenly allocated across all interneuron subtypes suggests that cortical activity may have the capacity to influence the gain of all innocuous touch circuit modules. Indeed, electrical activation of somatosensory cortex in cats is sufficient to induce dorsal root potentials, a reflection of presynaptic inhibition (Rudomin and Schmidt, 1999; Russo et al., 2000), thereby engaging circuits that modulate gain, presumably through PVi and/or Cdh3$^+$ interneurons, which form axo-axonic inhibitory synapses upon LTMR terminals (Figure 4.4C-D). Just as efference copies of motor command pathways within the spinal cord are implicated in defining active versus passive movements (Seki and Fetz, 2012), the nature of descending cortical inputs to the LTMR-RZ, which resemble LTMR inputs in terms of both broad distribution of LTMR-RZ interneuron targets and overall numbers of synapses, suggests to us that the LTMR-RZ is a locus for enabling gain modulation during periods of active tactile exploration versus passive touch (Fanselow and Nicolelis, 1999). Thus, we speculate that LTMR-RZ interneurons receive inputs from both LTMRs and cortex to sensitize or desensitize tactile pathways, possibly in a modality-specific and somatotopically-organized manner, to differentially process tactile inputs during tactile exploration and passive touch.

The fourth, and arguably most notable principle to emerge from this study, is that convergent LTMR inputs engage both LTMR-RZ interneurons and ascending outputs to the brain in a manner that is essential for touch perception. Inactivation of large cohorts of excitatory and inhibitory LTMR-RZ interneurons using an intersectional genetic strategy revealed that interneurons within this spinal cord region are necessary for the perception of texture and normal hairy skin sensitivity (Figure 3.9). Moreover, PSDC neurons, a major output neuronal population of the LTMR-RZ, receive both direct inputs from Aβ-LTMRs and indirect inputs from LTMR-RZ interneurons, which are themselves synaptic partners of two or more LTMR subtypes as well as cortical neurons. Electrophysiological recordings of PSDC neurons reveal them to be activated directly by Aβ-LTMRs and indirectly by Aβ-LTMRs, Aδ-LTMRs, and possibly C-LTMRs, via excitatory and inhibitory LTMR-RZ interneurons (Figure 4.11). These findings, taken together, indicate that processing of innocuous touch information relevant for perception begins in the LTMR-RZ and is conveyed from the LTMR-RZ to the brain via postsynaptic ascending pathways.

The present findings support an integrative model of cutaneous tactile processing that incorporates four principles. First, the LTMR-RZ comprises 11 or more physiologically and morphologically distinct LTMR-RZ interneuron types, each of which integrates inputs from multiple cutaneous LTMR subtypes. Second, sparse LTMR subtype input allocation distributed upon 4 to 11 interneuron subtypes suggests a parallel processing channel architecture within the LTMR-RZ. Third, corticospinal projection neurons provide a major LTMR-RZ input that is also sparsely allocated across each of the 11 LTMR-RZ interneuron subtypes. Fourth, LTMR-RZ interneurons are essential for tactile discrimination and perception. Furthermore, at least one class of LTMR-RZ ascending output neurons integrates direct Aβ-LTMR inputs and multiple, indirect modulatory inputs from excitatory and inhibitory LTMR-RZ interneurons, to convey processed touch information to the brain. These four themes are best considered in the context of a highly integrative model of innocuous touch information processing in the spinal cord. In this model, LTMR subtype activity ensembles emanating from the skin, as well as modulatory inputs from the cortex, converge upon 11 LTMR-RZ interneuron subtypes, each serving as a functionally distinct integrator of tactile modalities and descending cortical inputs, to orchestrate patterns of ascending LTMR-RZ projection neuron impulses that underlie touch perception.

5.5. Conclusion

Evidence provided in this study and others has revealed that the mechanosensory dorsal horn is a site of major integration and processing of tactile information. LTMR inputs, organized in the periphery to minimize redundancy within single subtype populations, are conveyed to the spinal cord in a somatotopically organized fashion. Within the dorsal horn, LTMR inputs from the same patch of hairy skin converge and align to synapse onto second order neurons along with convergent information from within the spinal cord and cortex. We thus propose an integrative model for touch information processing in which LTMR activity ensembles emanating from the skin and descending modulatory input from the cortex converge upon an array of LTMR-RZ excitatory and inhibitory networks.

These networks are comprised of 11 or more morphologically, physiologically and synaptically distinct LTMR-RZ interneuron subtypes that function to sculpt the activity of ascending pathways which, together with the direct dorsal column pathway, underlie tactile discrimination and perception.

EXPERIMENTAL PROCEDURES

Mouse lines

Mouse lines generated and analyzed for dorsal horn interneuron expression are described in Tables 3.1-3.2. Other published mouse lines used include *CCK*^{iresCre} (Jax#012706); *Rorβ*^{iresCre} (Jax#023526); *PV*$^{2A\text{-}CreER}$ (Jax#028580); *R26*^{CreER} (Jax#004847); *R26*$^{LSL\text{-}YFP}$(Ai3) (Jax#007903); *R26*$^{LSL\text{-}tdTomato}$(Ai9) (Jax#007909); *R26*$^{LSL\text{-}FSF\text{-}TdTom}$ (Ai65) (Jax#021875); *R26*$^{LSL\text{-}FSF\text{-}JAWS\text{-}GFP}$ (Ai57) (Madisen et al., 2015); *R26*$^{LSL\text{-}FSF\text{-}CatCh\text{-}eYFP}$ (Ai80) (Madisen et al., 2015); *R26*$^{LSL\text{-}synaptophysin\text{-}tdTomato}$ (Ai34) (Jax#012570); *R26*$^{LSL\text{-}ChR2\text{-}YFP}$(Ai32) (Jax#012569); *R26*^{iAP} (Badea et al., 2009); *Advillin*^{Cre} (Hasegawa et al., 2007); *Emx1*^{Cre} (Jax#005628); *Lbx1*^{Cre} (Sieber et al., 2007); *vGlut2*^{iresCre} (JAX#016963); *vGAT*^{iresCre} (JAX#016962); *GAD2*$^{2A\text{-}mCherry}$ (JAX#023140); vGluT2-YFP (JAX#017978); *GAD67*^{GFP} (Tamamaki et al., 2003); GlyT2-GFP (Punnakkal et al., 2014); *RC::FPSit* (Niederkofler et al., 2016); *RC::PFtox* (Kim et al., 2009). Published LTMR-CreER lines include *TrkB*^{CreER} (Rutlin et al., 2015); *TrkB*$^{Tau\text{-}GFP}$ (Li et al., 2011); *Ret*^{CreER} (Luo et al., 2009); *TrkC*^{CreER} (Bai et al., 2015), and *Ret*^{fCFP} (Uesaka et al., 2008) . Mice were handled and housed in accordance with the Harvard Medical School and Johns Hopkins University IACUC guidelines.

The following BAC transgenics and targeted alleles were generated for this study. The **Cdh3-CreER** (NIDA158), **5HTr6-CreER** (NIDA108) and **Kcnip2-CreER** (NIDA099) BAC transgenic mouse lines were generated by introducing a 4.7 kb CreERT2 cassette, pLD53.CreERT2, into the following bacterial artificial chromosomes, RP23-267K22 (Cdh3); RP23-65B16 (5HTr6) and RP23-146N4 (Kcnip2). A detailed step-by-step description of the BAC modification method has been published previously (Gong et al., 2010). Briefly, CreERT2 was inserted at the start site of the gene of interest via a two plasmid/ one-recombination step process. The modified BACs were expanded in E. coli, linearized by PI-SceI and microinjected in the pronuclei of fertilized C57BL/6 J embryos. In the case of RP23-146N4 (Kcnip2) linearization was done with NotI, instead of PI-SceI and the DNA subsequently run through a CL-4B hydrophobic interaction column. The ***PKCγ***^{myrGFP} and ***PKCγ***^{CreERT2} knock-in mice were generated using a targeting vector that was made utilizing a 2-step recombineering protocol (Liu et al., 2003). The genomic sequence of mouse PKCγ gene (strain 129S7/SvEv) was obtained from Ensembl Mouse Genome Browser. A 184kb BAC clone (bMQ_233p05) containing exon 1 of the *PKCγ* gene was obtained from SourceBioScience. A 4.7kb region (2.2kb-pre and 2.5kb-post first coding ATG of exon 1) from bMQ_233p05 was subcloned into a pBluescript-diptheria toxin A (PBS-DTA) plasmid via a first recombineering step. A myristoylated GFP (myrGFP) and Cre recombinase- estrogen receptor T2 (CreERT2) fusion *-Frt-Neomycin-Frt-loxP* cassette was introduced into the first coding ATG of exon 1 of the *PKCγ* gene via a second recombineering step. The ***Rorβ***^{CreERT2} knock-in mice were generated using a targeting vector that was made utilizing a 2-step recombineering protocol (Liu et al., 2003). The genomic sequence of mouse *Rorβ* (strain NOD/LtJ) was obtained from Ensembl Mouse Genome Browser. A 167kb BAC clone (CH29-604B6) containing exon 1 of the *Rorβ* gene was obtained from CHORI. A 9.7kb region (1.3kb-pre and 8.4kb-post first coding ATG of exon 1) from CH29-604B6 was subcloned into a pBluescript-diptheria toxin A (PBS-DTA) plasmid via a first recombineering step. A *Cre recombinase-estrogen receptor T2* (CreERT2) fusion-*Frt-Neomycin-Frt-loxP* cassette was introduced into the first coding ATG of exon 1 of the *RORβ* gene via a second recombineering step. The last 4bp of *RORβ* exon 1 were replaced. ***TH***$^{\boldsymbol{2A\text{-}CreER}}$ knock-in mice were generated using a targeting vector that was made utilizing a 2-step recombineering protocol (Liu et al., 2003). The genomic sequence of mouse *TH* (strain 129S7/SvEv) was obtained from Ensembl Mouse Genome Browser. BAC clone bMQ_453O04 containing exon 13 of the *TH* gene was obtained from SourceBioScience. A 9.15kb region (5kb pre-3'UTR and 4.1kb including and post 3'UTR) from bMQ_453O04 was subcloned into a pBluescript-diptheria toxin A (PBS-DTA) plasmid via a first recombineering step. A Cre recombinase- estrogen receptor T2 (CreERT2) cassette was introduced after a T2A peptide coding sequence immediately before the start of the 3'UTR of the tyrosine hydroxylase gene, and a *Frt-Neomycin-Frt-loxP* introduced directly after the 3'UTR via a second recombineering step. The ***Advillin***$^{\boldsymbol{FlpO}}$ knock-in mice used in experiments shown in Figure 4.1D will be described elsewhere (Travis Dickindesher and DDG unpublished). **Cdx2-NSE-FlpO** BAC transgenic animals were generated from the previously described vector for generation of the Cdx2-NSE-Cre BAC transgenic line (Coutaud and Pilon, 2013a) by replacing the Cre cassette with FlpO using standard cloning techniques. Cdx2-NSE-FlpO transgenic DNA was microinjected in FVB/N oocytes in accordance to standard methods. Offspring were screened for PCR-based genotyping of tail DNA using specific FlpO recombinase primers (forward within NSE sequence: 5'TAGCCAGACTCCTGCCTGAT3', reverse within FlpO sequence: 5'GTTCACGATGTCGAA GCTCA3'). Eight F0 transgenic animals were identified, of which only males (four in total) were tested for FlpO activity. FlpO activity was evaluated by crossing F1 male mice with *R26*$^{FSF\text{-}GFP}$ female animals and setting timed pregnancies using standard vaginal plug detection with noon of the day of plug considered at E0.5. Embryos at embryonic day 12.5 were collected and screened for caudal expression (as described in Figure S3.7). Of the four F0 lineages tested, one resulted in the correct recombination pattern. Two F1 males from this lineage were kept to propagate the Cdx2-NSE-FlpO mouse line via breeding with FVB/N females. Of note, Cdx2-NSE-FlpO transgene expression is sensitive to background, as described in (Coutaud and Pilon, 2013b), this likely reflects the fact that regulatory sequences used to generate this transgene were cloned from FVB genomic DNA.

Tamoxifen treatment

Tamoxifen was dissolved in ethanol (20 mg/ml), mixed with an equal volume of sunflower seed oil (Sigma), vortexed for 5-10 mins and centrifuged under vacuum for 20-30 mins to remove the ethanol. The solution was kept at -20^{o}C and delivered via oral gavage to pregnant females for embryonic treatment (E10-5-E13.5, as specified in the figure legends) or via intraperitoneal injection or oral gavage for postnatal treatments (P8-P25, as specified in the figure legends). For all analyses, the morning after coitus was designated as E0.5 and the day of birth as P0.

Mouse crosses for neurotransmitter phenotype analysis

The following mouse crosses were used to determine the neurotransmitter phenotype of the LTMR-RZ interneuron lines (Figure 3.3B). For each cross at least three animals were analyzed with at least 100 GFP^{+} cells counted per animal. For Cdh3 (*vGlut2*^{iresCre} or *vGAT*^{iresCre}*; R26*$^{LSL\text{-}TdTom}$(Ai9)*;*Cdh3-GFP); Cbln2 (*vGlut2*^{iresCre} or *vGAT*^{iresCre}*; R26*$^{LSL\text{-}TdTom}$(Ai9)*;*Cbln2-GFP); CCK (*vGlut2*^{iresCre} or *vGAT*^{iresCre}*; R26*$^{LSL\text{-}TdTom}$(Ai9)*;*CCK-GFP);

5HTr6 (*vGlut2*^{iresCre} or *vGAT*^{iresCre}*; R26*$^{LSL\text{-}TdTom}$(Ai9)*;*5HTr6-GFP); Igfbp5 (*vGlut2*^{iresCre} or *vGAT*^{iresCre}*; R26*$^{LSL\text{-}TdTom}$(Ai9)*;*Igfbp5-GFP); Kcnip2 (*vGlut2*^{iresCre} or *vGAT*^{iresCre}*; R26*$^{LSL\text{-}TdTom}$(Ai9)*;*Knip2-GFP); NeuroD4 (*vGlut2*^{iresCre} or *vGAT*^{iresCre}*; R26*$^{LSL\text{-}TdTom}$(Ai9)*;*NeuroD4-GFP); PKCγ (*vGlut2*^{iresCre} or *vGAT*^{iresCre}*; R26*$^{LSL\text{-}TdTom}$(Ai9) with Rb anti-PKCγ antibody, see antibody list at end of this section); PV (*vGlut2*^{iresCre} or *vGAT*^{iresCre}*; R26*$^{LSL\text{-}TdTom}$(Ai9) with Rb anti-PV antibody, see antibody list at end of this section); Rorβ (*vGlut2*^{iresCre} or *vGAT*^{iresCre}*; R26*$^{LSL\text{-}TdTom}$(Ai9)*;Rorβ*$^{\text{GFP}}$).

Mouse crosses for overlap matrix analysis

The following mouse crosses were used to determine the % coverage of LTMR-RZ by the genetically labeled interneuron mouse lines (Figure 3.6B). For each cross at least three animals were analyzed with at least 100 GFP$^+$ cells counted per animal. For tamoxifen regimens when CreER lines are used see Figure 3.2. For antibody species and dilution when immunohistochemistry is used see Figure 3.2. Excitatory matrix: *CCK*^{CreER}*;*Igfbp5-GFP*; R26*$^{LSL\text{-}Tom}$(Ai9). *CCK*^{CreER}*;*5HTr6-GFP*;R26*$^{LSL\text{-}Tom}$(Ai9). *CCK*^{CreER}*;*Cbln2-GFP*; R26*$^{LSL\text{-}Tom}$(Ai9). *CCK*^{CreER}*;*PV-Tom*;R26*$^{LSL\text{-}YFP}$(Ai3). *CCK*^{CreER}*;*NeuroD4-GFP*;R26*$^{LSL\text{-}Tom}$(Ai9). *CCK*^{CreER}*; R26*$^{LSL\text{-}Tom}$(Ai9) with PKCγ immunohistochemistry. 5HTr6-CreER*;*Cbln2-GFP*;R26*$^{LSL\text{-}Tom}$(Ai9). 5HTr6-CreER*;*NeudoD4-GFP*;R26*$^{LSL\text{-}Tom}$(Ai9). 5HTr6-CreER*;*Igfbp5-GFP*;R26*$^{LSL\text{-}Tom}$(Ai9). 5HTr6-GFP with PKCγ and PV immunohistochemistry. NeuroD4-GFP with PKCγ and PV immunohistochemistry. Cbln2-GFP with PKCγ and PV immunohistochemistry. Igfbp5-GFP with PKCγ and PV immunohistochemistry. WT tissue with PKCγ and PV immunohistochemistry. Inhibitory matrix: Cdh3-GFP with PV immunohistochemistry. *Rorβ*^{GFP} with PV immunohistochemistry. Kcnip2-GFP with PV immunohistochemistry.

Kcnip2-CreER*;*Cdh3-GFP*;* $R26^{LSL\text{-}Tom}$(Ai9). $Ror\beta^{CreER}$*;*Kcnip2-GFP*;*$R26^{LSL\text{-}Tom}$(Ai9). $Ror\beta^{CreER}$*;*Cdh3-GFP*;*$R26^{LSL\text{-}Tom}$(Ai9).

Behavioral testing

Male mice of a mixed genetic backgrounds (C57BL/6J and FVB/NJ) were used for behavioral analyses. Testing was done beginning at 7 weeks of age, and in most cases, was completed by 12 weeks of age. All animals were group housed, with control and mutant animals in the same litters and cages. Littermates from the same genetic crosses were used as controls for each group, to control for variability in mouse strains/backgrounds. Animal numbers per group for behavioral tests are indicated in figures. All behavioral analyses were done by observers blinded to genotype.

For a detailed protocol of texture NORT, see (Orefice et al., 2016). In brief, for NORT assays mice were first habituated to an open field chamber by allowing free exploration of an empty chamber for 10 minutes for two consecutive days (day 1 and 2). Each of the two subsequent testing days involving texture NORT (day 3) and color/shape NORT (day 4) included two sessions. In the first session (learning phase), the mouse was placed in the testing arena with two identical objects placed in the center of the arena. Each mouse was allowed to explore the objects for 10 minutes. Animals were then removed from the testing arena and placed in a transport cage for 5 minutes. During this time, the arena was cleaned with 70% ethanol, and one of the objects was replaced with a novel object. The mouse was then placed back into the chamber and allowed to explore objects for 10 minutes (testing phase). The amount of time the mouse spent physically investigating (touching) each of the objects was assessed during both the learning and testing phases. If an animal did not physically touch both objects during the learning phase, it was excluded from NORT analysis. For textured NORT, textured objects (either smooth or rough) were 4 cm on each side and constructed of plexiglass. For color/shape NORT, wooden blocks that differed in shape, size and color were utilized. To avoid confounding whisker movements and sensations, whiskers were plucked three days prior to the start of habituation. The position of the mouse was tracked using custom Matlab scripts. Whisking, nose pokes and investigation using the paws were all included in the time spent investigating objects, though for this assay over 90% of the time investigating objects is performed using the glabrous skin on paws (Orefice et al., 2016).

The response of mice to tactile and acoustic startle stimuli was measured using a San Diego Instruments startle reflex system (SR-LAB™ Startle Response System) (Orefice et al., 2016). In brief, for tactile PPI air puffs were administered to the back of the mouse to assess hairy skin sensitivity. A 1.5 PSI air puff prepulse stimulus strength was chosen because control animals of this particular Bl6/FVB mix showed a minimal, but statistically significant response to the stimulus alone, compared to baseline movement in the chamber without any stimulus (average response in controls, 8.19 ± 1.39%). Each mouse was placed in the chamber for a 5 minute acclimation period, during which constant background noise of broadband white noise was presented. Background noise for the acoustic PPI testing sessions was 65 dB. Background noise for the tactile PPI testing sessions was increased to 75 dB, to ensure that that the animal could not hear the air puff prepulse. Acoustic PPI and tactile PPI sessions were run on separate days. For acoustic PPI, the prepulse was 20ms in duration and presented 100ms before the startle pulse (inter-stimulus interval, ISI). For tactile PPI, the prepulse intensity remained constant (1.5PSI, 50ms), and the ISI was varied from 50ms to 1 second in duration.

Whole body flinch, or startle reflex, was quantitated using an accelerometer sensor measuring the amplitude of movement of the animal, within the cylindrical holder.

Skin injections

For mice aged P6 and younger, cryoanesthesia was used: pups are placed in a latex glove and immersed up to the neck in crushed ice and water (2-3°C) for 5-8minutes. Cryoanesthesia duration lasts ~10-15 minutes, during which time the skin injections were performed. Mice aged P10 and older were anesthetized via continuous inhalation of isoflurane (1-3%) from a precision vaporizer for the 5-15 minute duration of the surgery. The animal's breathing rate was monitored throughout the procedure and the anesthetic dose was adjusted as necessary. If necessary, the area being targeted for injection was shaved, treated with commercial depilatory cream (NAIR, Church and Dwight Co.; Princeton, NJ) for 0.5-1 min, and swabbed with ethanol and betadine. A beveled glass capillary needle (FHC Inc capillary tubing, FHC 27-30-0) was loaded loaded with AAV1-syn-FlpO (titre = 1.23E+13, UPenn Vector Core) together with a small amount of fast green (Sigma F7252-5G) in 0.9% saline. Using blunt forceps to pinch and stabilize the skin, the needle was inserted to target the dermis; AAV/fast green mixture was injected at a volume of 50nL to 1µL at each injection site. Each animal was injected at two to six locations, depending on the LTMR subtype being targeted. Following injection, analgesic (Carprofen, 4 mg/kg) was administered and animal was allowed to recover from anesthesia on a warm pad, with monitoring. After 24 hours, an additional dose of Carprofen was administered and animals were observed for adequate healing and recovery. Five to six weeks post-injection, animals were sacrificed by CO_2 asphyxiation followed by perfusion.

Dorsal column injections for PSDC labeling

Mice (P13-15) were anesthetized via continuous inhalation of isoflurane (1-3%) from a precision vaporizer for the 30-60 minutes duration of the surgery. The animal's breathing rate was monitored throughout the procedure and the anesthetic dose was adjusted as necessary. Puralube eye ointment was applied to the eyes. The back of the neck was shaved, treated with commercial depilatory cream (NAIR, Church and Dwight Co.; Princeton, NJ) for 0.5-1 min, and swabbed with water and Betadine. A 5 mm incision was made in the midline of the back skin at the cervical level and local anesthetic (0.5% lidocaine) was applied to the incision site. Muscles were cut or separated from the midline until the spinal cord cervical vertebrae were exposed. A small incision was made on the dura and arachnoid membranes immediately above the C1 cervical spinal vertebrae to expose the DCN. 100-200 nl of Adeno-Associated Virus (AAV2/1-CMV-Cre, titer 9.78e12 in 0.9% saline, Penn Vector Core), Rabies Virus (RabV-deltaG-GFP, titre 5.84E+7 - 9.48E+8 IU/mL, Salk Institute or Boston Children's viral core), or 100-300nl of CTB555 (2 μg/μl in PBS, Invitrogen) was injected into the DCN using a glass pipette under visual guidance. Afterwards, muscles and skin were stitched together with sutures, and Carprofen (4 mg/kg) was injected subcutaneously for analgesia. Mice recovered from anesthesia on a warm pad for 1 hour and were returned to their home cage (housed in groups of 5). Additional doses of Carprofen were injected intraperitoneally at 24 and 48 hours post-operation. The condition of the mice, including the healing of wounds, body weight, and grooming, was monitored daily. At the appropriate time point (4 weeks following AAV injections or 3-7 days following CTB or

RabV injections), mice were sacrificed by CO_2 asphyxiation followed by perfusion, or used for electrophysiology experiments.

Spinal cord slice preparation and electrophysiological recordings

Acute spinal cord sagittal slices were used for whole-cell patch clamp recordings of dorsal horn interneurons. Animals (P14-P21) were briefly anesthetized via continuous inhalation of isoflurane (1-3%) while the spinal column was removed. On cold choline solution (92mM Choline Chloride, 2.5mM KCL, 1.2mM NaH_2PO_4, 30mmM $NaHCO_3$, 20mM HEPES, 2.5mM Glucose, 5mM Sodium Ascorbate, 2mM Thiourea, 3mM Sodium Pyruvate, 10mM $MgSO_4$ $7H_2O$, 0.5mM $CaCl_2$ $2H_2O$) the lumbar enlargement was removed from the spinal column and mounted in 0.3% LMP agar for slicing in the sagittal plane (250-400µm, Leica VT1200S). Spinal cord slices were allowed to recover at 34°C for 30 min in ACSF containing 2.5mM CaCl2, 1mM NaH2PO4, 119mM NaCl, 2.5mM KCl, 1.3mM $MgSO_4$ $7H_2O$, 26mM $NaHCO_3$, 25mM dextrose, and 1.3mM Na ascorbate, saturated with 95% O_2, 5% CO_2 at a rate of ~2 ml/min. Following recovery, slices were placed at room temperature for 30min-1hr prior to recording. Cells were visualized by fluorescence to recognize fluorescent protein positive cells followed by infrared differential interference contrast microscopy for patching. Whole cell voltage-clamp recordings below the substantia gelatinosa were obtained under visual guidance using a 40x objective. The following mouse crosses were used to label each interneuron population for electrophysiology: PKCγ (*PKCγ*^{CreER}*;R26*$^{LSL\text{-}YFP(Ai3)}$ 2mg of tamoxifen at P15); Cbln2 (Cbln2-GFP); NeuroD4 (NeuroD4-GFP); PVe (*PV*^{FlpO}*;vGluT2*^{iresCre}*;R26*$^{LSL\text{-}FSF\text{-}TdTom}$(Ai65)); CCK (*CCK*^{CreER}*;R26*$^{LSL\text{-}YFP}$(Ai3) 2mg of tamoxifen at P15); 5HTr6 (5HTr6-GFP); Igfbp5 (Igfbp5-GFP); PVi (*PV*^{FlpO}*;vGAT*^{iresCre}*; R26*$^{LSL\text{-}FSF\text{-}TdTom}$(Ai65));

Kcnip2 (Kcnip2-GFP); Rorβ (*Rorβ*^{GFP}); Cdh3 (Cdh3-GFP). Voltage-clamp recordings from retrogradely labeled PSDCs in laminae IV-V were obtained under visual guidance using a 40x objective. Patch electrodes (4-6 MΩ) were filled with a KCl-based internal solution containing 125mM KCl, 2.8mM NaCl, 2mM $MgCl_2$, 2mM ATP-Mg^{2+}, 0.3mM GTP-Na^+, 0.6mM EGTA, and 10mM HEPES, and neurons were voltage clamped at -70mV. Action potential (AP) discharge patterns were studied in current-clamp. The membrane potential recorded ~10s after switching from voltage to current clamp was designated as the resting membrane potential (RMP) and subsequent recordings were made from this potential. AP discharge patterns were characterized by injecting a series of depolarizing step-currents (1.2s duration, 5-10pA increments, delivered every 6s, ranging from -80pA to 200pA) into the recorded neuron. AP discharge patterns were classified according to previously published criteria (Graham et al., 2004, 2007; Grudt and Perl, 2002; Yasaka et al., 2010). In brief, Initial Bursting (IB) neurons were characterized by AP discharge limited to the beginning of the depolarizing step; Delayed (D) firing neurons featured a prominent delay between the onset of the depolarizing step and AP discharge; Single Spiking (SS) neurons were characterized by the discharge of a single AP; Phasic (P) neurons were characterized by a burst of AP firing at rheobase (2-4 APs) that became persistent at steady state; Gap Firing (GF) neurons featured prominent gaps between AP at rheobase and/or steady state; and Reluctant (R) firing neurons did not discharge APs. Regular Spiking (RS) and Tonic (T) firing patterns were characterized by persistent AP discharge throughout the depolarizing and distinguished according to previously published criteria (Hughes et al., 2012). For dorsal root stimulation experiments, 300µm thick transverse spinal cord slices with dorsal roots attached were prepared as described above. Patch electrodes (2-4 MΩ) were filled with a CsCl-based internal solution containing 135mM $CsMeSO_3$, 4mM ATP-Mg^{2+}, 0.3mM GTP-Na^+, 1mM EGTA, 3.3mM QX-314(Cl^- salt), 8mM Na_2-Phoshocreatine and 10mM HEPES. Synaptic currents were evoked with electrical stimulation of dorsal roots using a suction electrode at Aβ fiber strength (≤25 µA, 20µs) (Nakatsuka et al., 2000; Torsney and MacDermott, 2006), and PSDC neurons were voltage-clamped alternatively at the reversal potential for synaptic inhibition and excitation to isolate excitatory postsynaptic currents (EPSCs) and disynaptic inhibitory postsynaptic currents (IPSCs), respectively. To activate ChR2 in acute slices, LED whole field illumination was used through a water immersion 40x objective. Aδ-LTMR axon terminals were stimulated with brief pulses (1-5ms) of blue light (473 nm, ~5mW). Input resistance and access resistance were monitored continuously throughout each experiment and cells were excluded from analysis if these values changed by more than 10% during the experiment or if the resting membrane potential was higher than -50mV. Data were acquired using a Multiclamp amplifier, a Digidata 1440A acquisition system, and pClamp10 software (Molecular Devices). Sampling rate was 10 kHz, and data were low-pass filtered at 3 kHz. No correction for junction potential was applied.

Skin and spinal cord whole-mount immunohistochemistry

Mice were anesthetized with CO_2 and perfused with 5-10mL modified Ames Media (Sigma) in 1x PBS, followed by 20-40 mL of 4% paraformaldehyde (PFA) in PBS at room temperature (RT). For hairy and glabrous skin, euthanized mice were treated with commercial depilatory cream (NAIR, Church and Dwight Co.; Princeton, NJ) for 0.5-1 min and washed with hand soap. Skin was dissected and fixed in Zamboni's fixation buffer and intact vertebral columns were fixed in 4%PFA at 4°C overnight. Following fixation, samples were washed 5x30min in 1xPBS at 4°C.

The protocol for skin whole-mount immunohistochemistry was performed as previously described (Bai et al., 2015). First, six to eight hours of one hour washes in 1% TritonX-100 in 1xPBS (PBST), then incubation with primary antibodies diluted in blocking solution (75% 1% PBST, 20% DMSO, 5% Normal Goat Serum, 0.02% NaN_3) on a rocking platform for 2-3 days. Primary antibodies are listed at end of this section. The skin was washed in PBST for 6-8 x 1 hour, then incubated with secondary antibodies in blocking solution on rocking platform for 2-3 days. Secondary antibodies included an array of species-specific Alexa Fluor 488, 546, and 647 conjugated IgGs (Invitrogen), The skin was washed again in PBST with 1% Triton X-100 for 6-8 x 1 hour and then dehydrated in 100% MeOH (3 x wash) overnight on a rocking platform. The next day, skin was pinned to a glass dish coated using Sylgard 184 Silicone Elastomer Kit (Dow), cleared in BABB (BABB: 1 part Benzyl Alcohol: 2 parts Benzyl Benzoate) for 5 min, and mounted on slides using BABB as mounting medium. All steps were completed at room temperature.

For steps proceeding spinal cord whole mount staining see also: Figure 2.6. The entire spinal cord with DRGs attached were dissected from the vertebral column, followed by fine dissection to remove dura and hemisect the spinal cord along the rostrocaudal plane. Tissue was then blocked in blocking solution (1% TritonX-100, 1% Tween-20, 5%

normal goat serum in 1xPBS) for 4 hours, followed by incubation with primary antibodies diluted in blocking solution on a rocking platform for 2-3 days. Primary antibodies are listed at end of this section. Spinal cords were then washed 6 x 1 hour in PBST (1% TritonX-100 in 1xPBS) and incubated in secondary antibodies diluted in blocking solution on a rocking platform for 2-3 days. Secondary antibodies included an array of species-specific Alexa Fluor 488, 546, and 647 conjugated IgGs (Invitrogen). Following this, cords were washed 6 x 1 hour in PBST and serial dehydrated in 50%, 75%, and 100% MeOH (2 hours each, and final overnight incubation in 100% MeOH). The next day, spinal cords were pinned to a glass dish coated using Sylgard 184 Silicone Elastomer Kit (Dow), cleared in BABB (BABB: 1 part Benzyl Alcohol: 2 parts Benzyl Benzoate) for 5 min, and mounted on slides using BABB as mounting medium. All steps were completed at room temperature.

Immunohistochemistry of vibratome sections

Mice (P30-P35) were anesthetized with CO_2 and perfused with 5-10mL modified Ames Media (Sigma) in 1x PBS, followed by 20-40 mL of 4% paraformaldehyde (PFA) in PBS at room temperature (RT). Vertebral columns (including spinal cords and dorsal root ganglia) were dissected from perfused mice and were post-fixed in 4% PFA at 4°C for 2-16 hours. A section of spinal cord, measuring ~3mm containing the lumbar region was removed from the tissue sample and sagittally sliced into 50-150μm sections in cold PBS with a vibrating blade vibratome (Leica VT100S). The tissue sections were removed from the vibratome chamber and placed into cold filtered PBS for immunohistochemistry (Polgár et al., 2013). In brief, tissue samples were rinsed in 50% ethanol/water solution for 30 minutes to allow for enhanced antibody penetration. Three washes in a high salt

Phosphate Buffer Saline (HS PBS) were conducted each lasting 10 minutes. The tissue was then exposed to a solution of primary antibodies in high salt Phosphate Buffer Saline containing 0.3% Triton-X-100 (HS PBSt) for 48-72 hours at 4°C. Primary antibodies are listed at end of this section. The tissue was then washed in HS PBSt three times and incubated in a secondary antibody solution in HS PBSt for 24 hours at 4°C. Secondary antibodies included an array of species-specific Alexa Fluor 405, 488, 546, and 647 conjugated IgGs (Invitrogen). The tissue was treated with another HS PBSt wash lasting 10 minutes, followed by a 4',6-diamidino-2-phenylindole (DAPI) stain at a 1:5000 dilution, lasting 10 minutes, and followed by a final PBSt wash also lasting 10 minutes. Tissue sections were mounted on glass slides and coverslipped with Fluoromount Aqueous Mounting Medium (Sigma). The slides were stored at 4°C.

Peripheral overlap quantifications

To assess the relative overlap of LTMR peripheral projections, whole mount staining, imaging, and quantification of DRG labeling was first conducted on LTMR-Cre;Ai3/Ai9 tissue. If labeling in red (Ai9), green (Ai3), and yellow (Ai3 and Ai9) was determined to be in approximately equal ratios (no one population >45% of DRG labeling), then skin was also processed for staining and analysis. WM stains on hairy skin were completed as described. For quantification of hairy skin, each hair follicle was observed and determined to have single, dual, or triple innervation (as determined by the number of colors of neurons innervating that hair). Color of neurons in skin was also tracked to ensure equal ratio of colors was conserved from DRG. Troma1 staining was used as a landmark when guard hairs needed to be distinguished from awl/auchene and zigzag hairs. For parsing out different body region innervation, the entire skin from the animal was removed and subsequently trimmed to isolate the region of interest before imaging. For all animals, a minimum of 50 awl/auchene and/or zigzag and 20 guard hair follicles from each body region were used for quantifications.

Neuronal reconstructions and morphometric analysis

Reconstructions of sparsely-labeled peripheral and central LTMR axonal projections (as shown in Figures 2.9 and 2.10) were completed using Neuromantic reconstruction software. Images were acquired on a Zeiss LSM 700 confocal microscope using a 20X lens (Plan-Apochromat 20X/NA 0.8). Images were converted to single-channel 8bit greyscale .tif files from the original .lsm files and reconstructions were done one channel at a time using the “semi-automatic” mode. Reconstructions were then pseudo-colored and merged in ImageJ.

The following mouse crosses were used to label interneuron populations for Neurolucida reconstructions, at least 3 animals per cross were used for analysis, number of neurons reconstructed per line as specified in the Figure 3.10 and 3.11 legends. For the unbiased approach depicted in Figure 3.1C ($R26^{CreER}$;$R26^{LSL\text{-}YFP}$(Ai3) 100ug of tamoxifen at E13.5). For the interneuron subtypes depicted in Figures 3.10 and 3.11: PKCγ ($PKC\gamma^{CreER}$;$R26^{LSL\text{-}YFP}$(Ai3) 2mg of tamoxifen at P15); Cbln2 (Cbln2-GFP); NeuroD4 (NeuroD4-GFP); PVe (PV^{FlpO};$vGluT2^{iresCre}$;$R26^{LSL\text{-}FSF\text{-}TdTom}$(Ai65)); CCK ($CCK^{CreER}$;$R26^{LSL\text{-}YFP}$(Ai3)) 2mg of tamoxifen at P21); 5HTr6 (5HTr6-GFP); Igfbp5 (Igfbp5-GFP); PVi (PV^{FlpO};$vGAT^{iresCre}$; $R26^{LSL\text{-}FSF\text{-}TdTom}$(Ai65)); Kcnip2 (Kcnip2-GFP); Rorβ ($Ror\beta^{CreER}$;$R26^{LSL\text{-}YFP}$(Ai3) 2mg of tamoxifen at P18); Cdh3 (Cdh3-GFP). Sagittal sections of lumbar spinal cord were immunostained as described above and z-stack images were taken on a Zeiss LSM 700 confocal microscope using a 20X lens (Plan-Apochromat 20X/NA 0.8). Analysis was limited to the LTMR-RZ, using IB4 (IIiv border) as an upper limit and 250μm below IB4 as a lower limit. Confocal image stacks were loaded into the Neurolucida 360 software. Specific neurons from each image stack were reconstructed using the user-guided reconstruction tool. Reconstructions were saved and opened in Neurolucida Explorer software for morphological analysis. Basic information detailing somatic and dendritic measurements were retrieved from the reconstructions using Neurolucida software and graphed with GraphPad Prism. Sholl-based metrics detailed in Figure 3.12 including: Enclosing radius, Sum of Intersections, Critical Value (Nm), Critical Radius (Rc), Mean Value (Nav), Centroid Value, Centroid Radius, Ramification Index (RI), Regression Coefficient (k), Branching Index (BI), were obtained by analyzing intersection-based sholl data obtained in Neurolucida with MATLAB script written using previously described formulas (Ferreira et al., 2014; Garcia-Segura and Perez-Marquez, 2014; Rajković et al., 2016). The depth location within the LTMR-RZ was measured from the bottom of the IB4$^+$ lamina IIiv using ImageJ software.

Linear Discriminant Analysis

We performed linear discriminant analysis (LDA) on 26 parameters collected from the neuronal morphometric analysis using the LDA function in R, on a total of 200 excitatory and 137 inhibitory interneurons. These 26 parameters were chosen from a total of 46 metrics and deemed to be most important to interneuron classification due to their negative effect on classifier performance when removed from the parameter dataset. Prior to running LDA, all data was scaled and centered to adjust for differences in magnitude between metrics, and interneurons were randomly split into a training set (90%) and test set (10%). LDA using the training set was used to create a classifier, for which performance was assessed with the test set. The process of random splitting into training and test sets, followed by LDA and test set classification, was iterated 10,000 times while recording the incidence of true positives (TP), true negatives (TN), false positives (FP), and false negatives (FN) resulting from classification of the test set. These values were used to calculate classifier precision, P = TP / (TP+FP); recall, R = TP / (TP+FN); fallout, F = FP / (FP+TN); miss, R = FN / (FN+TP); and accuracy, A = (TP+TN) / (TP+TN+FP+FN).

To ask which categories of metrics were most important to classifier performance, we performed LDA and interneuron classification as described above while removing categories of variables relating to either cell location (Distance Below IB4), soma morphology (Enclosed Volume, Max Perimeter, Area, Feret Max Soma, Aspect Ratio, Roundness, Mean Area, Surface Area), dendritic spines (Spines, Spine Density), or dendritic morphology (Dendrite Quantity, Nodes, Length, Volume, Torsion Ratio, Convex Hull Volume, Convex Hull Area, Sum of Intersections, Critical Value, Critical Radius, Centroid Radius, Ramification Index, Regression Coefficient, Branching Index). The heatmap.2 function in R was used to construct a heatmap representing the reduction in classifier accuracy resulting from removal of these metrics.

Synaptic analysis

Within the LTMR-RZ, vesicular glutamate transporters (vGluTs) are well-established markers to label peripheral, local excitatory interneurons, and cortical pre-synaptic inputs, with differences in which vGluT subtype each population expresses. Established LTMR subtypes also display unique vGluT expression: C-LTMRs in the mouse express vGluT3 while Aβ- and Aδ-LTMRs express vGluT1 (Seal et al., 2009; Todd et al., 2003). Descending excitatory cortical projection neurons express vGluT1 while local excitatory interneurons express vGluT2 (Du Beau et al., 2012; Todd et al., 2003). Homer protein family members are expressed at postsynaptic densities (PSDs) of glutamatergic synapses where they play crucial roles in synaptic scaffolding and Ca^{2+} signalling. Importantly, Homer proteins are located further from the synaptic cleft (~80nm) than other established markers of excitatory PSDs such as Shank proteins, PSD-95, or GluR1 subunits, making it possible to label these proteins without antigen retrieval (Dani et al., 2010; Gutierrez-Mecinas et al., 2016), and furthermore, Homer protein has been shown to be present at the majority of glutamatergic synapses within the dorsal horn (Gutierrez-Mecinas et al., 2016). Thus, in this study, Homer1 is used to detect the presence of all excitatory glutamatergic synapses, with the combined use of pre-synaptic markers, including vGluT1 and genetically expressed synaptophysin-tdTomato (via Ai34).

LTMR-RZ synaptic architecture analysis. Sagittal sections of lumbar spinal cord (50μm) were immunostained as described above and z-stack images were taken on a Zeiss LSM 700 confocal microscope using a 20X lens (Plan-Apochromat 20X/NA 0.8). Analysis was limited to the LTMR-RZ, using IB4 (IIiv border) as an upper limit and 250μm below IB4 as a lower limit. Apposition analysis with $Homer1^+$ and $Ai34^+$ puncta was completed using published methods (Ippolito and Eroglu, 2010). For each animal used in analysis, a minimum of 5 sets of images, each image set comprising (2) 5μm z-stacks from a minimum of 3 separate sections, was used for analysis. Input analysis of synaptophysin-toTomato overlap with vGluT1 was analyzed using ImageJ software to isolate *Emx1*^{Cre};Ai34 or *Advillin*^{Cre};Ai34 puncta contained within vGluT1^{+} puncta; these puncta were subsequently counted using the Puncta Analyzer plugin. For each animal included in the analysis, a minimum of of 2 sets of images, each image set comprising (2) 3μm z-stacks, was used.

For determining the number of synapses per individual LTMR, as shown in Figure 4.2, whole mount staining was performed on perfused, post-fixed spinal cords from adult (P30-P35) mice. Tiled z-stack images were taken on a Zeiss LSM 700 confocal microscope using a 20X lens (Plan-Apochromat 20X/NA 0.8) and used for subsequent analysis. For each image, ImageJ software was used to crop to a region of interest that contained only the central projection & synapses from a single neuron. These cropped images were blinded for subsequent analysis, in which the ImageJ Cell Counter plugin was used to count total synaptophysin-tdTomato^{+} puncta per neuron (based on a minimum size and intensity threshold). A minimum of 1 (for Aβ RA-LTMRs) or 3 (for C- and Aδ-LTMRs) cells were quantified per animal, with cells sampled across cervical, thoracic, and lumbar regions for all subtypes. Averages of these counts (n=4 animals per LTMR subtype) yield the average number of synapses per neuron. To calculate total synaptic input from each LTMR population, the average number of synapses per C-, Aδ-, or Aβ RA-LTMR was multiplied by the relative abundance of these subtypes in the DRG, previously reported as 15-20%, 7%, and 5% of total DRG neurons, respectively (Li et al., 2011; Luo et al., 2009; Rutlin et al., 2015). Further multiplication using an average of 10,000 neurons per mouse DRG (Gjerstad et al., 2002b), and 62 DRGs (8 cervical, 13 thoracic, 6 lumbar, 4 sacral DRGs per side) completes the calculation to yield total synaptic input from each population (puncta per population = (puncta/neuron) × (% of DRG) × 62,000).

Distribution analysis of LTMR-RZ interneuron synapses. Sagittal sections of lumbar spinal cord (50µm) were immunostained as described above and z-stack images were taken on a Zeiss LSM 700 confocal microscope using a 20X lens (Plan-Apochromat 20X/NA 0.8). Low-level expression of synaptophysin-tdTomato in cellular cytosol was used to locate sparsely labeled cells and follow neurites to all tdTom^+ synapses. ImageJ software and multipoint tool was used for marking synapses and exporting coordinates; center of cell soma and lamina IIiv border (using IB4 binding) were also marked and measured. Synaptic coordinates were then converted into their location in the dorsal-ventral axis relative to IB4. Cells with somas residing outside of the LTMR-RZ were not included in the analysis. A minimum total of 10 cells from 3 animals was used in this synaptic distribution analysis.

Analysis of pre- and post-synaptic inhibitory contacts from LTMR-RZ interneurons. Transverse sections of lumbar spinal cord (60µm) were immunostained as described above and were scanned with a Zeiss LSM 710 confocal microscope equipped with argon multiline, 405 nm diode, 561 nm solid state, and 633 nm HeNe lasers, and a spectral detection system. Image stacks were obtained through a 63x oil-immersion lens (numerical aperture 1.4) and scanned at a z-separation of 0.3 µm. The resulting z-stacks of were analysed with Neurolucida for Confocal software (MBF Bioscience, Williston, VT). Laminar boundaries were determined by mapping the expression patterns of PV and vGluT1 (for laminae IIi and III), and overlaying templates of appropriate spinal segments obtained from the Allen Brain Atlas (www.brain-map.org) onto projected images of immunolabeled sections.

For analyzing inhibitory contacts to myelinated afferents (*Advillin*^{Cre}*;*Ai34) and descending corticospinal projections (*Emx1*^{Cre}*;*Ai34) (n=4 animals for each line), only channels corresponding to the reporter and vGluT1 were initially viewed and fifty boutons that contained either reporter and vGluT1 or only vGluT1, were selected randomly in each lamina. The channel corresponding to the vGAT labelling was then viewed. The proportion of terminals from either group that were contacted by vGAT terminals, and the mean number of vGAT contacts onto these boutons, was then determined.

For characterizing inhibitory inputs to vGluT1^{+} boutons in the LTMR-RZ from Cdh3^{+} (Cdh3-GFP*)*, PV^{+} (immunostaining), Rorβ^{+} (*Rorβ*^{CreER}*;*Ai34), and Kcnip2^{+} (Kcnip2-CreER*;*Ai34) interneurons (n=4 animals for each interneuron population), we first used Neurolucida for Confocal to randomly select fifty axon terminals per lamina that contained both the reporter and vGAT from confocal image stacks from each animal. The channel corresponding to vGluT1 labelling was then viewed, allowing us to determine the proportion of inhibitory terminals from each reporter line that target vGluT1 boutons in the LTMR zone. We then randomly selected fifty vGluT1 terminals from each lamina, before revealing the vGAT labelling followed by viewing the channel for the reporter. This allowed us to determine both the number of vGAT terminals in contact with each vGluT1 terminal, and the proportion of these terminals that expressed the reporter labeling. To determine the proportion of inhibitory reporter terminals that mediate postsynaptic (rather than presynaptic) inhibition in the LTMR recipient zone, a total of fifty reporter-expressing terminals that were also vGAT-immunoreactive were selected randomly (n=3 animals for each interneuron population). Confocal image stacks were then analyzed using Neurolucida for Confocal to determine the proportion of inhibitory reporter terminals that apposed a gephyrin-immunoreactive punctum.

Array tomography. Anatomical synaptic contacts were validated using array tomography to confirm overlap of synapses from primary sensory neurons ($\textit{Advillin}^{\textit{FlpO}}$;$\textit{R26}^{\textit{FSit}}$) with synaptic markers used in this study as well as other known synaptic markers. This procedure was completed by the Harvard Neurobiology Imaging Facility and analysis was conducted as previously published (Saunders et al., 2015). Mice used for this analysis were perfused as described above; lumbar spinal cord samples were post-fixed at 4°C overnight, rinsed 3 x 30min in 1xPBS, and sectioned into 150μm slabs using a vibratome (Leica VT100S). Lumbar spinal cord was then dehydrated, embedded in LR white resin and serially sectioned at 70nm using an ultramicrotome (Saunders et al., 2015). After embedding and before sectioning, dorsal and ventral horns of the spinal cord were visually identified by morphological differences, and ventral horns were trimmed from block to ensure the appropriate region of the spinal cord was isolated for subsequent imaging and analysis. Staining, imaging, and post-imaging alignment and background subtraction was performed as previously described (Saunders et al., 2015); see table at end of this section for antibodies used. DAPI and GFP staining were used to determine regions of interest within the LTMR-RZ on each section. Four images were then acquired and stitched into a final image; DAPI staining across each staining session was used to align images across imaging sessions. Image analyses were carried out using previously written MATLAB scripts provided by the lab of Dr. Bernardo Sabatini (Saunders et al., 2015). GFP volumes (defined by spanning multiple planes with minimum size and brightness thresholds) and synaptic markers (defined by minimum size and brightness thresholds) were computationally detected from image stacks, excluding DAPI nuclei and regions lacking tissue. Colocalization analyses of GFP and synaptic markers was performed within (distance = 0) and at varying distances outside (102-512nm) of GFP volumes. Mean occurrence of colocalization per voxel was compared to that of 1,000 rounds of randomized immunopunctae. Z scores were calculated for distance = 0 as follows: $[\mu_{actual}-\mu_{randomized}]/\sigma_{randomized}$ where μ is mean occurrence of colocalization per voxel and σ is standard deviation. A total of n = 3 animals with 2 stacks each (each stack comprising 25-35 70nm sections) was used for this analysis.

Input and connectivity analysis. Synaptic input and connectivity analysis (as presented in Figures 4.8-4.10) was performed on mice in which LTMR-RZ interneuron BAC-GFP transgenic lines were crossed with Cre and CreER lines of input populations of interest and the synaptophysin-tdTomato reporter line (Ai34). Thus, in a single animal, one LTMR-RZ interneuron population (Cbln2$^+$, NeuroD4$^+$, CCK$^+$, 5Htr6$^+$, Igfbp5$^+$, Kcnip2$^+$, Rorβ$^+$, or Cdh3$^+$) along with the pre-synaptic boutons of one input population (descending corticospinal projections, Aβ RA-LTMRs, Aδ-LTMRs, or C-LTMRs) were genetically labeled. Immunostaining allowed for the additional detection of PKCγ$^+$ and PV$^+$ interneuron populations in GFP-negative animals (PVe and PVi populations were distinguished by morphology), as well as pre- and post-synaptic markers used in the analysis (primarily vGlut1 and Homer1). All animals used in this analysis were perfused, postfixed, sectioned (50μm, lumbar spinal cord), and immunostained as described above.

Z-stack images of spinal cord slices were taken on a Zeiss LSM 700 confocal microscope using a 40X oil-immersion lens (Zeiss; Plan-Apochromat 40X/NA 1.40) and scanned at a z-separation of 0.5µm. Images were taken in lamina IIiv-IV of the dorsal horn, which was defined as between the lamina IIiv border (marked by IB4 binding) and 250µm below that border. Bias to particular regions of the LTMR-RZ (particularly in the dorsal-ventral axis) based on input population was actively avoided by not observing the input population channel until a particular interneuron cell was selected for imaging. Further, for interneuron populations spanning multiple laminae, cells were selected and imaged in a repeating order of dorsal to ventral, ensuring that dorsal and ventral components of the population were sampled for analysis. Imaging parameters (laser power, gain/offset, averaging, dwell time, etc.) were consistent across each stain on all animals. For example, Homer1 (Alexa Fluor 647 secondary) was imaged using the same parameters in *all* animals; whereas GFP (Alexa Fluor 488 secondary) was imaged using the same parameters for all Igfbp5-GFP animals, but would differ from that of the other BAC-GFP transgenic lines.

All images were first prepared for analysis using ImageJ: using the channel of interneuron labeling, two masks were generated - one using a standardized threshold for signal in this channel and a second by expanding this first mask by 1µm in all dimensions. These masks were then used to isolate pre- and post-synaptic labeling by multiplying these channels (using the Image Calculator function) with the expanded and non-expanded masks, respectively. Thus, when recombined for analysis, each image contained pre- and post-synaptic labeling that was restricted to sites of expanded or non-expanded GFP overlap, respectively (see Figure 4.6). Blinded images were then analyzed for these inputs by eye, using the Cell Counter ImageJ plugin. Anatomical excitatory inputs were identified using Homer1 antibody overlap with the labeled interneurons of interest; each Homer1$^+$ puncta represents one anatomical excitatory input. These excitatory inputs were defined as originating from an input population of interest when the pre-synaptic marker of that population (vGluT1 or synaptophysin-tdTomato) partially (minimum of 10% Homer1$^+$ pixels overlapping with input pixels) or fully overlapped with a Homer1$^+$ puncta. All analysis was restricted to neurons where the cell body was clearly in view and associated with the respective neurite. Puncta were counted as a factor of location: cell body, proximal neurite (within the first 50μm) or distal neurite (beyond the first 50μm). For each genotype, a minimum of 3 animals was used for analysis, with a minimum sampling from each animal of 4 neurons per cellular compartment (minimum total length of 500μm and 50μm analyzed for proximal and distal neurites, respectively).

For broad and LTMR subtype-specific connectivity profiles of each LTMR-RZ interneuron subtype (as presented in Figure 4.8A and 4.9A), synaptic input ratios were calculated as follows. From each cell, if multiple neurites were analyzed, the synaptic counts and neurite lengths were summed (keeping proximal and distal separate), and puncta per length (μm) and puncta per surface area (μm^2) were calculated for neurites and somas, respectively. Homer1$^+$ puncta represent total excitatory input to the cell, and so to obtain the proportion (%) of this excitatory input from a particular input population, Homer1$^+$Ai34$^+$ puncta per μm^2 were divided by total Homer1$^+$ puncta per μm^2. These values were subsequently divided by the input population normalization value to account for variability in labeling efficiency (see next paragraph). For each animal, these normalized values for proportion of excitatory input from each cellular compartment were then averaged across all neurons; these were then averaged to obtain the final normalized average +/- SEM (n=animal number) proportion of excitatory inputs. Thus, proportion (%) of excitatory input from input population 'A' = [(total # A^+homer1^+ puncta/µm) ÷ (total homer1^+ puncta/µm)] ÷ normalization value (this calculation is done separately for each cellular compartment). Subtractive calculations (such as those used in Figure 4.8A and 4.10) utilized these final averages across all animals of a particular genotype. For comparisons made between input populations, the normalized average puncta per µm for each input was totalled across all 11 interneuron lines, and the puncta per µm of inputs onto each interneuron subpopulation was divided by this total. The result of this computation is to show, of the anatomical inputs *onto these 11 interneuron populations*, what proportion is dedicated to each interneuron subtype.

Normalization value: The reliance on tamoxifen treatment for recombination and expression of synaptophysin-tdTomato in our LTMR-CreER lines presents the likelihood of variable labeling from animal-to-animal. Thus, for all animals analyzed, the average synaptophysin-tdTomato puncta per image area (µm^2) was calculated. Unprocessed images (the same as those used for the connectivity profile counts) were used to isolate synaptophysin-tdTomato puncta in a particular region of interest (the lamina-specific innervation target of that population) with a standardized threshold and then count total puncta number using the ImageJ Puncta Analyzer program. For each animal, a minimum of puncta counts from 3 images was obtained and averaged. These values were compared across all animals of a single Cre or CreER line, and the maximum synaptophysin-tdTomato puncta per µm^2 was determined. For each animal, the average puncta per µm^2

is then divided by this maximum value to determine the normalization value for labeling efficiency, which is subsequently used as described above. This was also completed for vGluT1 staining to account for differences in staining efficiency and to optimize subtractive calculations. Normalization value for input population ‘A’ = (total # A^+ puncta) ÷ (total area in ROI).

Statistical methods

All data are expressed as the mean +/- the standard error of the mean (SEM), unless otherwise stated in the figure legend.

For morphological/physiological comparisons a Student’s t-test was used to compare excitatory and inhibitory cohorts. One-way ANOVAs are expressed as an F-statistic and P-value within brackets, and post-hoc comparisons were performed using the post-hoc test indicated in the figure legend. The p values of post-hoc comparisons between groups are represented with asterisks above brackets over the indicated groups using a bracketed line in the figures.

For behavior, the number of animals per group used in each experiment is denoted within the bar for that group in each panel. Unless otherwise stated, a Student’s t-test was used to compare a group to chance performance (0% for NORT), or to compare mutants to their control littermates. If significant differences between mutants and control littermates were observed, this was indicated by an asterisk over the indicated groups. Main effects of genotype to tactile PPI from one-way ANOVAs are expressed as an F-statistic and P-value within brackets.

For LTMR-specific connectivity profiles, each input population was compared to a hypothetical mean (0%) using a one-sample t-test. If these values were not statistically significantly ($p>0.05$) above 0%, lack of significance was indicated by "n.s." above the respective bar graph. Comparisons between input populations onto a single interneuron population were performed using one-way ANOVA, and main effects from one-way ANOVAs are expressed as an F-statistic and P-value within brackets. Post-hoc comparisons were performed using Tukey's test. The p values of post-hoc comparisons between groups are represented with asterisks above brackets over the indicated groups using a bracketed line in the figures.

List of primary antibodies.

Primary Antibodies

Antigen	Host	Dilution	Supplier	Cat # or Reference	Applications
647-IB4		1:500	Invitrogen	I32450	IHC
CCK	Rabbit	1:1000	Frontier Institute Co. Ltd	CCK-pro-Rb-Af350	IHC
Gephyrin (7A)	Mouse	1:500	SynapticSystems	147 021	IHC
Gephyrin	Rabbit	1:100	BD Biosciences	612632	AT
GFP	Chicken	1:100	GeneTex	GTX13970	AT
GFP	Chicken	1:1000	Aves	GFP 1020	IHC, WM
GFP	Chicken	1:1000	Abcam	13970	IHC
GFP	Rabbit	1:1000	Invitrogen	A11122	IHC, WM
GluR2	Mouse	1:50	Millipore	MAB397	AT
dsRed	Rabbit	1:1000	Clontech	632496	IHC, WM
Homer1	Rabbit	1:500 (AT) or 1:1000 (IHC)	SynapticSystems	160 003	IHC, AT
mCherry	Goat	1:500	Sicgen	AB0040-200	WM
NFH	chicken	1:1000	Aves	NFH0211	IHC
NF200	Rabbit	1:1000	Sigma	N4142	WM
NeuN	Mouse	1:1000	Millipore	MAB377	IHC
Parvalbumin (PV)	Goat	1:2000	SWANT	PVG-213	IHC
Parvalbumin (PV)	Guinea Pig	1:500	Frontier Institute Co. Ltd	PV-GP-Af1000	IHC
Parvalbumin (PV)	Rabbit	1:2000-3000	SWANT	PV-25	IHC
PKCg	Rabbit	1:1000	Santa Cruz	sc-211	IHC
PKCg	Guinea Pig	1:1000	Frontier Institute Co. Ltd	PKCg-GP-Af350	IHC
PKCg	Goat	1:500	Frontier Institute Co. Ltd	PKCg-Go-Af840	ICH
PSD95	Mouse	1:100	NeuroMab	75-028	AT
Synapsin1	Rabbit	1:100	Millipore	AB1543	AT
TH	Rabbit	1:1000	Millipore	AB1542	IHC, WM
TH	Sheep	1:1000	Millipore	AB152	IHC, WM
Troma1	Rat	1:50	DSHB (U of Iowa)	TROMA-I	WM
vGAT	Goat	1:1000	Frontier Institute Co. Ltd	VGAT-Go-Af620	IHC
vGAT	Mouse	1:1000 (IHC) or 1:100 (AT)	SynapticSystems	131 011	IHC; AT
vGluT1	Guinea Pig	1:1000-1:5000	Millipore	AB5905	IHC, AT
vGluT1	Rabbit	1:20000	SynapticSystems	135 303	IHC

REFERENCES

Abraira, V.E., and Ginty, D.D. (2013). The sensory neurons of touch. Neuron *79*, 618–639.

Antal, M., Polgár, E., Chalmers, J., Minson, J.B., Llewellyn-Smith, I., Heizmann, C.W., and Somogyi, P. (1991). Different populations of parvalbumin- and calbindin-D28k-immunoreactive neurons contain GABA and accumulate 3H-D-aspartate in the dorsal horn of the rat spinal cord. J. Comp. Neurol. *314*, 114–124.

Aschauer, D.F., Kreuz, S., and Rumpel, S. (2013). Analysis of transduction efficiency, tropism and axonal transport of AAV serotypes 1, 2, 5, 6, 8 and 9 in the mouse brain. PLoS One *8*, e76310.

Badea, T.C., Hua, Z.L., Smallwood, P.M., John, W., Thomas, R., Xin, Y., and Jeremy, N. (2009). New Mouse Lines for the Analysis of Neuronal Morphology Using CreER(T)/loxP-Directed Sparse Labeling. PLoS One *4*, e7859.

Bai, L., Lehnert, B.P., Junwei, L., Neubarth, N.L., Dickendesher, T.L., Nwe, P.H., Colleen, C., Jeffery Woodbury, C., and Ginty, D.D. (2015). Genetic Identification of an Expansive Mechanoreceptor Sensitive to Skin Stroking. Cell *163*, 1783–1795.

Barlow, H. (2001). Redundancy reduction revisited. Network *12*, 241–253.

Barlow, H.B. (2012). Possible Principles Underlying the Transformations of Sensory Messages. In Sensory Communication, pp. 216–234.

Brown, A.G. (2012). Organization in the Spinal Cord: The Anatomy and Physiology of Identified Neurones (Springer Science & Business Media).

Bui, T.V., and Brownstone, R.M. (2015). Sensory-evoked perturbations of locomotor activity by sparse sensory input: a computational study. J. Neurophysiol. *113*, 2824–2839.

Bui, T.V., Akay, T., Loubani, O., Hnasko, T.S., Jessell, T.M., and Brownstone, R.M. (2013). Circuits for grasping: spinal dI3 interneurons mediate cutaneous control of motor behavior. Neuron *78*, 191–204.

Burger, C., Gorbatyuk, O.S., Velardo, M.J., Peden, C.S., Williams, P., Zolotukhin, S., Reier, P.J., Mandel, R.J., and Muzyczka, N. (2004). Recombinant AAV viral vectors pseudotyped with viral capsids from serotypes 1, 2, and 5 display differential efficiency and cell tropism after delivery to different regions of the central nervous system. Mol. Ther. *10*, 302–317.

Burgess, P.R., Petit, D., and Warren, R.M. (1968). Receptor types in cat hairy skin supplied by myelinated fibers. J. Neurophysiol. *31*, 833–848.

Casale, E.J., Light, A.R., and Rustioni, A. (1988). Direct projection of the corticospinal tract to the superficial laminae of the spinal cord in the rat. J. Comp. Neurol. *278*, 275–286.

Chaudhri, O., Small, C., and Bloom, S. (2006). Gastrointestinal hormones regulating appetite. Philos. Trans. R. Soc. Lond. B Biol. Sci. *361*, 1187–1209.

Cheema, S.S., Rustioni, A., and Whitsel, B.L. (1984). Light and electron microscopic evidence for a direct corticospinal projection to superficial laminae of the dorsal horn in cats and monkeys. J. Comp. Neurol. *225*, 276–290.

Choudhry, R., Hodgins, M.B., Van der Kwast, T.H., Brinkmann, A.O., and Boersma, W.J.A. (1992). Localization of androgen receptors in human skin by immunohistochemistry: implications for the hormonal regulation of hair growth, sebaceous glands and sweat glands. J. Endocrinol. *133*, 467 – NP.

Chung, K., and Deisseroth, K. (2013). CLARITY for mapping the nervous system. Nat. Methods *10*, 508–513.

Chung, K., Kyungsoon, C., Kevetter, G.A., Willis, W.D., and Coggeshall, R.E. (1984). An estimate of the ratio of propriospinal to long tract neurons in the sacral spinal cord of the rat. Neurosci. Lett. *44*, 173–177.

Coutaud, B., and Pilon, N. (2013a). Characterization of a novel transgenic mouse line expressing Cre recombinase under the control of the Cdx2 neural specific enhancer. Genesis *51*, 777–784.

Coutaud, B., and Pilon, N. (2013b). Characterization of a novel transgenic mouse line expressing Cre recombinase under the control of the Cdx2 neural specific enhancer. Genesis *51*, 777–784.

Cua, A.B., Wilhelm, K.P., and Maibach, H.I. (1990). Elastic properties of human skin: relation to age, sex, and anatomical region. Arch. Dermatol. Res. *282*, 283–288.

Dacey, D.M. (1993). The mosaic of midget ganglion cells in the human retina. J. Neurosci. *13*, 5334–5355.

Dani, A., Huang, B., Bergan, J., Dulac, C., and Zhuang, X. (2010). Superresolution imaging of chemical synapses in the brain. Neuron *68*, 843–856.

Del Barrio, M.G., Bourane, S., Grossmann, K., Schüle, R., Britsch, S., O'Leary, D.D.M., and Goulding, M. (2013). A transcription factor code defines nine sensory interneuron subtypes in the mechanosensory area of the spinal cord. PLoS One *8*, e77928.

Du Beau, A., Shakya Shrestha, S., Bannatyne, B.A., Jalicy, S.M., Linnen, S., and Maxwell, D.J. (2012). Neurotransmitter phenotypes of descending systems in the rat lumbar spinal cord. Neuroscience *227*, 67–79.

Duysens, J., and Pearson, K.G. (1976). The role of cutaneous afferents from the distal hindlimb in the regulation of the step cycle of thalamic cats. Exp. Brain Res. *24*, 245–255.

Fanselow, E.E., and Nicolelis, M.A. (1999). Behavioral modulation of tactile responses in the rat somatosensory system. J. Neurosci. *19*, 7603–7616.

Feldt, S., Bonifazi, P., and Cossart, R. (2011). Dissecting functional connectivity of neuronal microcircuits: experimental and theoretical insights. Trends Neurosci. *34*, 225–236.

Ferreira, T.A., Blackman, A.V., Oyrer, J., Jayabal, S., Chung, A.J., Watt, A.J., Sjöström, P.J., and van Meyel, D.J. (2014). Neuronal morphometry directly from bitmap images. Nat. Methods *11*, 982–984.

Garcia-Segura, L.M., and Perez-Marquez, J. (2014). A new mathematical function to evaluate neuronal morphology using the Sholl analysis. J. Neurosci. Methods *226*, 103–109.

Gazzaniga, M.S. (2004). The Cognitive Neurosciences (MIT Press).

Giesler, G.J., Jr, Nahin, R.L., and Madsen, A.M. (1984). Postsynaptic dorsal column pathway of the rat. I. Anatomical studies. J. Neurophysiol. *51*, 260–275.

Giesler, G.J., Jr, Miller, L.R., Madsen, A.M., and Katter, J.T. (1987). Evidence for the existence of a lateral cervical nucleus in mice, guinea pigs, and rabbits. J. Comp. Neurol. *263*, 106–112.

Gjerstad, M.D., Tandrup, T., Koltzenburg, M., and Jakobsen, J. (2002a). Predominant neuronal B-cell loss in L5 DRG of p75 receptor-deficient mice. J. Anat. *200*, 81–87.

Gjerstad, M.D., Tandrup, T., Koltzenburg, M., and Jakobsen, J. (2002b). Predominant neuronal B-cell loss in L5 DRG of p75 receptor-deficient mice. J. Anat. *200*, 81–87.

Gong, S., Kus, L., and Heintz, N. (2010). Rapid bacterial artificial chromosome modification for large-scale mouse transgenesis. Nat. Protoc. *5*, 1678–1696.

Gorski, J.A., Talley, T., Qiu, M., Puelles, L., Rubenstein, J.L.R., and Jones, K.R. (2002). Cortical excitatory neurons and glia, but not GABAergic neurons, are produced in the Emx1-expressing lineage. J. Neurosci. *22*, 6309–6314.

Graham, B.A., Brichta, A.M., and Callister, R.J. (2004). In vivo responses of mouse superficial dorsal horn neurones to both current injection and peripheral cutaneous stimulation. J. Physiol. *561*, 749–763.

Graham, B.A., Brichta, A.M., and Callister, R.J. (2007). Pinch-current injection defines two discharge profiles in mouse superficial dorsal horn neurones, in vitro. J. Physiol. *578*, 787–798.

Greig, L.C., Woodworth, M.B., Galazo, M.J., Padmanabhan, H., and Macklis, J.D. (2013). Molecular logic of neocortical projection neuron specification, development and diversity. Nat. Rev. Neurosci. *14*, 755–769.

Grudt, T.J., and Perl, E.R. (2002). Correlations between neuronal morphology and electrophysiological features in the rodent superficial dorsal horn. J. Physiol. *540*, 189–207.

Grueber, W.B., and Sagasti, A. (2010). Self-avoidance and tiling: Mechanisms of dendrite and axon spacing. Cold Spring Harb. Perspect. Biol. *2*, a001750.

Grueber, W.B., Jan, L.Y., and Jan, Y.N. (2002). Tiling of the Drosophila epidermis by multidendritic sensory neurons. Development *129*, 2867–2878.

Gutierrez-Mecinas, M., Maria, G.-M., Kuehn, E.D., Abraira, V.E., Erika, P., Masahiko, W., and Todd, A.J. (2016). Immunostaining for Homer reveals the majority of excitatory synapses in laminae I–III of the mouse spinal dorsal horn. Neuroscience *329*, 171–181.

Hama, H., Kurokawa, H., Kawano, H., Ando, R., Shimogori, T., Noda, H., Fukami, K., Sakaue-Sawano, A., and Miyawaki, A. (2011). Scale: a chemical approach for fluorescence imaging and reconstruction of transparent mouse brain. Nat. Neurosci. *14*, 1481–1488.

Hanaway, J., and Smith, J.M. (1979). Synaptic fine structure and the termination of corticospinal fibers in the lateral basal region of the cat spinal cord. J. Comp. Neurol. *183*, 471–486.

Hasegawa, H., Abbott, S., Han, B.-X., Qi, Y., and Wang, F. (2007). Analyzing somatosensory axon projections with the sensory neuron-specific Advillin gene. J. Neurosci. *27*, 14404–14414.

Hochman, S., Garraway, S.M., and Pockett, S. (1997). Membrane properties of deep dorsal horn neurons from neonatal rat spinal cord in vitro. Brain Res. *767*, 214–219.

Horch, K.W., Tuckett, R.P., and Burgess, P.R. (1977). A key to the classification of cutaneous mechanoreceptors. J. Invest. Dermatol. *69*, 75–82.

Hughes, D.I., Sikander, S., Kinnon, C.M., Boyle, K.A., Watanabe, M., Callister, R.J., and Graham, B.A. (2012). Morphological, neurochemical and electrophysiological features of parvalbumin-expressing cells: a likely source of axo-axonic inputs in the mouse spinal dorsal horn. J. Physiol. *590*, 3927–3951.

Ippolito, D.M., and Eroglu, C. (2010). Quantifying synapses: an immunocytochemistry-based assay to quantify synapse number. J. Vis. Exp.

Jackson, A., Baker, S.N., and Fetz, E.E. (2006). Tests for presynaptic modulation of corticospinal terminals from peripheral afferents and pyramidal tract in the macaque. J. Physiol. *573*, 107–120.

Johnson, K.O. (2001). The roles and functions of cutaneous mechanoreceptors. Curr. Opin. Neurobiol. *11*, 455–461.

Johnson, K.O., and Hsiao, S.S. (1992). Neural mechanisms of tactual form and texture perception. Annu. Rev. Neurosci. *15*, 227–250.

Johnson, K.O., Phillips, J.R., Hsiao, S.S., and Bankman, I.N. (1991). Tactile Pattern Recognition. In Information Processing in the Somatosensory System, pp. 305–318.

Johnson, K.O., Yoshioka, T., and Vega-Bermudez, F. (2000). Tactile functions of mechanoreceptive afferents innervating the hand. J. Clin. Neurophysiol. *17*, 539–558.

Kaiser, T., Ting, J.T., Monteiro, P., and Feng, G. (2016). Transgenic labeling of parvalbumin-expressing neurons with tdTomato. Neuroscience *321*, 236–245.

Kim, J.C., Cook, M.N., Carey, M.R., Shen, C., Regehr, W.G., and Dymecki, S.M. (2009). Linking genetically defined neurons to behavior through a broadly applicable silencing allele. Neuron *63*, 305–315.

King, A.E., Thompson, S.W., Urban, L., and Woolf, C.J. (1988). The responses recorded in vitro of deep dorsal horn neurons to direct and orthodromic stimulation in the young rat spinal cord. Neuroscience *27*, 231–242.

Koltzenburg, M., Stucky, C.L., and Lewin, G.R. (1997). Receptive properties of mouse sensory neurons innervating hairy skin. J. Neurophysiol. *78*, 1841–1850.

Kramer, A.P., and Kuwada, J.Y. (1983). Formation of the receptive fields of leech mechanosensory neurons during embryonic development. J. Neurosci. *3*, 2474–2486.

Kumazawa, T., and Perl, E.R. (1977). Primate cutaneous sensory units with unmyelinated (C) afferent fibers. J. Neurophysiol. *40*, 1325–1338.

Kuwajima, T., Sitko, A.A., Bhansali, P., Jurgens, C., Guido, W., and Mason, C. (2013). ClearT: a detergent- and solvent-free clearing method for neuronal and non-neuronal tissue. Development *140*, 1364–1368.

Laing, I., Todd, A.J., Heizmann, C.W., and H.H.H.W., S. (1994). Subpopulations of gabaergic neurons in laminae i–iii of rat spinal dorsal horn defined by coexistence with classical transmitters, peptides, nitric oxide synthase or parvalbumin. Neuroscience *61*, 123–132.

Laurent, G. (2002). Olfactory network dynamics and the coding of multidimensional signals. Nat. Rev. Neurosci. *3*, 884–895.

Lechner, S.G., and Lewin, G.R. (2013). Hairy sensation. Physiology *28*, 142–150.

Li, L., and Ginty, D.D. (2014). The structure and organization of lanceolate mechanosensory complexes at mouse hair follicles. Elife *3*, e01901.

Li, L., Rutlin, M., Abraira, V.E., Cassidy, C., Kus, L., Gong, S., Jankowski, M.P., Luo, W., Heintz, N., Koerber, H.R., et al. (2011). The functional organization of cutaneous low-threshold mechanosensory neurons. Cell *147*, 1615–1627.

Liu, H., Kim, S.-Y., Fu, Y., Wu, X., Ng, L., Swaroop, A., and Forrest, D. (2013). An isoform of retinoid-related orphan receptor β directs differentiation of retinal amacrine and horizontal interneurons. Nat. Commun. *4*, 1813.

Liu, P., Jenkins, N.A., and Copeland, N.G. (2003). A highly efficient recombineering-based method for generating conditional knockout mutations. Genome Res. *13*, 476–484.

Lopez-Garcia, J.A., and King, A.E. (1994). Membrane properties of physiologically classified rat dorsal horn neurons in vitro: correlation with cutaneous sensory afferent input. Eur. J. Neurosci. *6*, 998–1007.

Lorenzo, L-E, Godin, A.G., Wang, F., St-Louis, M, Carbonetto, S., Wiesman, P.W., Ribeiro-da-Silva, A., and De Koninck, Y. (2014). Gephyrin clusters are absent from small diameter primary afferent terminals despite the presence of GABAA receptors. J. Neuroscience, 34; 8300 – 8317.

Lumpkin, E.A., Marshall, K.L., and Nelson, A.M. (2010). The cell biology of touch. J. Cell Biol. *191*, 237–248.

Luo, W., Enomoto, H., Rice, F.L., Milbrandt, J., and Ginty, D.D. (2009). Molecular identification of rapidly adapting mechanoreceptors and their developmental dependence on ret signaling. Neuron *64*, 841–856.

Madisen, L., Zwingman, T.A., Sunkin, S.M., Oh, S.W., Zariwala, H.A., Gu, H., Ng, L.L., Palmiter, R.D., Hawrylycz, M.J., Jones, A.R., et al. (2010). A robust and high-throughput Cre reporting and characterization system for the whole mouse brain. Nat. Neurosci. *13*, 133–140.

Madisen, L., Mao, T., Koch, H., Zhuo, J.-M., Berenyi, A., Fujisawa, S., Hsu, Y.-W.A., Garcia, A.J., 3rd, Gu, X., Zanella, S., et al. (2012). A toolbox of Cre-dependent optogenetic transgenic mice for light-induced activation and silencing. Nat. Neurosci. *15*, 793–802.

Madisen, L., Garner, A.R., Shimaoka, D., Chuong, A.S., Klapoetke, N.C., Li, L., van der Bourg, A., Niino, Y., Egolf, L., Monetti, C., et al. (2015). Transgenic mice for intersectional targeting of neural sensors and effectors with high specificity and performance. Neuron *85*, 942–958.

Masland, R.H. (2001). The fundamental plan of the retina. Nat. Neurosci. *4*, 877–886.

Mason, M.R.J., Ehlert, E.M.E., Eggers, R., Pool, C.W., Hermening, S., Huseinovic, A., Timmermans, E., Blits, B., and Verhaagen, J. (2010). Comparison of AAV serotypes for gene delivery to dorsal root ganglion neurons. Mol. Ther. *18*, 715–724.

Maxwell, D.J., Koerber, H.R., and Bannatyne, B.A. (1985). Light and electron microscopy of contacts between primary afferent fibres and neurones with axons ascending the dorsal columns of the feline spinal cord. Neuroscience *16*, 375–394.

Maxwell, D.J., Ottersen, O.P., and Storm-Mathisen, J. (1995). Synaptic organization of excitatory and inhibitory boutons associated with spinal neurons which project through the dorsal columns of the cat. Brain Res. *676*, 103–112.

Maxwell, D.J., Belle, M.D., Cheunsuang, O., Stewart, A., and Morris, R. (2007). Morphology of inhibitory and excitatory interneurons in superficial laminae of the rat dorsal horn. J. Physiol. *584*, 521–533.

McGlone, F., Wessberg, J., and Olausson, H. (2014). Discriminative and affective touch: sensing and feeling. Neuron *82*, 737–755.

Mitchell, K., Spike, R.C., and Todd A.J. (1993). An immunocytochemical study of glycine receptor and GABA in laminae I-III of rat spinal dorsal horn. J. Neurosci. 13:2371–2381.

Morgan, J.L., Berger, D.R., Wetzel, A.W., and Lichtman, J.W. (2016). The Fuzzy Logic of Network Connectivity in Mouse Visual Thalamus. Cell *165*, 192–206.

Morin, F. (1955). A new spinal pathway for cutaneous impulses. Am. J. Physiol. *183*, 245–252.

Mountcastle, V.B. (1957). Modality and topographic properties of single neurons of cat's somatic sensory cortex. J. Neurophysiol. *20*, 408–434.

Neumann, S., Braz, J.M., Skinner, K., Llewellyn-Smith, I.J., and Basbaum, A.I. (2008). Innocuous, Not Noxious, Input Activates PKC Interneurons of the Spinal Dorsal Horn via Myelinated Afferent Fibers. Journal of Neuroscience *28*, 7936–7944.

Niederkofler, V., Asher, T.E., Okaty, B.W., Rood, B.D., Narayan, A., Hwa, L.S., Beck, S.G., Miczek, K.A., and and Dymecki, S.M. (2016). Identification of serotonergic neuronal modules that affect aggressive behavior. Cell Rep. *in press*.

Niu, J., Ding, L., Li, J.J., Kim, H., Liu, J., Li, H., Moberly, A., Badea, T.C., Duncan, I.D., Son, Y.-J., et al. (2013). Modality-based organization of ascending somatosensory axons in the direct dorsal column pathway. J. Neurosci. *33*, 17691–17709.

Olausson, H., Lamarre, Y., Backlund, H., Morin, C., Wallin, B.G., Starck, G., Ekholm, S., Strigo, I., Worsley, K., Vallbo, A.B., et al. (2002). Unmyelinated tactile afferents signal touch and project to insular cortex. Nat. Neurosci. *5*, 900–904.

Orefice, L.L., Zimmerman, A.L., Chirila, A.M., Sleboda, S.J., Head, J.P., and Ginty, D.D. (2016). Peripheral Mechanosensory Neuron Dysfunction Underlies Tactile and Behavioral Deficits in Mouse Models of ASDs. Cell *166*, 299–313.

Ortuño, T., Grieve, K.L., Cao, R., Cudeiro, J., and Rivadulla, C. (2014). Bursting thalamic responses in awake monkey contribute to visual detection and are modulated by corticofugal feedback. Front. Behav. Neurosci. *8*, 198.

Otazu, G.H., Chae, H., Davis, M.B., and Albeanu, D.F. (2015). Cortical Feedback Decorrelates Olfactory Bulb Output in Awake Mice. Neuron *86*, 1461–1477.

Owens, D.M., and Lumpkin, E.A. (2014). Diversification and specialization of touch receptors in skin. Cold Spring Harb. Perspect. Med. *4*.

Petitjean, H., Pawlowski, S.A., Fraine, S.L., Sharif, B., Hamad, D., Fatima, T., Berg, J., Brown, C.M., Jan, L.-Y., Ribeiro-da-Silva, A., et al. (2015). Dorsal Horn Parvalbumin Neurons Are Gate-Keepers of Touch-Evoked Pain after Nerve Injury. Cell Rep. *13*, 1246–1257.

Polgár, E., Durrieux, C., Hughes, D.I., and Todd, A.J. (2013). A quantitative study of inhibitory interneurons in laminae I-III of the mouse spinal dorsal horn. PLoS One *8*, e78309.

de Pommery, J., Roudier, F., and Menétrey, D. (1984). Postsynaptic fibers reaching the dorsal column nuclei in the rat. Neurosci. Lett. *50*, 319–323.

Prescott, S.A., and De Koninck, Y. (2002). Four cell types with distinctive membrane properties and morphologies in lamina I of the spinal dorsal horn of the adult rat. J. Physiol. *539*, 817–836.

Punnakkal, P., von Schoultz, C., Haenraets, K., Wildner, H., and Zeilhofer, H.U. (2014). Morphological, biophysical and synaptic properties of glutamatergic neurons of the mouse spinal dorsal horn. J. Physiol. *592*, 759–776.

Rajković, K., Marić, D.L., Milošević, N.T., Jeremic, S., Arsenijević, V.A., and Rajković, N. (2016). Mathematical modeling of the neuron morphology using two dimensional images. J. Theor. Biol. *390*, 80–85.

Ralston, D.D., and Ralston, H.J., 3rd (1985). The terminations of corticospinal tract axons in the macaque monkey. J. Comp. Neurol. *242*, 325–337.

Renier, N., Nicolas, R., Zhuhao, W., Simon, D.J., Jing, Y., Pablo, A., and Marc, T.-L. (2014). iDISCO: A Simple, Rapid Method to Immunolabel Large Tissue Samples for Volume Imaging. Cell *159*, 896–910.

Rexed, B. (1952). The cytoarchitectonic organization of the spinal cord in the cat. J. Comp. Neurol. *96*, 414–495.

Rozell, C.J., Johnson, D.H., Baraniuk, R.G., and Olshausen, B.A. (2008). Sparse coding via thresholding and local competition in neural circuits. Neural Comput. *20*, 2526–2563.

Rudomin, P., and Schmidt, R.F. (1999). Presynaptic inhibition in the vertebrate spinal cord revisited. Exp. Brain Res. *129*, 1–37.

Russo, R.E., Delgado-Lezama, R., and Hounsgaard, J. (2000). Dorsal root potential produced by a TTX-insensitive micro-circuitry in the turtle spinal cord. J. Physiol. *528 Pt 1*, 115–122.

Rustioni, A., and Kaufman, A.B. (1977). Identification of cells or origin of non-primary afferents to the dorsal column nuclei of the cat. Exp. Brain Res. *27*, 1–14.

Rutlin, M., Michael, R., Cheng-Ying, H., Abraira, V.E., Colleen, C., Ling, B., Jeffery Woodbury, C., and Ginty, D.D. (2015). The Cellular and Molecular Basis of Direction Selectivity of Aδ-LTMRs. Cell *160*, 1027.

Saunders, A., Oldenburg, I.A., Berezovskii, V.K., Johnson, C.A., Kingery, N.D., Elliott, H.L., Xie, T., Gerfen, C.R., and Sabatini, B.L. (2015). A direct GABAergic output from the basal ganglia to frontal cortex. Nature *521*, 85–89.

Schlake, T., and Thomas, S. (2007). Determination of hair structure and shape. Semin. Cell Dev. Biol. *18*, 267–273.

Seal, R.P., Wang, X., Guan, Y., Raja, S.N., Woodbury, C.J., Basbaum, A.I., and Edwards, R.H. (2009). Injury-induced mechanical hypersensitivity requires C-low threshold mechanoreceptors. Nature *462*, 651–655.

Seki, K., and Fetz, E.E. (2012). Gating of sensory input at spinal and cortical levels during preparation and execution of voluntary movement. J. Neurosci. *32*, 890–902.

Sieber, M.A., Storm, R., Martinez-de-la-Torre, M., Müller, T., Wende, H., Reuter, K., Vasyutina, E., and Birchmeier, C. (2007). Lbx1 acts as a selector gene in the fate determination of somatosensory and viscerosensory relay neurons in the hindbrain. J. Neurosci. *27*, 4902–4909.

Tamamaki, N., Yanagawa, Y., Tomioka, R., Miyazaki, J.-I., Obata, K., and Kaneko, T. (2003). Green fluorescent protein expression and colocalization with calretinin, parvalbumin, and somatostatin in the GAD67-GFP knock-in mouse. J. Comp. Neurol. *467*, 60–79.

Taniguchi, H., He, M., Wu, P., Kim, S., Paik, R., Sugino, K., Kvitsiani, D., Kvitsani, D., Fu, Y., Lu, J., et al. (2011). A resource of Cre driver lines for genetic targeting of GABAergic neurons in cerebral cortex. Neuron *71*, 995–1013.

Thomson, A.M., West, D.C., and Headley, P.M. (1989). Membrane Characteristics and Synaptic Responsiveness of Superficial Dorsal Horn Neurons in a Slice Preparation of Adult Rat Spinal Cord. Eur. J. Neurosci. *1*, 479–488.

Todd, A.J. (1996). GABA and glycine in synaptic glomeruli of the rat spinal dorsal horn. Eur. J. Neurosci. *8*, 2492–2498.

Todd, A.J. (2010). Neuronal circuitry for pain processing in the dorsal horn. Nat. Rev. Neurosci. *11*, 823–836.

Todd, A.J., Hughes, D.I., Polgár, E., Nagy, G.G., Mackie, M., Ottersen, O.P., and Maxwell, D.J. (2003). The expression of vesicular glutamate transporters VGLUT1 and VGLUT2 in neurochemically defined axonal populations in the rat spinal cord with emphasis on the dorsal horn. Eur. J. Neurosci. *17*, 13–27.

Tsunozaki, M., Makoto, T., and Bautista, D.M. (2009). Mammalian somatosensory mechanotransduction. Curr. Opin. Neurobiol. *19*, 362–369.

Uesaka, T., Nagashimada, M., Yonemura, S., and Enomoto, H. (2008). Diminished Ret expression compromises neuronal survival in the colon and causes intestinal aganglionosis in mice. J. Clin. Invest. *118*, 1890–1898.

Valtschanoff, J.G., Weinberg, R.J., and Rustioni, A. (1993). Amino acid immunoreactivity in corticospinal terminals. Exp. Brain Res. *93*, 95–103.

Vrontou, S., Wong, A.M., Rau, K.K., Koerber, H.R., and Anderson, D.J. (2013). Genetic identification of C fibres that detect massage-like stroking of hairy skin in vivo. Nature *493*, 669–673.

Wassle, H., and Riemann, H.J. (1978). The Mosaic of Nerve Cells in the Mammalian Retina. Proceedings of the Royal Society B: Biological Sciences *200*, 441–461.

Wässle, H., Peichl, L., and Boycott, B.B. (1981). Dendritic territories of cat retinal ganglion cells. Nature *292*, 344–345.

Watson, A.H.D., Hughes, D.I., and Bazzaz, A.A. (2002). Synaptic relationships between hair follicle afferents and neurones expressing GABA and glycine-like immunoreactivity in the spinal cord of the rat. J. Comp. Neurol. *452*, 367–380.

Woo, S.-H., Lumpkin, E.A., and Patapoutian, A. (2015). Merkel cells and neurons keep in touch. Trends Cell Biol. *25*, 74–81.

Wu, H., Williams, J., and Nathans, J. (2012). Morphologic diversity of cutaneous sensory afferents revealed by genetically directed sparse labeling. Elife *1*, e00181.

Xiao, Z., and Suga, N. (2002). Modulation of cochlear hair cells by the auditory cortex in the mustached bat. Nat. Neurosci. *5*, 57–63.

Yasaka, T., Kato, G., Furue, H., Rashid, M.H., Sonohata, M., Tamae, A., Murata, Y., Masuko, S., and Yoshimura, M. (2007). Cell-type-specific excitatory and inhibitory circuits involving primary afferents in the substantia gelatinosa of the rat spinal dorsal horn in vitro. J. Physiol. *581*, 603–618.

Yasaka, T., Tiong, S.Y.X., Hughes, D.I., Riddell, J.S., and Todd, A.J. (2010). Populations of inhibitory and excitatory interneurons in lamina II of the adult rat spinal dorsal horn revealed by a combined electrophysiological and anatomical approach. Pain *151*, 475–488.

Yosipovitch, G., Maayan-Metzger, A., Merlob, P., and Sirota, L. (2000). Skin barrier properties in different body areas in neonates. Pediatrics *106*, 105–108.

Zhu, H., and Luo, L. (2004). Diverse functions of N-cadherin in dendritic and axonal terminal arborization of olfactory projection neurons. Neuron *42*, 63–75.

Zhu, D., Larin, K.V., Luo, Q., and Tuchin, V.V. (2013). Recent progress in tissue optical clearing. Laser Photon. Rev. *7*, 732–757.

Zimmerman, A., Bai, L., and Ginty, D.D. (2014). The gentle touch receptors of mammalian skin. Science *346*, 950–954.

Zincarelli, C., Carmela, Z., Stephen, S., Giuseppe, R., and Rabinowitz, J.E. (2008). Analysis of AAV Serotypes 1–9 Mediated Gene Expression and Tropism in Mice After Systemic Injection. Mol. Ther. *16*, 1073–1080.

Emily D. Kuehn

1762 Beacon Street #3 Brookline, MA 02445
Tel: (586) 904-0100
E-mail: emily.d.kuehn@gmail.com

Education

Johns Hopkins University School of Medicine, Baltimore, MD
The Solomon H. Snyder Department of Neuroscience
Ph.D. in Neuroscience (expected October 2016)

Kalamazoo College, Kalamazoo, MI
Bachelor of Arts (BA) degree, *cum laude*, June 2010
Major: Biology
Concentrations: Neuroscience, Biochemistry & Molecular Biology

Research Experience

08/2011 – Present	**Graduate Student** The Solomon H. Snyder Department of Neuroscience Johns Hopkins University School of Medicine, Baltimore, MD *Elucidating the morphological and synaptic organization of mammalian touch circuits.* Dr. David Ginty, Principal Investigator
08/2010 – 07/2011	**Research Technician** Department of Biomedical Sciences; Center for Structural & Functional Neuroscience University of Montana, Missoula, MT *Synergistic signaling of RTKs and SFKs within endosomes and the plasma membrane.* Dr. Mark Grimes, Principal Investigator
06/2009 – 08/2009 06/2008 – 08/2008	**Summer Undergraduate Research Fellowship (SURF) Intern** Department of Biomedical Sciences; Center for Structural & Functional Neuroscience University of Montana, Missoula, MT *Role of ALK and Trk signaling in neuroblastoma differentiation*. Dr. Mark Grimes, Principal Investigator
06/2007 – 08/2007	**Research Assistant** Entomology Department Walter Reed Army Institute of Research, Silver Spring, MD *Effectiveness of novel traps in capturing female mosquitoes.* Dr. Victoria Solberg, Principal Investigator

Publications and Presentations

Abraira VE* and **Kuehn ED*** *et al*. The cellular and synaptic architecture of the mechanosensory dorsal horn. (*in review*; *these authors contributed equally)

Gutierrez-Mecinas M, **Kuehn ED**, Abraira VA, Polgar E, Watanabe M, Todd AJ. Immunostaining for Homer reveals the majority of excitatory synapses in laminae I-III of the mouse spinal dorsal horn. *Neuroscience*. In press.

Palacios-Moreno J, Foltz L, Guo A, Stokes MP, **Kuehn ED**, George L, Comb M, Grimes ML. 2015. Neuroblastoma tyrosine kinase signaling networks involve FYN and LYN in endosomes and lipid rafts. *PLoS Comput. Biol.* 11(4):e1004130.

Kuehn ED, Zhang Q, Bai L, Zimmerman A, Abraira VE, Ginty DD. Elucidating the morphological and synaptic organization of the mammalian touch circuit. Poster session presented at: Cold Spring Harbor Laboratories Wiring the Brain. 2015 March 24-28; Cold Spring Harbor, NY.

Teaching Experience

Sept 2015 – May 2016	**Course head** for Pleasure, Pain, and Everything Between (Neuro107) *Harvard University, Cambridge, MA*
July 2015	**Participant** in Theory & Practice for STEM Professionals *Center for Excellence in Teaching at Simmons College, Boston, MA*
Sept 2014 – Dec 2014	**Teaching fellow** for Development, Plasticity, & Decline *Harvard University, Cambridge, MA*
Jan 2013 – June 2013	**Teaching assistant** for Neuroscience & Cognition II *Johns Hopkins University School of Medicine, Baltimore, MD*
Oct 2010 – July 2011	**Private Tutor** for Cellular & Molecular Biology students *University of Montana, Missoula, MT*
Mar 2009 – June 2010	**Teaching assistant** for Cell & Molecular Biology laboratory *Kalamazoo College, Kalamazoo, MI*
Mar 2009 – June 2010	**Supplemental Instruction (SI) leader** for Biology department *Kalamazoo College, Kalamazoo, MI*

Outreach

Jan 2016 – June 2016	**Teaching Assistant** for Overnights Program *Boston Museum of Science, Boston, MA*
Jan 2016 – Mar 2016	**Blog Writer** for Science in the News *Harvard University Graduate School of Arts & Sciences, Boston, MA*
Sept 2012 – Sept 2013	**LIFE co-chair** (Leadership Initiative for the Environment) *Johns Hopkins University School of Medicine, Baltimore, MD*
June 2007 – Aug 2007	**Near-Peer Mentor** for Gains in Mathematics and Science Program *Walter Reed Army Institute of Research, Silver Spring, MD*

Mentoring and Advising

Harvard Medical School, Boston, MA

Nov 2015 – Feb 2016	**HPREP mentor**, Health Professions Recruitment & Exposure Program
Jan 2015 – April 2015	**Rotation mentor**, Qiyu Zhang, Program in Neuroscience Ph.D. student

Summer 2015, 2016	**Lab mentor**, Haley Dolan, University of Wisconsin Biology student
Dec 2014 – Aug 2016	**Lab & project mentor**, Katie West, Simmons College Biology student
Aug– Oct 2014	**Lab mentor**, Cynthia Morton, Simmons College Nursing student
Jan 2014 – Dec 2014	**Lab mentor**, Pann Nwe, Simmons College, Public Health student
Jan 2014 – Aug 2014	**Lab mentor**, Isabella Alveal, Simmons College Biology student

Kalamazoo College, Kalamazoo, MI

Sept 2009 – June 2010	**Departmental Student Advisor** for Neuroscience department
Jan 2007 – June 2010	**Executive board member and mentor** for Sisters in Science

Honors and Awards

June 2016	NRC RAP fellowship, *National Research Council (NRC)*
Spring 2016	Certificate of Teaching Excellence, *The Derek Bok Center for Teaching & Learning, Harvard University*
Fall 2015	Certificate of Teaching Excellence, *The Derek Bok Center for Teaching & Learning, Harvard University*
March 2013	Graduate Research Fellowship Program Honorable Mention, *National Science Foundation (NSF)*
June 2010	Diebold Scholar Award, *Kalamazoo College*
March 2010	Alternate recipient for Fulbright Grant, *Fulbright U.S. Student Program*
February 2010	Enlightened Leadership Award, *Kalamazoo College*
May 2009	Summer Research Scholarship recipient, *Howard Hughes Medical Institute (HHMI)*
May 2009-2008	Summer Undergraduate Research Fellowship (SURF) recipient, *University of Montana*
May 2008	Field Experience Scholarship recipient, *Kalamazoo College*